The Astrophysical Journal Supplement Series, 268:18 (38pp), 2023 September https://doi.org/10.3847/1538-4365/acdf5d


# Linear Mode Decomposition in Magnetohydrodynamics Revisited

G. P. Zank[1,2], L.-L. Zhao[1,2], L. Adhikari[1,2], M. Nakanotani[1], A. Pitňa[3], D. Telloni[4], and H. Che[1,2]
[1] Center for Space Plasma and Aeronomic Research (CSPAR), University of Alabama in Huntsville, Huntsville, AL 35805, USA; garyp.zank@gmail.com
[2] Department of Space Science, University of Alabama in Huntsville, Huntsville, AL 35805, USA
[3] Department of Surface and Plasma Science, Faculty of Mathematics and Physics, Charles University, Prague, Czechia
[4] National Institute for Astrophysics, Astrophysical Observatory of Torino, Via Osservatorio 20, I-10025 Pino Torinese, Italy
*Received 2023 May 6; revised 2023 June 10; accepted 2023 June 16; published 2023 August 28*

## Abstract

Small-amplitude fluctuations in the magnetized solar wind are measured typically by a single spacecraft. In the magnetohydrodynamics (MHD) description, fluctuations are typically expressed in terms of the fundamental modes admitted by the system. An important question is how to resolve an observed set of fluctuations, typically plasma moments such as the density, velocity, pressure, and magnetic field fluctuations, into their constituent fundamental MHD modal components. Despite its importance in understanding the basic elements of waves and turbulence in the solar wind, this problem has not yet been fully resolved. Here, we introduce a new method that identifies between wave modes and advected structures such as magnetic islands or entropy modes and computes the phase information associated with the eligible MHD modes. The mode-decomposition method developed here identifies the admissible modes in an MHD plasma from a set of plasma and magnetic field fluctuations measured by a single spacecraft at a specific frequency and an inferred wavenumber $\boldsymbol{k}_m$. We present data from three typical intervals measured by the Wind and Solar Orbiter spacecraft at ∼1 au and show how the new method identifies both propagating (wave) and nonpropagating (structures) modes, including entropy and magnetic island modes. This allows us to identify and characterize the separate MHD modes in an observed plasma parcel and to derive wavenumber spectra of entropic density, fast and slow magnetosonic, Alfvénic, and magnetic island fluctuations for the first time. These results help identify the fundamental building blocks of turbulence in the magnetized solar wind.

*Unified Astronomy Thesaurus concepts:* Solar wind (1534)

## 1. Introduction

The decomposition of small-amplitude fluctuations measured by spacecraft observations made in the solar wind, or even those found in simulations, into their constituent modes has an extensive history, beginning with the work of Glassmeier et al. (1995) and Motschmann et al. (1998) and continuing through until today (e.g., Zhao et al. 2021b, 2022a). A related approach was developed by Cho & Lazarian (2003) for numerical magnetohydrodynamic (MHD) simulations in the context of compressible turbulence. In all these approaches, an observed interval of fluctuations is decomposed into three sets of forward and backward eigenmodes, namely the Alfvénic, fast, and slow modes. Recently, Gan et al. (2022) and Fu et al. (2022) presented interesting numerical simulations exploring the existence and properties of fast-mode MHD waves and density fluctuations, respectively, in a turbulent magnetofluid. The identification of the various modes was based on the use of spatiotemporal 4D fast Fourier transform (FFT) routines to analyze the fluctuations. While appropriate to a numerical simulation, such an approach cannot be applied to single-point measurements made by a spacecraft in the solar wind. Despite the popularity of the mode-decomposition technique developed by Glassmeier et al. (1995) and Motschmann et al. (1998) and its numerous applications to the solar wind (see, e.g., Zhao et al. 2021b, 2022a and references therein), the Alfvénic, fast, and slow modes are not the only linear modes supported by MHD. Linear Alfvénic modes as well as fast and slow magnetosonic modes are examples of propagating waves, each possessing a characteristic velocity (the Alfvén ($\boldsymbol{V}_{\rm A}$) and fast and slow magnetosonic ($\boldsymbol{V}_{f,s}$) velocities, respectively) that, in a flowing magnetofluid with a background or mean velocity $\boldsymbol{U}_0$, are both advected with and propagate relative to the fluid at the characteristic velocity $\boldsymbol{U}_0 \pm \boldsymbol{V}_{{\rm A},f,s}$. Nonpropagating linear modes are also characteristic modes of a magnetofluid, and such modes are simply advected by the background flow and have a characteristic velocity $\boldsymbol{U}_0$. Two exclusively advected modes are admitted by a magnetofluid, one of which is the entropy mode $s \propto p/\rho^{\gamma}$ (where $s$, $p$, $\rho$, and $\gamma$ are the entropy, pressure, density, and adiabatic index, respectively), being a fluctuation in the entropy and density with no accompanying change in the pressure (or the fluid velocity or magnetic field) The entropy mode reflects essentially the "lumpiness" of a fluid (as an analogy, one might think of a sauce in which the thickening agent has not been fully whisked smooth). The second advected linear mode, a magnetic flux rope or magnetic island, is a structure that is of a purely magnetic character, which, when projected into a 2D plane orthogonal to the mean magnetic field, forms a structure of closed, nested magnetic field lines. Only the fluctuating transverse components of the magnetic field form a magnetic island. In 3D, the superposition of the transverse magnetic island fluctuations and the mean magnetic field (orthogonal to the transverse magnetic field fluctuations) creates a flux rope in which the transverse fluctuating magnetic field components wind around the mean magnetic field in a helical sense. The analog of the advected linear vorticity mode of hydrodynamics is absent in a magnetofluid because vorticity is coupled to the magnetic field

through the Alfvén mode. This is discussed further in Section 2.

Indeed, numerous studies of solar wind fluctuations using entirely different techniques have identified nonpropagating flux rope modes (Veltri 1999; Moldwin et al. 2000; Feng et al. 2008; Greco et al. 2008; Telloni et al. 2013, 2020; Trenchi et al. 2013; Khabarova et al. 2015, 2016; Khabarova & Zank 2017; Zheng & Hu 2018; Adhikari et al. 2019; Chen et al. 2019; Malandraki et al. 2019; Zhao et al. 2019, 2021a), and they form an integral and substantial part of the solar wind fluctuation zoo. The presence of flux ropes or magnetic islands in the solar wind is reflected in the competing views or paradigms of solar wind turbulence, with one camp regarding low-frequency MHD turbulence as primarily Alfvénic in character (sometimes described as Alfvénic turbulence or slab turbulence), comprised of counterpropagating Alfvén waves that can interact nonlinearly through a resonance between two oppositely propagating Alfvén waves and a zero-frequency mode. Anisotropy within this perspective is addressed within the critical balance description of Goldreich & Sridhar (1995). An alternative perspective is that MHD turbulence is comprised primarily of structures, i.e., nonpropagating modes, which are thought to be 2D flux ropes or magnetic islands that interact nonlinearly, dominated by the 2D component with a minority Alfvénic or slab component (Zank & Matthaeus 1992, 1993; Bieber et al. 1996; Saur & Bieber 1999; Hunana & Zank 2010; Forman et al. 2011; Zank et al. 2017, 2020; Zhao et al. 2023), giving a quasi-2D character for nearly incompressible (NI MHD) turbulence. It is possible, however, as discussed by Bandyopadhyay & McComas (2021), Zhao et al. (2022b), that the slab component may become more dominant as distance from the Sun decreases, and the manner in which turbulence anisotropy evolves with heliocentric distance remains an important and open question. Finally, density fluctuations (Telloni et al. 2009; Bruno et al. 2014; Zank et al. 2021a) are of course present in the solar wind, and it has been argued that some of them are advected entropy-related density fluctuations (Hunana & Zank 2010; Adhikari et al. 2017, 2020b, 2020a; Zank et al. 2017; Asgari-Targhi et al. 2021; Tasnim et al. 2022).

Our purpose here is not to resolve the debate about the nature of MHD turbulence in the solar wind but to develop tools to analyze small-amplitude linear fluctuations in the solar wind from which their modal composition can be determined. In principle, any mode-decomposition analysis of a set of MHD scale/frequency fluctuations observed in the solar wind should include the nonpropagating as well as the propagating modes. Curiously, the possibility of nonpropagating or structure modes appears not to have been addressed in any previous analyses. The important question of how MHD structures, including entropy modes, should be incorporated into a mode decomposition is addressed here.

A second important question is whether previous approaches to mode decomposition have incorporated correctly the corresponding phase information for the constituent modes. This is critical in (1) rendering a proper mode decomposition of a measured fluctuation and (2) properly relating the observed frequency to wavenumber space. It is possible, as we show, to evaluate the individual phase relations for each mode, which then yields the relation between the frequency and wavenumbers for individual decomposed modes.

The paper is structured as follows. We first revisit the linear modes that are admitted by the equations of ideal MHD, with Section 2 addressing in particular the nonpropagating modes. Based on this analysis, we derive the requisite eigenrelations for each mode. In Section 3, we present the mode-decomposition analysis, deriving an $8 \times 8$ linear system of equations that governs the decomposition of an observed set of measured fluctuations, together with a set of constraints that specify the various wavenumber relations. This allows us to determine from a measured Doppler-shifted frequency $\omega'_m$, inferred wavenumber vector $\boldsymbol{k}_m$, and set of measured MHD fluctuations (density $\delta\rho_m$, velocity $\delta\boldsymbol{u}_m$, pressure $\delta p_m$, and magnetic field $\delta\boldsymbol{B}_m$) the underlying MHD modes that comprise the observed fluctuations. By way of illustration, the simpler and less laborious analysis for hydrodynamics is given in an Appendix. Section 4 concludes with some representative analyses using solar wind data at 1 and 0.81 au from the Wind and Solar Orbiter spacecraft, respectively. Besides presenting a simplified analysis for 2D hydrodynamics in an appendix, we provide appendices listing the detailed entries of the $8 \times 8$ mode-decomposition matrix and a summary of the algorithm. Further discussion and comments can be found in the conclusions.

## 2. Linear MHD Modes

For the subsequent analysis, it is useful to review the linear modes admitted by the ideal MHD equations, because it is quite widely—if erroneously—thought that MHD admits only six basic modes (the forward and backward fast and slow magnetosonic modes and the forward and backward Alfvén modes). The ideal MHD equations in a Cartesian coordinate system are expressed in nonconservative form as usual by

$$\frac{\partial \rho}{\partial t} + \nabla \cdot (\rho \boldsymbol{U}) = 0; \tag{1}$$

$$\rho\left(\frac{\partial \boldsymbol{U}}{\partial t} + \boldsymbol{U} \cdot \nabla \boldsymbol{U}\right) = -\nabla P + \frac{1}{\mu_0}(\nabla \times \boldsymbol{B}) \times \boldsymbol{B}; \tag{2}$$

$$\frac{\partial P}{\partial t} + \boldsymbol{U} \cdot \nabla P + \gamma P \nabla \cdot \boldsymbol{U} = 0; \tag{3}$$

$$\frac{\partial \boldsymbol{B}}{\partial t} + \boldsymbol{U} \cdot \nabla \boldsymbol{B} = \boldsymbol{B} \cdot \nabla \boldsymbol{U} - \boldsymbol{B}(\nabla \cdot \boldsymbol{U}); \tag{4}$$

$$\nabla \cdot \boldsymbol{B} = 0, \tag{5}$$

where $\rho$, $\boldsymbol{U} = (U_x, U_y, U_z)$, $P$, $\boldsymbol{B} = (B_x, B_y, B_z)$, $\gamma$, and $\mu_0$ respectively denote the mass density, flow velocity, scalar pressure, magnetic field, the adiabatic index, and the permeability of free space. On introducing the entropy $S = C_V \ln(P/\rho^\gamma)$, with $C_V$ being the specific heat at constant volume, Equations (1) and (3) yield the entropy transport equation:

$$\frac{\partial S}{\partial t} + \boldsymbol{U} \cdot \nabla S = 0. \tag{6}$$

Let us introduce a set of small-amplitude fluctuations $\delta\Psi \equiv (\delta\rho, \delta\boldsymbol{u}, \delta p, \delta\boldsymbol{B})$ about the mean solar wind background flow parameters $\rho_0$, $\boldsymbol{U}_0$, $P_0$, and $\boldsymbol{B}_0$, and linearize (1)–(5), obtaining as usual:

$$\frac{\partial \delta\rho}{\partial t} + \boldsymbol{U}_0 \cdot \nabla \delta\rho + \rho_0 \nabla \cdot \delta\boldsymbol{u} = 0; \tag{7}$$

$$\frac{\partial \delta \boldsymbol{u}}{\partial t} + \boldsymbol{U}_0 \cdot \nabla \delta \boldsymbol{u} = -\frac{1}{\rho_0}\nabla \delta p + \frac{1}{\mu_0 \rho_0}(\nabla \times \delta \boldsymbol{B}) \times \boldsymbol{B}_0; \quad (8)$$

$$\frac{\partial \delta p}{\partial t} + \boldsymbol{U}_0 \cdot \nabla \delta p + \gamma P_0 \nabla \cdot \delta \boldsymbol{u} = 0; \quad (9)$$

$$\frac{\partial \delta \boldsymbol{B}}{\partial t} + \boldsymbol{U}_0 \cdot \nabla \delta \boldsymbol{B} = \boldsymbol{B}_0 \cdot \nabla \delta \boldsymbol{u} - \boldsymbol{B}_0(\nabla \cdot \delta \boldsymbol{u}); \quad (10)$$

$$\nabla \cdot \delta \boldsymbol{B} = 0. \quad (11)$$

Without any loss of generality, assume $\boldsymbol{B}_0 = B_0 \hat{\boldsymbol{z}}$. We further assume no local gradients in the background plasma variables and that they are stationary, i.e., $\rho_0$, $\boldsymbol{U}_0$, $P_0$, and $\boldsymbol{B}_0$ are constant.

To identify the linear modes admitted by Equations (7)–(11), we begin by following the classical analysis of Lighthill (1960). On setting $\Delta \equiv \nabla \cdot \delta \boldsymbol{u}$ and $\Gamma \equiv \partial \delta u_z / \partial z$, we obtain the wave equation

$$\frac{D^2 \Delta}{Dt^2} = a_0^2 \nabla^2 \Delta + V_{A0}^2 \nabla^2 (\Delta - \Gamma), \quad (12)$$

where the square of the background sound and Alfvén speeds are $a_0^2 = \gamma P_0/\rho_0$ and $V_{A0}^2 = B_0^2/\mu_0 \rho_0$, respectively, and $D/Dt \equiv \partial/\partial t + \boldsymbol{U}_0 \cdot \nabla$ is the Lagrangian time derivative with respect to the mean flow velocity $\boldsymbol{U}_0$. If $\boldsymbol{\xi} \equiv \nabla \times \boldsymbol{U}$ denotes the fluid vorticity, the linearized vorticity is simply $\delta \xi = \nabla \times \delta \boldsymbol{u}$. It then follows that the $z$-component of the perturbed vorticity, $\delta \xi_z = -\partial \delta u_x/\partial y + \partial \delta u_y/\partial x$, satisfies the Alfvén wave equation

$$\frac{D^2 \delta \xi_z}{Dt^2} = V_{A0}^2 \frac{\partial^2 \delta \xi_z}{\partial z^2}. \quad (13)$$

Hence, the $z$-component of the vorticity propagates along the mean magnetic field at the Alfvén speed $V_{A0}$. As we discuss further below, the $z$-component of the vorticity introduces a perpendicular wavenumber into the Alfvén dispersion relation, and when the angle of propagation is orthogonal to the mean magnetic field, Equation (13) describes a nonpropagating vortical structure. The gradient in $\delta u_z$ along the mean magnetic field is coupled to the compressive component of the fluctuating velocity $\delta \boldsymbol{u}$ and propagates at the sound speed according to

$$\frac{D^2 \Gamma}{Dt^2} = a_0^2 \frac{\partial^2 \Delta}{\partial z^2}. \quad (14)$$

Equations (12)–(14) govern the propagating modes supported by the MHD equations and correspond to the fast and slow magnetosonic modes and the Alfvén modes, as we discuss further below. From Equation (12) or (14), the assumption that $\Delta = 0$ (i.e., solenoidal or incompressible fluctuations) implies that $\Gamma = 0$, the simplest choice of which is $\delta u_z = 0$.

Consider now equations for the nonpropagating modes. Evidently, from Equation (6), the perturbed entropy $\delta s = C_V(\delta p/P_0 - \gamma \delta \rho/\rho_0)$ is governed by the advection equation

$$\frac{D \delta s}{Dt} = \frac{\partial \delta s}{\partial t} + \boldsymbol{U}_0 \cdot \nabla \delta s = 0. \quad (15)$$

Besides the propagating $z$-component of the vorticity $\delta \xi_z$ mentioned above, there is a separate nonpropagating purely magnetic mode component. From Equation (10), incompressibility ($\Delta = 0$, $\delta B_z = 0$, $\delta u_z = 0$) yields the advection equation for fluctuations $\delta \boldsymbol{B}$,

$$\frac{D \delta \boldsymbol{B}_\perp}{Dt} = \frac{\partial \delta \boldsymbol{B}_\perp}{\partial t} + \boldsymbol{U}_0 \cdot \nabla \delta \boldsymbol{B}_\perp = 0, \quad (16)$$

where $\delta \boldsymbol{B}_\perp = (\delta B_x(x, y), \delta B_y(x, y))$. Unlike the Alfvénic fluctuations, the advected magnetic mode is a purely magnetic mode and not coupled to the fluid. Because $\nabla \cdot \delta \boldsymbol{B}_\perp = 0$, this 2D mode can be considered an advected structure with $\delta \boldsymbol{B}_\perp = \delta B(-\sin\phi, \cos\phi)$ in spherical coordinates (below) and is a linearized form of magnetic flux rope or magnetic island when projected onto a 2D plane orthogonal to the mean magnetic field $\boldsymbol{B}_0$. Such advected structures have been observed recently by Zhao et al. (2023), who used data from the four Magnetospheric Multiscale spacecraft to identify features of nonpropagating structures with frequencies close to zero in the plasma rest frame.

Unlike the magnetic island modes, the incompressible hydrodynamical vortical modes are coupled to the magnetic field, because $\Delta = 0$ implies that (Zank et al. 2017)

$$\frac{D^2 \delta \boldsymbol{\xi}}{Dt^2} = V_{A0}^2 \frac{\partial^2 \delta \boldsymbol{\xi}}{\partial z^2}. \quad (17)$$

As discussed above, for fluctuations propagating orthogonally to the mean magnetic field, the 2D $z$-component of the vorticity is advected only and the 2D transverse fluctuations $\delta \boldsymbol{u}_\perp \equiv (\delta u_x(x, y), \delta u_y(x, y))$ satisfy

$$\frac{D \delta \xi_z}{Dt} = \frac{\partial \delta \xi_z}{\partial t} + \boldsymbol{U}_0 \cdot \nabla \delta \xi_z = 0. \quad (18)$$

Unless a specific 2D configuration is considered, as may be the case for the solar wind when the mean flow and magnetic field are orthogonal, Equation (18) is unnecessary and the Alfvén wave Equation (13) is sufficient.

Magnetic flux ropes or their equivalent 2D projection, magnetic islands, are observed throughout the solar wind on all scales (e.g., Veltri 1999; Moldwin et al. 2000; Telloni et al. 2013; Trenchi et al. 2013; Zank et al. 2014, 2015; Khabarova et al. 2015, 2016; Khabarova & Zank 2017; Adhikari et al. 2019; Chen et al. 2019; Malandraki et al. 2019; Zhao et al. 2019, 2021a).

The advection Equations (15) and (16) add two further modes that need to be considered in any mode decomposition procedure, i.e., the advected entropy mode and the advected purely magnetic mode that describes magnetic islands.

A spectral analysis of the mode Equations (12)–(16) yields the dispersion equation and eigenrelations for each mode. As usual, we adopt normal modes $\delta \hat{\Psi} \exp[i(\omega t - \boldsymbol{k} \cdot \boldsymbol{x})]$, where $\delta \hat{\Psi}$ is the Fourier transform of $\delta \Psi$, $\omega$ the frequency, $\boldsymbol{k}$ the wavenumber, and $\omega' \equiv \omega - \boldsymbol{U}_0 \cdot \boldsymbol{k}$ the Doppler-shifted frequency. The Fourier transforms of Equations (12)–(16) or (7)–(11) yield the dispersion equations and eigenrelations listed below. The wavenumber vector is expressed in spherical coordinates $\boldsymbol{k} = k(\cos\phi \sin\theta, \sin\phi \sin\theta, \cos\theta)$ with respect to the mean magnetic field $\boldsymbol{B}_0 = B_0 \hat{\boldsymbol{z}}$.

*Fast (f)/slow (s) magnetosonic modes*. Equations (12) and (14) yield the fast and slow magnetosonic modes that are governed by the dispersion relation,

$$\omega' = \pm V_{f,s} k; \quad (19)$$

$$\omega'^2 = \frac{1}{2}[(a_0^2 + V_{A0}^2)k^2 \pm \sqrt{(a_0^2 + V_{A0}^2)^2 k^4 - 4a_0^2 V_{A0}^2 k^4 \cos^2\theta}] = V_{f,s}^2 k^2, \quad (20)$$

where fast ($f$) corresponds to the "+" root and slow ($s$) to the "−" root in Equation (20). In the eigenrelations that follow, we use the superscript notation "$fs\pm$" to indicate the fast ($f$) or slow ($s$) mode and $\pm$ to indicate the positive or negative choice of root in Equation (19). We will sometimes refer to the positive or negative root in (19) as corresponding to "forward" or "backward" propagating fast/slow magnetosonic modes. The fast/slow-mode eigenrelations are all expressed conveniently in terms of the fluctuating pressure $\delta\hat{p}^{fs\pm}$,

$$\frac{\delta\hat{\rho}^{fs\pm}}{\rho_0} = \frac{\delta\hat{p}^{fs\pm}}{\rho_0 a_0^2}; \quad (21)$$

$$\frac{\delta\hat{u}_{x,y}^{fs\pm}}{U_0} = \frac{V_{f,s\pm}}{U_0}\frac{V_{f,s}^2 k_{x,y}^{fs\pm}/k^{fs\pm}}{V_{f,s}^2 - V_{A0}^2(k_z^{fs\pm})^2/(k^{fs\pm})^2}\frac{\delta\hat{p}^{fs\pm}}{\rho_0 a_0^2}; \quad (22)$$

$$\frac{\delta\hat{u}_z^{fs\pm}}{U_0} = \frac{M_{fs\pm}k_z^{fs\pm}/k^{fs\pm}}{M_0^2}\frac{\delta\hat{p}^{fs\pm}}{\rho_0 a_0^2}; \quad (23)$$

$$\frac{\delta\hat{B}_{x,y}^{fs\pm}}{B_0} = \frac{-V_{f,s}^2 k_{x,y}^{fs\pm}k_z^{fs\pm}/(k^{fs\pm})^2}{V_{f,s}^2 - V_{A0}^2(k_z^{fs\pm})^2/(k^{fs\pm})^2}\frac{\delta\hat{p}^{fs\pm}}{\rho_0 a_0^2}; \quad (24)$$

$$\frac{\delta\hat{B}_z^{fs\pm}}{B_0} = \frac{V_{fs}^2 - a_0^2(k_z^{fs\pm})^2/(k^{fs\pm})^2}{V_{f,s}^2}\frac{\delta\hat{p}^{fs\pm}}{\rho_0 a_0^2}, \quad (25)$$

where $U_0 = |\boldsymbol{U}_0|$, $M_0 \equiv U_0/a_0$ is the acoustic Mach number and $M_{fs\pm} \equiv U_0/V_{f,s\pm}$ the fast/slow forward/backward magnetosonic Mach number. Equations (21)–(25) are the eigenrelations for four of the waves.

*Alfvén modes*. The dispersion equation and the eigenrelations for the forward (+) and backward (−) Alfvén waves are derived from Equations (17), (10), and $\nabla\cdot\delta\boldsymbol{u} = 0$ and listed below. It is convenient to introduce the wavenumber vector in spherical coordinates $\boldsymbol{k} = k(\cos\phi\sin\theta, \sin\phi\sin\theta, \cos\theta) = (\boldsymbol{k}_\perp, k_\parallel) = \boldsymbol{k}_\perp + \boldsymbol{k}_\parallel$, where $\phi$ is the phase and $\theta$ the angle between $\boldsymbol{k}$ and the $z$-axis (parallel to $\boldsymbol{B}_0$). To distinguish the angles made by an Alfvén wave, we use the notation $\phi^A$, $\theta^A$ here, and similarly for the other modes. In this case, we express the eigenrelations in terms of the Alfvénic fluctuation speed $\delta\hat{u}^A = |\delta\hat{\boldsymbol{u}}^A|$ as follows:

$$\omega' = \pm V_{A0}k_z; \quad (26)$$

$$\delta\hat{\rho}^A = 0; \quad \delta\hat{p}^A = 0; \quad \delta\hat{u}_z^A = 0; \quad \delta\hat{B}_z^A = 0; \quad (27)$$

$$\delta\hat{\boldsymbol{u}}_\perp^A = \delta\hat{u}^A(-\sin\phi^A, \cos\phi^A) \equiv \delta\hat{u}^A(-\beta^A, \alpha^A); \quad (28)$$

$$\frac{\delta\hat{\boldsymbol{B}}_\perp^A}{B_0} = \mp\frac{\delta\hat{\boldsymbol{u}}_\perp^A}{V_{A0}} = \mp M_{A0}\frac{\delta\hat{u}_\perp^A}{U_0}(-\sin\phi^A, \cos\phi^A); \quad (29)$$

$$\delta\hat{j}_z^A = \pm\frac{i\rho_0 V_{A0}k_\perp^A}{B_0}\delta\hat{u}^A, \quad (30)$$

where $k_\perp = |\boldsymbol{k}_\perp|$. We note that, for $\theta^A = 0°$, $k_z^A = k^A\cos\theta^A = k^A \neq 0$ and $k_\perp^A = 0$ (i.e., propagating and nonpolarized), whereas for $\theta^A = \pi/2$, $k_\perp^A \neq 0$ and $k_z^A = 0$. The latter case does not propagate.

*Entropy modes*. The linearized form Equation (6) allows the eigenrelations to be expressed as follows:

$$\omega' = 0; \quad (31)$$

$$\delta\hat{s}^e \neq 0; \quad \delta\hat{\rho}^e \text{ arbitrary}; \quad \delta\hat{p}^e = 0; \quad \delta\hat{\boldsymbol{u}}^e = 0; \quad \delta\hat{\boldsymbol{B}}^e = 0. \quad (32)$$

*Magnetic island modes*. Similarly, using Equation (16) allows us to express the eigenrelations in terms of the magnetic field fluctuation $\delta\hat{B}^i = |\delta\hat{\boldsymbol{B}}^i|$ as follows:

$$\omega' = 0; \quad (33)$$

$$\delta\hat{\rho}^i = 0; \quad \delta\hat{p}^i = 0; \quad \delta\hat{\boldsymbol{u}}^i = 0; \quad \delta\hat{B}_z^i = 0; \quad (34)$$

$$\delta\hat{\boldsymbol{B}}_\perp^i = \delta\hat{B}^i(-\sin\phi^i, \cos\phi^i) = \delta\hat{B}^i(-\beta^i, \alpha^i). \quad (35)$$

Hence, the modes that need to be considered in an MHD mode-decomposition analysis are (1) two counterpropagating fast magnetosonic modes, (2) two counterpropagating slow magnetosonic modes, (3) two counterpropagating Alfvén modes, (4) an advected entropy mode, and (5) an advected magnetic island mode. This totals eight modes that need to be determined from the set of nine MHD Equations (1)–(5). As we discuss below, only seven of the equations are linearly independent and can thus be used to provide boundary conditions for the mode-decomposition analysis. An additional boundary condition can be introduced that corresponds to the magnetic island mode. The boundary conditions relate to both the amplitudes that comprise the mode-decomposition and the phases of the corresponding constituent modes. Both the methodology and interpretation of prior mode-decomposition approaches that consider only the six propagating wave modes (e.g., Glassmeier et al. 1995; Motschmann et al. 1998; Cho & Lazarian 2003; Zhao et al. 2021b, 2021c, 2022a) need to be reconsidered because they include neither the advected modes nor the phase information.

## 3. Mode Decomposition

### 3.1. The Conservation Laws

The conservation laws of MHD can be expressed as (e.g., Zank 2014)

$$\rho\boldsymbol{U}\cdot\hat{\boldsymbol{n}} = \mathcal{M}_a; \quad (36)$$

$$\rho\boldsymbol{U}\boldsymbol{U}\cdot\hat{\boldsymbol{n}} + \left(P + \frac{1}{2\mu_0}B^2\right)\boldsymbol{I}\cdot\hat{\boldsymbol{n}} - \frac{1}{\mu_0}\boldsymbol{B}\boldsymbol{B}\cdot\hat{\boldsymbol{n}} = \mathcal{M}_o; \quad (37)$$

$$\left(\frac{1}{2}\rho U^2 + \frac{\gamma}{\gamma-1}P + \frac{1}{\mu_0}B^2\right)\boldsymbol{U}\cdot\hat{\boldsymbol{n}} - \frac{1}{\mu_0}\boldsymbol{U}\cdot\boldsymbol{B}\boldsymbol{B}\cdot\hat{\boldsymbol{n}} = \mathcal{E}_T; \quad (38)$$

$$\boldsymbol{U}\boldsymbol{B}\cdot\hat{\boldsymbol{n}} - \boldsymbol{B}\boldsymbol{U}\cdot\hat{\boldsymbol{n}} = \mathcal{B}_F; \quad (39)$$

$$\boldsymbol{B}\cdot\hat{\boldsymbol{n}} = \mathcal{B}_D, \quad (40)$$

where $\mathcal{M}_a$, $\mathcal{M}_o$, $\mathcal{E}_T$, $\mathcal{B}_F$, and $\mathcal{B}_D$ are constants, and $\hat{\boldsymbol{n}}$ is the normal to the surface across which the respective fluxes are transported. We consider a measurement made "instantaneously" by a single spacecraft in the solar wind (or generally a moving plasma) that yields the plasma and magnetic field amplitudes $\delta\Psi_m = (\delta\rho_m, \delta p_m, \delta\boldsymbol{u}_m, \delta\boldsymbol{B}_m)$ at a Doppler-shifted frequency $\omega_m'$. A wavenumber $\boldsymbol{k}_m$ is needed as well, but this cannot be measured directly by a single spacecraft, and in

practice, we will need to use various approximate methods (e.g., Sonnerup & Scheible 1998; Santolik et al. 2003; Knetter et al. 2004; Zhao et al. 2021c) to infer $\boldsymbol{k}_m$. Because the $\delta\Psi_m$ variables are measured at a particular frequency as they are swept past the spacecraft, we define $\hat{\boldsymbol{n}}$ to be in the direction of the mean flow vector $\boldsymbol{U}_0$, i.e., the surface across which the fluctuations are transported in a plane perpendicular to $\boldsymbol{U}_0$. Having specified the mean magnetic field $\boldsymbol{B}_0 = B_0\hat{z}$, we may without loss of generality rotate the mean flow vector $\boldsymbol{U}_0$ into the $(x, z)$-plane (Figure 1) so that $\boldsymbol{U}_0 = U_0(\sin\psi, 0, \cos\psi)$, where $\psi$ is the angle between $\boldsymbol{U}_0$ and $\hat{z}$. Hence, $\hat{\boldsymbol{n}} = (\sin\psi, 0, \cos\psi)$ and $\psi \in [0, \pi]$.

On linearizing Equations (36)–(40), we obtain at the leading order

$$O(1):\ \rho_0 U_0 = \text{const.}; \tag{41}$$

$$\rho_0 U_0^2 \sin\psi + (P_0 + B_0^2/(2\mu_0))\sin\psi = \text{const.}; \tag{42}$$

$$\rho_0 U_0^2 \cos\psi + (P_0 + B_0^2/(2\mu_0))\cos\psi - B_0^2/\mu_0 \cos\psi = \text{const} \tag{43}$$

$$\frac{1}{2}U_0^2 + \frac{a_0^2}{\gamma - 1} + V_{A0}^2 \sin^2\psi = \text{const.}; \tag{44}$$

$$U_0 B_0 \sin^2\psi = \text{const.}; \tag{45}$$

$$B_0 \cos\psi = \text{const.}, \tag{46}$$

and at the next order,

$$O(\delta\Psi):\ U_0\delta\rho + \rho_0(\delta u_x \sin\psi + \delta u_z \cos\psi) = \text{const.}; \tag{47}$$

$$U_0^2 \sin\psi\delta\rho + \rho_0 U_0(1 + \sin^2\psi)\delta u_x + \rho_0 U_0 \sin\psi\cos\psi\delta u_z + \delta p \sin\psi + \frac{B_0}{\mu_0}(\delta B_z \sin\psi - \delta B_x \cos\psi) = \text{const.}; \tag{48}$$

$$\rho_0 U_0 \delta u_y - \frac{B_0}{\mu_0}\cos\psi\delta B_y = \text{const.}; \tag{49}$$

$$U_0^2 \cos\psi\delta\rho + \rho_0 U_0 \cos\psi\sin\psi\delta u_x + \rho_0 U_0(1 + \cos^2\psi)\delta u_z + \delta p\cos\psi - \frac{B_0}{\mu_0}(\sin\psi\delta B_x - \cos\psi\delta B_z) = \text{const.}; \tag{50}$$

$$\frac{1}{2}U_0^2\frac{\delta\rho}{\rho_0} + (\mathcal{E}_T + U_0^2)\sin\psi\frac{\delta u_x}{U_0} + (\mathcal{E}_0 + U_0^2)\cos\psi\frac{\delta u_z}{U_0} + \frac{a_0^2}{\gamma - 1}\frac{\delta p}{P_0} - 2V_{A0}^2\left(\sin\psi\cos\psi\frac{\delta B_x}{B_0} - \sin^2\psi\frac{\delta B_z}{B_0}\right) = \text{const.}; \tag{51}$$

$$B_0 \cos\psi\delta u_x - U_0\cos^2\psi\delta B_x + U_0\sin\psi\cos\psi\delta B_z = \text{const.}; \tag{52}$$

$$B_0\cos\psi\delta u_y - U_0\delta B_y = \text{const.}; \tag{53}$$

$$U_0\sin\psi\cos\psi\delta B_x - U_0\sin^2\psi\delta B_z - B_0\sin\psi\delta u_x = \text{const.}; \tag{54}$$

$$\delta B_x \sin\psi + \delta B_z\cos\psi = \text{const.}, \tag{55}$$

where $\mathcal{E}_0 \equiv (1/2)U_0^2 + a_0^2/(\gamma - 1)$ and $\mathcal{E}_T \equiv \mathcal{E}_0 + V_{A0}^2$. We note that Equation (54) is a simple linear combination of the $x$-component of the induction Equation (52) (due in part to the choice of surface corresponding to the normal $\hat{\boldsymbol{n}}$) and the divergence condition (55) is used implicitly in the preceding equations. Accordingly, (54) and (55) are not independent, and therefore the $O(\delta\Psi)$ set of independent perturbed conservation laws numbers seven, corresponding to Equations (47)–(53).

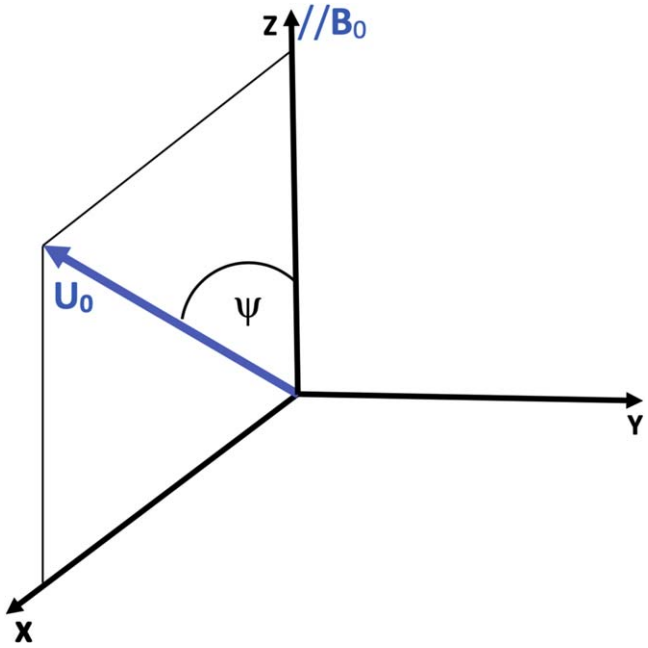


**Figure 1.** The assumed coordinate system with the mean magnetic field $\boldsymbol{B}_0$ aligned along the $z$-axis and the mean flow vector $\boldsymbol{U}_0$ rotated into the $(x, y)$-plane without loss of generality, making an angle $\psi$ with the mean magnetic field aligned $z$-axis.

Besides the above boundary conditions, we need to include boundary conditions for the advected 2D magnetic island fluctuations. One can consider this from two perspectives, either beginning with a fully compressible 2D MHD description in which the mean magnetic field is normal to the 2D plane, or specializing to a 2D incompressible description from the compressible 3D MHD equations. Because the former approach is interesting, is related to the 2D hydrodynamic description of Appendix A, and was used by Zank et al. (2021a) in discussing the transmission of turbulence across a perpendicular shock wave, we utilize this approach.

On considering the 2D compressible MHD equations in a plane orthogonal to the mean magnetic field $\boldsymbol{B}_0 = B_0\hat{z}$, i.e., assuming all plasma and magnetic field variables satisfy $\Psi = \Psi(x, y)$ and linearizing as before with the exception that $\boldsymbol{B} \to \delta\boldsymbol{B}$, we find that the perturbed nonconservation form of the equations separates into exclusively hydrodynamic

$$\begin{aligned}
&\frac{\partial\delta\rho}{\delta t} + \boldsymbol{U}_0\cdot\nabla\delta\rho + \rho_0\nabla\cdot\delta\boldsymbol{u} = 0;\\
&\frac{\partial\delta\boldsymbol{u}}{\partial t} + \boldsymbol{U}_0\cdot\nabla\delta\boldsymbol{u} = -\frac{1}{\rho_0}\nabla\delta p;\\
&\frac{\partial\delta p}{\delta t} + \boldsymbol{U}_0\cdot\nabla\delta p + \gamma p_0\nabla\cdot\delta\boldsymbol{u} = 0,
\end{aligned} \tag{56}$$

and magnetic field components (Zank et al. 2021a),

$$\frac{\partial\delta\boldsymbol{B}}{\partial t} + \boldsymbol{U}_0\cdot\nabla\delta\boldsymbol{B} = 0; \quad \nabla\cdot\delta\boldsymbol{B} = 0. \tag{57}$$

The corresponding perturbed conservation laws for the hydrodynamic component are presented in Appendix A and

are not repeated here. The perturbed 2D conservation of magnetic flux equation, $\boldsymbol{uB}\cdot\hat{\boldsymbol{n}}-\boldsymbol{Bu}\cdot\hat{\boldsymbol{n}}=0$, yields

$$\delta B_x = \text{const.} \quad \text{or} \quad \delta B_x = \delta B_{mx}; \tag{58}$$

$$\delta B_y = \text{const.} \quad \text{or} \quad \delta B_y = \delta B_{my}. \tag{59}$$

Equations (58) and (59) provide the needed further conservation laws.

### 3.2. Mode Decomposition

The linearized fluctuation Equations (47)–(53) and (58) and (59) contain information about both the amplitudes and the phases of the constituent MHD modes. The measurement of a particular solar wind fluctuation is made at a particular frequency $\omega_m'$ in the spacecraft frame, i.e., a Doppler-shifted frequency $\omega_m'\neq 0$ with a corresponding wavenumber $\boldsymbol{k}_m$. From the dispersion relations presented in Section 2, we can express the normal-mode representation $\exp i(\omega t-\boldsymbol{k}\cdot\boldsymbol{x})$ in terms of the Doppler frequency, i.e.,

$$\omega t-\boldsymbol{k}\cdot\boldsymbol{x}=\omega' t+\boldsymbol{U}_0\cdot\boldsymbol{k}t-\boldsymbol{k}\cdot\boldsymbol{x}=\omega' t-\boldsymbol{k}\cdot\boldsymbol{x}', \tag{60}$$

where $\boldsymbol{x}'\equiv\boldsymbol{x}-\boldsymbol{U}_0 t$ is a comoving spatial coordinate in the fluid frame. Consider, e.g., the measured density fluctuation$\delta\rho_m$ that can be expressed as a superposition of an entropy fluctuation and forward and backward fast and slow magnetosonic modes, or $\delta\rho_m=\delta\rho^e+\delta\rho^{f+}+\delta\rho^{f-}+\delta\rho^{s+}+\delta\rho^{s-}$ where $\delta\rho^e$ and $\delta\rho^{fs\pm}$ denote the density fluctuations associated with an entropy, forward and backward fast ($f\pm$) and slow ($s\pm$) magnetosonic modes, respectively. Expressed equivalently in terms of normal modes, we have

$$\begin{aligned}\delta\hat{\rho}_m e^{i(\omega_m' t-\boldsymbol{k}_m\cdot\boldsymbol{x}')} &= \delta\hat{\rho}^e e^{i(\omega_e t-\boldsymbol{k}^e\cdot\boldsymbol{x})}+\delta\hat{\rho}^{f+}e^{i(\omega_{f+}t-\boldsymbol{k}^{f+}\cdot\boldsymbol{x})}\\ &\quad+\delta\hat{\rho}^{f-}e^{i(\omega_{f-}t-\boldsymbol{k}^{f-}\cdot\boldsymbol{x})}+\delta\hat{\rho}^{s+}e^{i(\omega_{s+}t-\boldsymbol{k}^{s+}\cdot\boldsymbol{x})}\\ &\quad+\delta\hat{\rho}^{s-}e^{i(\omega_{s-}t-\boldsymbol{k}^{s-}\cdot\boldsymbol{x})}\\ &=\delta\hat{\rho}^e e^{i(\omega_e' t-\boldsymbol{k}^e\cdot\boldsymbol{x}')}+\delta\hat{\rho}^{f+}e^{i(\omega_{f+}' t-\boldsymbol{k}^{f+}\cdot\boldsymbol{x}')}\\ &\quad+\delta\hat{\rho}^{f-}e^{i(\omega_{f-}' t-\boldsymbol{k}^{f-}\cdot\boldsymbol{x}')}+\delta\hat{\rho}^{s+}e^{i(\omega_{s+}' t-\boldsymbol{k}^{s+}\cdot\boldsymbol{x}')}\\ &\quad+\delta\hat{\rho}^{s-}e^{i(\omega_{s-}' t-\boldsymbol{k}^{s-}\cdot\boldsymbol{x}')},\end{aligned} \tag{61}$$

where $\omega_{e,fs\pm}'$ and $\boldsymbol{k}^{e,fs\pm}$ denote the Doppler frequency and wavenumber of the entropy ($e$) and forward and backward fast ($f\pm$) and slow ($s\pm$) magnetosonic modes, respectively. Because measurements are made by a "stationary" spacecraft, the measurement is made at $\boldsymbol{x}=0$, implying that $\boldsymbol{x}'=-\boldsymbol{U}_0 t$. Here, $t$ is the time elapsed after measurement, which for notational convenience we denote by $\Delta t$. The decomposition (61) is valid only for a time short enough that the measured fluctuations can be regarded as a coherent superposition of the individual or constituent modes. Thus, if the spatial scale of the measured fluctuation is $\ell$, then $\ell/\Delta t>V_{\rm ph}=\omega/k$, determines the "decoherence time" of the measured fluctuation, i.e., $\Delta t<\ell k/\omega$, where $V_{\rm ph}$ is the largest phase velocity of the constituent modes. Hence, for sufficiently small $\Delta t$, the density fluctuation $\delta\rho_m$ measured at $\boldsymbol{x}=0$ can be expressed as

$$\begin{aligned}\delta\hat{\rho}_m e^{i\Delta t(\omega_m'+\boldsymbol{U}_0\cdot\boldsymbol{k}_m)} &= \delta\hat{\rho}^e e^{i\Delta t\boldsymbol{U}_0\cdot\boldsymbol{k}^e}\\ &+\delta\hat{\rho}^{f+}e^{i\Delta t(\omega_m'+\boldsymbol{U}_0\cdot\boldsymbol{k}^{f+})}+\delta\hat{\rho}^{f-}e^{i\Delta t(-\omega_m'+\boldsymbol{U}_0\cdot\boldsymbol{k}^{f-})}\\ &+\delta\hat{\rho}^{s+}e^{i\Delta t(\omega_m'+\boldsymbol{U}_0\cdot\boldsymbol{k}^{s+})}+\delta\hat{\rho}^{s-}e^{i\Delta t(-\omega_m'+\boldsymbol{U}_0\cdot\boldsymbol{k}^{s-})},\end{aligned} \tag{62}$$

after using the dispersion relations $\omega_e'=0$, $\omega_{f+}'=\omega_m'=+V_f k^{f+}$, $\omega_{f-}'=-V_f k^{f-}=-\omega_m'$, $\omega_{s+}'=\omega_m'=+V_s k^{s+}$, and $\omega_{s-}'=-V_s k^{s-}=-\omega_m'$. Because the decoherence time is small, we can Taylor expand about $\omega_m'\Delta t\ll 1$ generally as

$$\begin{aligned}&\delta\hat{\psi}\cos\Delta t(\omega'+\boldsymbol{U}_0\cdot\boldsymbol{k})\\ &=\delta\hat{\psi}\sum_{n=0}^{\infty}(-1)^n(\Delta t)^{2n}\frac{(\omega'+\boldsymbol{U}_0\cdot\boldsymbol{k})^{2n}}{(2n)!}\\ &=\delta\hat{\psi}-\frac{1}{2}\delta\hat{\psi}(\Delta t)^2(\omega'+\boldsymbol{U}_0\cdot\boldsymbol{k})^2+\cdots.\end{aligned} \tag{63}$$

Thus, Equation (62) becomes, to leading and first order,

$$n=0:\ \ \delta\hat{\rho}_m=\delta\hat{\rho}^e+\delta\hat{\rho}^{f+}+\delta\hat{\rho}^{f-}+\delta\hat{\rho}^{s+}+\delta\hat{\rho}^{s-}; \tag{64}$$

$$\begin{aligned}n=1:\ \ &\delta\hat{\rho}_m(\omega_m'+\boldsymbol{U}_0\cdot\boldsymbol{k}_m)^2\\ &=\delta\hat{\rho}^e(\boldsymbol{U}_0\cdot\boldsymbol{k}^e)^2+\delta\hat{\rho}^{f+}(\omega_m'+\boldsymbol{U}_0\cdot\boldsymbol{k}^{f+})^2\\ &\quad+\delta\hat{\rho}^{f-}(-\omega_m'+\boldsymbol{U}_0\cdot\boldsymbol{k}^{f-})^2\\ &\quad+\delta\hat{\rho}^{s+}(\omega_m'+\boldsymbol{U}_0\cdot\boldsymbol{k}^{s+})^2+\delta\hat{\rho}^{s-}(-\omega_m'+\boldsymbol{U}_0\cdot\boldsymbol{k}^{s-})^2,\end{aligned} \tag{65}$$

illustrating that (64) relates the measured amplitude of the density to the amplitudes of the constituent modes (which nonetheless require phase information through the respective eigenrelations) and (65) couples the observed phase (wavenumber $\boldsymbol{k}_m$ and frequency $\omega_m'$) information to the phases of the individual constituent MHD modes. The remaining fluctuating plasma and magnetic variables can be expressed similarly as follows:

$$\begin{aligned}&\delta p_m=\delta p^{f+}+\delta p^{f-}+\delta p^{s+}+\delta p^{s-};\\ &n=0:\ \ \delta\hat{p}_m=\delta\hat{p}^{f+}+\delta\hat{p}^{f-}+\delta\hat{p}^{s+}+\delta\hat{p}^{s-};\\ &n=1:\ \ \delta\hat{p}_m(\omega_m'+\boldsymbol{U}_0\cdot\boldsymbol{k}_m)^2\\ &\quad=\delta\hat{p}^{f+}(\omega_m'+\boldsymbol{U}_0\cdot\boldsymbol{k}^{f+})^2+\delta\hat{p}^{f-}(-\omega_m'+\boldsymbol{U}_0\cdot\boldsymbol{k}^{f-})^2\\ &\quad\quad+\delta\hat{p}^{s+}(\omega_m'+\boldsymbol{U}_0\cdot\boldsymbol{k}^{s+})^2+\delta\hat{p}^{s-}(-\omega_m'+\boldsymbol{U}_0\cdot\boldsymbol{k}^{s-})^2.\end{aligned} \tag{66}$$

For the velocity and magnetic field fluctuation vectors, we incorporate both magnetic flux ropes/islands and counterpropagating Alfvén modes. For the reasons discussed above, we do not include the vortical mode unless considering the special case of orthogonal mean flow and magnetic field vectors. The expansions for the velocity and magnetic field fluctuations are given by the following system of equations:

$$\begin{aligned}&\delta\boldsymbol{u}_m=\delta\boldsymbol{u}^{f+}+\delta\boldsymbol{u}^{f-}+\delta\boldsymbol{u}^{s+}+\delta\boldsymbol{u}^{s-}+\delta\boldsymbol{u}^{A+}+\delta\boldsymbol{u}^{A-};\\ &n=0:\ \ \delta\hat{\boldsymbol{u}}_m=\delta\hat{\boldsymbol{u}}^{f+}+\delta\hat{\boldsymbol{u}}^{f-}+\delta\hat{\boldsymbol{u}}^{s+}+\delta\hat{\boldsymbol{u}}^{s-}+\delta\hat{\boldsymbol{u}}^{A+}+\delta\hat{\boldsymbol{u}}^{A-}\\ &n=1:\ \ \delta\hat{\boldsymbol{u}}_m(\omega_m'+\boldsymbol{U}_0\cdot\boldsymbol{k}_m)^2=\delta\hat{\boldsymbol{u}}^{f+}(\omega_m'+\boldsymbol{U}_0\cdot\boldsymbol{k}^{f+})^2\\ &+\delta\hat{\boldsymbol{u}}^{f-}(-\omega_m'+\boldsymbol{U}_0\cdot\boldsymbol{k}^{f-})^2+\delta\hat{\boldsymbol{u}}^{s+}(\omega_m'+\boldsymbol{U}_0\cdot\boldsymbol{k}^{s+})^2\\ &+\delta\hat{\boldsymbol{u}}^{s-}(-\omega_m'+\boldsymbol{U}_0\cdot\boldsymbol{k}^{s-})^2+\delta\hat{\boldsymbol{u}}^{A+}(\omega_{A+}'+\boldsymbol{U}_0\cdot\boldsymbol{k}^{A+})^2\\ &+\delta\hat{\boldsymbol{u}}^{A-}(\omega_{A-}'+\boldsymbol{U}_0\cdot\boldsymbol{k}^{A-})^2,\end{aligned} \tag{67}$$

and

$$\delta \boldsymbol{B}_m = \delta \boldsymbol{B}^i + \delta \boldsymbol{B}^{f+} + \delta \boldsymbol{B}^{f-} + \delta \boldsymbol{B}^{s+} + \delta \boldsymbol{B}^{s-} + \delta \boldsymbol{B}^{A+} + \delta \boldsymbol{B}^{A-};$$
$$n = 0: \delta \hat{\boldsymbol{B}}_m = \delta \hat{\boldsymbol{B}}^i + \delta \hat{\boldsymbol{B}}^{f+} + \delta \hat{\boldsymbol{B}}^{f-} + \delta \hat{\boldsymbol{B}}^{s+} + \delta \hat{\boldsymbol{B}}^{s-} + \delta \hat{\boldsymbol{B}}^{A+}$$
$$+ \delta \hat{\boldsymbol{B}}^{A-}; n = 1: \delta \hat{\boldsymbol{B}}_m(\omega'_m + \boldsymbol{U}_0 \cdot \boldsymbol{k}_m)^2 = \delta \hat{\boldsymbol{B}}^i(\boldsymbol{U}_0 \cdot \boldsymbol{k}^i)^2$$
$$+ \delta \hat{\boldsymbol{B}}^{f+}(\omega'_m + \boldsymbol{U}_0 \cdot \boldsymbol{k}^{f+})^2 + \delta \hat{\boldsymbol{B}}^{f-}(-\omega'_m + \boldsymbol{U}_0 \cdot \boldsymbol{k}^{f-})^2$$
$$+ \delta \hat{\boldsymbol{B}}^{s+}(\omega'_m + \boldsymbol{U}_0 \cdot \boldsymbol{k}^{s+})^2 + \delta \hat{\boldsymbol{B}}^{s-}(-\omega'_m + \boldsymbol{U}_0 \cdot \boldsymbol{k}^{s-})^2$$
$$+ \delta \hat{\boldsymbol{B}}^{A+}(\omega'_{A+} + \boldsymbol{U}_0 \cdot \boldsymbol{k}^{A+})^2$$
$$+ \delta \hat{\boldsymbol{B}}(\omega'_{A-} + \boldsymbol{U}_0 \cdot \boldsymbol{k}^{A-})^2. \tag{68}$$

From the discussion above, we have the nine unknown amplitudes, $\delta \hat{\boldsymbol{B}}^i_\perp$, $\delta \hat{\rho}^e$, $\delta \hat{p}^{f\pm}$, $\delta \hat{p}^{s\pm}$, and $\delta \hat{u}^{A\pm}$ for the eight modes (counting $\delta B^i_{x,y}$ separately), and we have the nine boundary conditions (47)–(53) and (58) and (59). However, as shown in Section 2, the linear mode eigenrelations are all functions of the unknown phase information $\boldsymbol{k}^e$, $\boldsymbol{k}^{f\pm}$, $\boldsymbol{k}^{s\pm}$, $\boldsymbol{k}^{A\pm}$, and $\boldsymbol{k}^i$, which gives a further $8 \times 3 = 24$ unknowns. In the next two subsections, we show how to reduce this set of unknowns to a well-posed linear problem that admits an unique solution to the mode-decomposition problem.

### 3.3. The Amplitude Matrix

A single spacecraft measures the plasma fluctuation amplitudes $\delta \rho_m$, $\delta \boldsymbol{u}_m$, $\delta p_m$, and $\delta \boldsymbol{B}_m$ at a Doppler-shifted frequency $\omega'_m$ and (inferred) wavenumber $\boldsymbol{k}_m$. For times shorter than the decoherence time of the measured fluctuation, we can reconstruct the fluctuation through the linear superposition of the constituent modes admitted by the linearized MHD equations. As described in Section 2, eight distinct modes are supported by the linearized MHD equations. The linearized conservation laws (47)–(55) and (58) (or (59)) provide eight fully independent conservation equations.

In view of Equations (47)–(55) and (58), the assumption of (simple) linearity yields a decomposition of an observed fluctuation for which the basis set is comprised of eight modes: the entropy, forward, and backward fast and slow magnetosonic; the forward and backward Alfvén modes; and a magnetic island mode.

Consider now the specifics of the decomposition, beginning with, for example, the perturbed conservation Equation (47), which can be expressed as

$$\frac{\delta \rho_m}{\rho_0} + \frac{\delta u_{mx}}{U_0}\sin\phi + \frac{\delta u_{mz}}{U_0}\cos\phi = \frac{\delta \rho}{\rho_0} + \frac{\delta u_x}{U_0}\sin\phi + \frac{\delta u_z}{U_0}\cos\phi. \tag{69}$$

As discussed in Section 3.2, it is possible for $\delta\rho/\rho_0$ to contain contributions from an entropy fluctuation $\delta \hat{\rho}^e$, as well as forward and backward fast and slow magnetosonic modes ($\delta \rho^{f\pm}$, $\delta \rho^{s\pm}$). From (64) (i.e., the $n = 0$ expansion), the corresponding amplitudes may be expressed as

$$\frac{\delta \hat{\rho}_m}{\rho_0} = \frac{\delta \hat{\rho}^e}{\rho_0} + \frac{\delta \hat{\rho}^{f+}}{\rho_0} + \frac{\delta \hat{\rho}^{f-}}{\rho_0} + \frac{\delta \hat{\rho}^{s+}}{\rho_0} + \frac{\delta \hat{\rho}^{s-}}{\rho_0}$$
$$= \frac{\delta \hat{\rho}^e}{\rho_0} + \frac{\delta \hat{p}^{f+}}{\rho_0 a_0^2} + \frac{\delta \hat{p}^{f-}}{\rho_0 a_0^2} + \frac{\delta \hat{p}^{s+}}{\rho_0 a_0^2} + \frac{\delta \hat{p}^{s-}}{\rho_0 a_0^2}, \tag{70}$$

after using the eigenrelation (21). By contrast, the fluctuation $\delta u_x$ on the right-hand side (rhs) of (69) can be composed of compressible forward and backward fast $\delta u_x^{f\pm}$ and slow $\delta u_x^{s\pm}$ magnetosonic modes and the forward and backward Alfvén modes $\delta u_x^{A\pm}$. Hence, we have the mode decomposition for the amplitudes of $\delta u_x$, after using Equations (67) ($n = 0$), (22), and (28):

$$\frac{\delta \hat{u}_{mx}}{U_0} = \frac{\delta \hat{u}_x^{f+}}{U_0} + \frac{\delta \hat{u}_x^{f-}}{U_0} + \frac{\delta \hat{u}_x^{s+}}{U_0} + \frac{\delta \hat{u}_x^{s-}}{U_0} + \frac{\delta \hat{u}_x^{A+}}{U_0} + \frac{\delta \hat{u}_x^{A-}}{U_0}$$
$$= \mathcal{F}_x^{f+}\frac{\delta \hat{p}^{f+}}{\rho_0 a_0^2} + \mathcal{F}_x^{f-}\frac{\delta \hat{p}^{f-}}{\rho_0 a_0^2} + \mathcal{F}_x^{s+}\frac{\delta \hat{p}^{s+}}{\rho_0 a_0^2}$$
$$+ \mathcal{F}_x^{s-}\frac{\delta \hat{p}^{s-}}{\rho_0 a_0^2} - \beta^{A+}\frac{\delta \hat{u}^{A+}}{U_0} - \beta^{A-}\frac{\delta \hat{u}^{A-}}{U_0}, \tag{71}$$

where

$$\mathcal{F}_x^{fs\pm} \equiv \frac{1}{M_0}\frac{V_{fs\pm}}{a_0}\frac{V_{fs}^2 \cos\phi^{fs\pm}\sin\theta^{fs\pm}}{V_{fs}^2 - V_{A0}^2\cos^2\theta^{fs\pm}}. \tag{72}$$

In Equation (72), $V_{fs\pm}$ refers to the forward (+)/backward (−) fast ($f$)/slow ($s$) magnetosonic speed (Equation (20)), which is a function of wavenumber pitch angle $\theta^{fs\pm}$ and $\phi^{fs\pm}$, the corresponding wavenumber gyrophase. $M_0 \equiv U_0/a_0$ is the sonic Mach number of the flow. Finally, $\delta u_z$ on the rhs of (69) can be constructed from the compressible fast and slow magnetosonic modes; hence, from Equations (67), (23), and (27), we have

$$\frac{\delta \hat{u}_z}{U_0} = \frac{\delta \hat{u}_z^{f+}}{U_0} + \frac{\delta \hat{u}_z^{f-}}{U_0} + \frac{\delta \hat{u}_z^{s+}}{U_0} + \frac{\delta \hat{u}_z^{s-}}{U_0}$$
$$= \frac{\cos\theta^{f+}}{M_0}\frac{a_0}{V_{f+}}\frac{\delta \hat{p}^{f+}}{\rho_0 a_0^2} + \frac{\cos\theta^{f-}}{M_0}\frac{a_0}{V_{f-}}\frac{\delta \hat{p}^{f-}}{\rho_0 a_0^2}$$
$$+ \frac{\cos\theta^{s+}}{M_0}\frac{a_0}{V_{s+}}\frac{\delta \hat{p}^{s+}}{\rho_0 a_0^2} + \frac{\cos\theta^{s-}}{M_0}\frac{a_0}{V_{s-}}\frac{\delta \hat{p}^{s-}}{\rho_0 a_0^2}. \tag{73}$$

On combining Equations (70)–(73) in (69), we obtain the first equation in the $(8 \times 8)$ system of linear equations expressed as

$$\boldsymbol{A}\boldsymbol{x} = \boldsymbol{b}, \text{ where } \boldsymbol{A} = (a_{ij}), \boldsymbol{x} = (x_j), \boldsymbol{b} = (b_i), \ i, j = 1 \cdots 8;$$
$$\boldsymbol{x} = \left(\frac{\delta \rho^e}{\rho_0}, \frac{\delta \hat{p}^{f+}}{\rho_0 a_0^2}, \frac{\delta \hat{p}^{f-}}{\rho_0 a_0^2}, \frac{\delta \hat{p}^{s+}}{\rho_0 a_0^2}, \frac{\delta \hat{p}^{s-}}{\rho_0 a_0^2}, \frac{\delta u^{A+}}{U_0}, \frac{\delta u^{A-}}{U_0}, \frac{\delta B^i}{B_0}\right)^t. \tag{74}$$

Although somewhat laborious, the remaining perturbed conservation laws (48)–(53) and (58) can be expressed in terms of the eight modes admitted by the MHD system of equations. The detailed expressions for $\boldsymbol{A}$ and $\boldsymbol{b}$ are listed in Appendix B.

### 3.4. Phase Relations

Evidently, the linearized system $\boldsymbol{A}\boldsymbol{x} = \boldsymbol{b}$ requires the wavenumber angles $\theta$ and $\phi$ of the eight specific modes and these need to be evaluated from the observed Doppler-shifted frequency $\omega'_m (\neq 0)$ (i.e., in the spacecraft frame) of the observed set of fluctuations, the inferred wavenumber $\boldsymbol{k}_m$,

and the respective dispersion relations. Although the MHD case is rather more involved, the 2D hydrodynamic case discussed in Appendix A provides a useful guide to the analysis below.

We show systematically and rigorously how all the phase information can be computed by knowing just one specific set of wave mode angles, i.e., corresponding to one mode—in our case, the forward fast magnetosonic mode $\theta^{f+}$ and $\phi^{f+}$. In principle, any other mode could be used, but the fast magnetosonic mode is the least complicated to work with. We then use the measured specific frequency $\omega'_m$ and (inferred) wavenumber $\boldsymbol{k}_m$ to estimate the values of $\theta^{f+}$ and $\phi^{f+}$.

Let us consider first the simplest case of the entropic wavenumber $\boldsymbol{k}^e$. The entropy mode is a strictly advected density fluctuation, hence $k^e_y = 0$. Because $k^e_x \neq 0$, $k^e_y = k^e \sin\phi^e \sin\theta^e = 0$ implies that $\phi^e = 0$ and hence

$$\begin{aligned} k^e_x &= k^e \sin\theta^e; \\ k^e_z &= k^e \cos\theta^e. \end{aligned} \tag{75}$$

Second, the dispersion relations for the fast and slow magnetosonic modes $\omega'_{fs\pm} = \pm V_{f,s}(\theta^{fs\pm})k^{fs\pm} = \pm\omega'_m$ imply that the magnitude of the fast/slow wavenumber $k^{f\pm}$ can be expressed as $k^{fs\pm} = \omega'_m/V_{f,s}(\theta^{fs\pm})$, provided we know $\theta^{fs\pm}$. These relations allow us to rewrite the $n = 1$ pressure Equation (66) as

$$\begin{aligned} &\delta\hat{p}_m\left(1 + \frac{\boldsymbol{U}_0\cdot\boldsymbol{k}_m}{\omega'_m}\right)^2 = \delta\hat{p}^{f+}(1 + M_f(\theta^{f+})(\sin\psi\cos\phi^{f+} \\ &\sin\theta^{f+} + \cos\psi\cos\theta^{f+})^2 + \delta\hat{p}^{f-}(1 - M_f(\theta^{f-}) \\ &\times(\sin\psi\cos\phi^{f-}\sin\theta^{f-} + \cos\psi\cos\theta^{f-})^2 \\ &+ \delta\hat{p}^{s+}(1 + M_s(\theta^{s+})(\sin\psi\cos\phi^{s+}\sin\theta^{s+} + \cos\psi\cos\theta^{s+}))^2 \\ &+ \delta\hat{p}^{s-}(1 - M_s(\theta^{s-})(\sin\psi\cos\phi^{s-}\sin\theta^{s-} + \cos\psi\cos\theta^{s-}))^2, \end{aligned} \tag{76}$$

after introducing the fast and slow magnetosonic Mach numbers $M_{f,s}(\theta^{fs\pm}) = U_0/V_{f,s}(\theta^{fs\pm})$ and using, e.g.,

$$\begin{aligned} \frac{\boldsymbol{U}_0\cdot\boldsymbol{k}^{f+}}{\omega'_m} &= \frac{U_0}{\omega'_m}(\sin\psi k^{f+}_x + \cos\psi k^{f+}_z) \\ &= \frac{U_0}{V_f(\theta^{f+})}(\sin\psi\cos\phi^{f+}\sin\theta^{f+} + \cos\psi\cos\theta^{f+}), \end{aligned}$$

and similarly for the other terms. A related analysis allows the $n = 1$ density Equation (65) to be expressed as

$$\begin{aligned} &\delta\hat{\rho}_m\left(1 + \frac{\boldsymbol{U}_0\cdot\boldsymbol{k}_m}{\omega'_m}\right)^2 = \delta\hat{\rho}^e\left(\frac{\boldsymbol{U}_0\cdot\boldsymbol{k}^e}{\omega'_m}\right)^2 + \delta\hat{\rho}^{f+} \\ &\times(1 + M_f(\theta^{f+})(\sin\psi\cos\phi^{f+}\sin\theta^{f+} + \cos\psi\cos\theta^{f+}))^2 \\ &+ \delta\hat{\rho}^{f-}(1 - M_f(\theta^{f-})(\sin\psi\cos\phi^{f-}\sin\theta^{f-} \\ &+ \cos\psi\cos\theta^{f-})^2 + \delta\hat{\rho}^{s+}(1 + M_s(\theta^{s+}) \\ &\times(\sin\psi\cos\phi^{s+}\sin\theta^{s+} + \cos\psi\cos\theta^{s+})^2 \\ &+ \delta\hat{\rho}^{s-}(1 - M_s(\theta^{s-})(\sin\psi\cos\phi^{s-}\sin\theta^{s-} + \cos\psi\cos\theta^{s-}))^2, \end{aligned} \tag{77}$$

the primary difference from (76) being the presence of the density term associated with the entropy.

We begin with the pressure Equation (76), because we need to ensure that the $n = 0$ total pressure amplitude relation $\delta\hat{p}_m = \delta\hat{p}^{f+} + \delta\hat{p}^{f-} + \delta\hat{p}^{s+} + \delta\hat{p}^{s-}$ holds. For the fast magnetosonic modes, this requires that we show that the first and second bracketed terms on the rhs of (76) are equal, i.e., that

$$\begin{aligned} &M_f(\theta^{f+})(\sin\psi\cos\phi^{f+}\sin\theta^{f+} + \cos\psi\cos\theta^{f+}) \\ &= -M_f(\theta^{f-})(\sin\psi\cos\phi^{f-}\sin\theta^{f-} + \cos\psi\cos\theta^{f-}). \end{aligned} \tag{78}$$

The fast-mode wave speed $V_f(\theta) \neq 0$ for all $\theta \in [0, \pi]$. Because the fast magnetosonic Mach number $M_f(\theta^{f\pm}) = U_0/V_f(\theta^{f\pm})$ and $V_f(\theta^{f+}) = |V_f(\theta^{f-})| = -V_f(\theta^{f-})$, we have $M_f(\theta^{f+}) = -M_f(\theta^{f-})$. Hence, the bracketed terms on the left and right sides of Equation (78) are satisfied trivially by the relations

$$\left.\begin{aligned} \cos\theta^{f+} &= \cos\theta^{f-} \\ \sin\theta^{f+} &= \sin\theta^{f-} \\ \cos\phi^{f+} &= \cos\phi^{f-} \end{aligned}\right\} \Longrightarrow \begin{cases} \theta^{f-} = \theta^{f+}, \\ \phi^{f^-} = \phi^{f+}, \end{cases} \tag{79}$$

and we restrict $\theta^{f\pm} \in [0, \pi]$. Despite the equal angular relations, the waves are oppositely propagating by virtue of the opposite signs in the dispersion relation that ensured that $M_f(\theta^{f+}) = -M_f(\theta^{f-})$.

The analysis for the slow magnetosonic mode is similar to that for the fast mode, except that the phase speed of the slow mode satisfies $V_s^2(\theta = \pi/2) = 0$ (and $V_s(\theta = 0) = \pm V_{A0}$). Let us consider first $\theta \neq \pi/2$. On introducing $M_s(\theta^{s\pm}) \equiv U_0/V_s(\theta^{s\pm})$, we need to ensure that

$$\begin{aligned} &M_s(\theta^{s+})(\sin\psi\cos\phi^{s+}\sin\theta^{s+} + \cos\psi\cos\theta^{s+}) \\ &= -M_s(\theta^{s-})(\sin\psi\cos\phi^{s-}\sin\theta^{s-} + \cos\psi\cos\theta^{s-}), \end{aligned} \tag{80}$$

as before. To ensure that $M_s(\theta^{s+}) = -M_s(\theta^{fs})$ and that (80) is satisfied, we require that

$$\begin{aligned} \theta^{s-} &= \theta^{s+} \\ \phi^{s^-} &= \phi^{s+}, \end{aligned} \tag{81}$$

hold, and we restrict $\theta^{s\pm} \in [0, \pi]$.

Consider instead $\theta^{s\pm}$ close to $\pi/2$ and the limit $\theta^{s\pm} \to \pi/2$, which implies that $\cos^2\theta^{s\pm} \ll 1$. On using the expansion $\cos\theta \simeq -(\theta - \pi/2) + O((\theta - \pi/2)^2 + \cdots$ for $\theta \simeq \pi/2$, then

$$V_s^{\pm}(\theta \simeq \pi/2) \simeq \pm\frac{1}{\sqrt{2}}\frac{a_0 V_{A0}}{\sqrt{a_0^2 + V_{A0}^2}}\left(\theta - \frac{\pi}{2}\right),$$

from which we obtain the limiting result $M_s(\theta^{s+})/M_s(\theta^{s-}) \simeq -(\theta^{s-} - \pi/2)/(\theta^{s+} - \pi/2)$. If $\theta^{s-} = \theta^{s+}$, then $-(\theta^{s-} - \pi/2)/(\theta^{s+} - \pi/2) = -1$ or $M_s(\theta^{s+})/M_s(\theta^{s-}) \to -1$ for $\theta \simeq \pi/2$. Hence, it follows that the result (81) holds generally for all values of $\theta^{s\pm} \in [0, \pi]$.

As a consequence, the $n = 1$ pressure Equation (76) becomes

$$\begin{aligned} &\delta\hat{p}_m\left(1 + \frac{\boldsymbol{U}_0\cdot\boldsymbol{k}_m}{\omega'_m}\right)^2 = (\delta\hat{p}^{f+} + \delta\hat{p}^{f-})\times(1 + M_f(\theta^{f+}) \\ &(\sin\psi\cos\phi^{f+}\sin\theta^{f+} + \cos\psi\cos\theta^{f+}))^2 + (\delta\hat{p}^{s+} + \delta\hat{p}^{f-}) \\ &\times(1 + M_s(\theta^{s+})(\sin\psi\cos\phi^{s+}\sin\theta^{s+} + \cos\psi\cos\theta^{s+}))^2. \end{aligned}$$

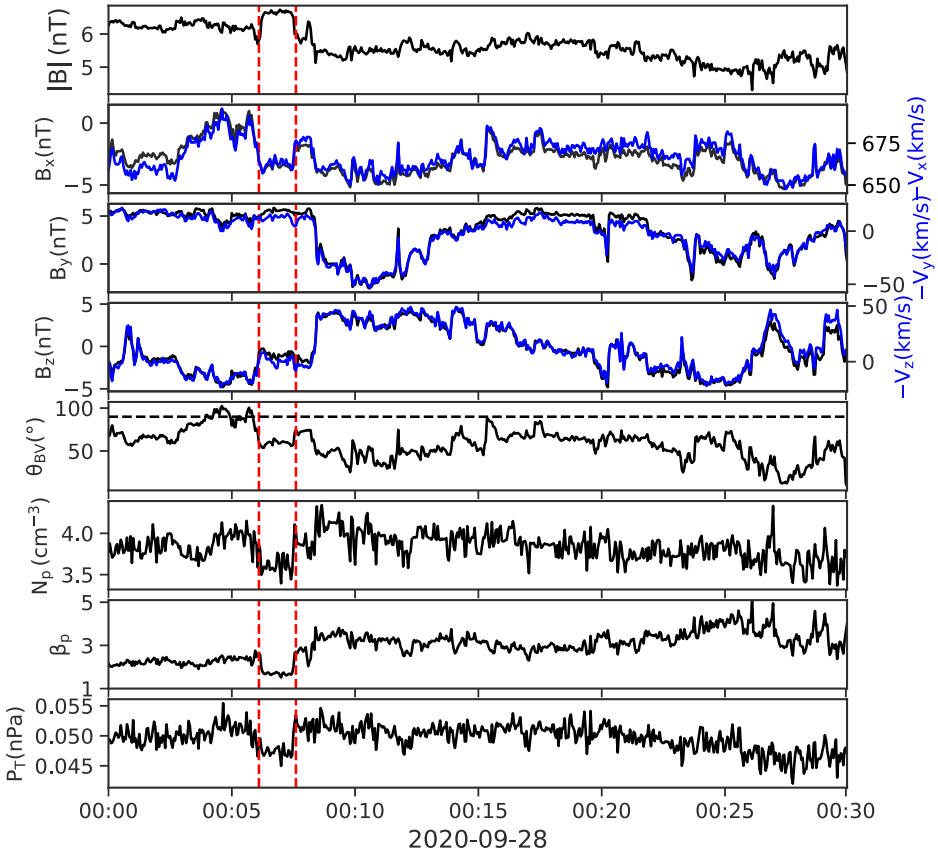


**Figure 2.** Overview of a fast solar wind 30 minute interval observed by the Wind spacecraft on 2020 September 28. From top to bottom, we plot the magnitude of the magnetic field $|B|$, the $x$, $y$, $z$ components of the magnetic field (left axis and black curves) and velocity field (right axis and blue curves) in the GSE coordinate system, the angle $\theta_{BV}$ between the magnetic and flow velocity vectors, the proton number density, the plasma beta $\beta_p$, and the total pressure $P_T$ that is the sum of the thermal and magnetic pressure. The red vertical dashed lines identify a possible large-amplitude nonlinear structure with an enhanced $|\boldsymbol{B}|$ and low density.

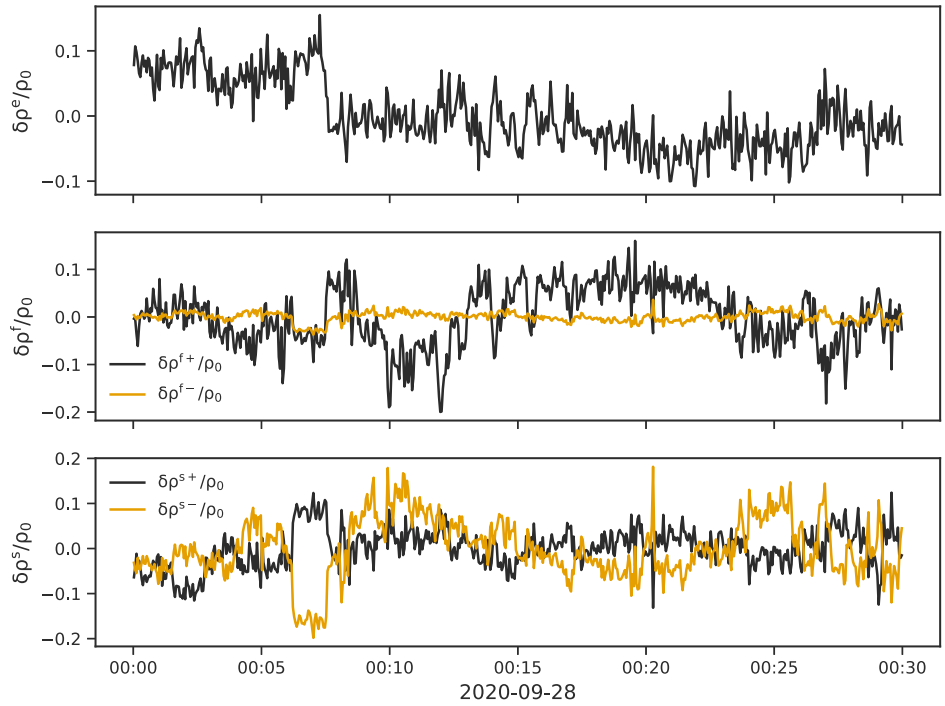


**Figure 3.** Mode decomposition over the 30 minute interval showing separately the contributions to the fluctuating density from (top to bottom) the entropy mode and the forward and backward fast and slow magnetosonic modes, $\delta\rho^e$, $\delta\rho^{f\pm}$, and $\delta\rho^{s\pm}$, respectively. All fluctuating quantities are normalized to the mean density as labeled.

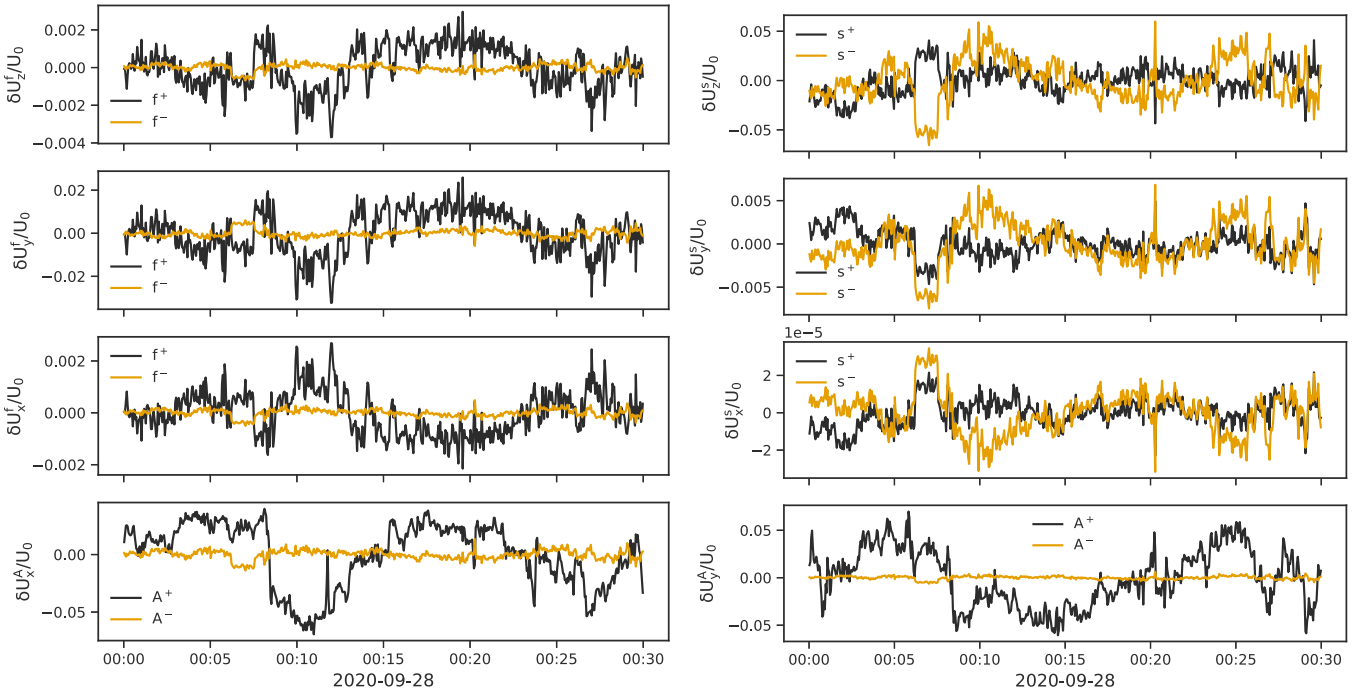


**Figure 4.** Mode decomposition in the mean-field coordinates showing separately the contributions to the fluctuating velocity from, arranged top to bottom in the left column, the forward and backward fast $\delta u^{f\pm}_{z,y,x}$ magnetosonic modes, respectively, and the forward and backward $x$-component of the Alfvén mode $\delta u_x^{A\pm}$, and in the right column, the forward and backward slow $\delta u^{s\pm}_{z,y,x}$ magnetosonic modes, respectively, and the forward and backward $y$-component of the Alfvén mode $\delta u_y^{A\pm}$. All fluctuating quantities are normalized to the mean speed as labeled.

This requires that the following condition relating $\theta^{f+}$ and $\theta^{s+}$ hold in order to ensure that we can express the rhs in terms of $\delta\hat{p}^{f+} + \delta\hat{p}^{f-} + \delta\hat{p}^{s+} + \delta\hat{p}^{s-}$:

$$(1 + M_f(\theta^{f+})(\sin\psi\cos\phi^{f+}\sin\theta^{f+} + \cos\psi\cos\theta^{f+}))^2$$
$$= (1 + M_s(\theta^{s+})(\sin\psi\cos\phi^{s+}\sin\theta^{s+} + \cos\psi\cos\theta^{s+}))^2 . \tag{82}$$

From the fast and slow magnetosonic dispersion relations, we have $\omega'_{f+} = \omega'_m = V_f(\theta^{f+})k^{f+}$ and $\omega'_{s+} = \omega'_m = V_s(\theta^{s+})k^{s+}$, which yields $k^{f+}/k^{s+} = V_s(\theta^{s+})/V_f(\theta^{f+})$. For the relation $\boldsymbol{U}_0\cdot\boldsymbol{k}^{s+} = \boldsymbol{U}_0\cdot\boldsymbol{k}^{f+}$ to hold, we require $k_x^{f+} = k_x^{s+}$ and $k_z^{f+} = k_z^{s+}$. The same is true for the $f$- and $s$-modes. Hence, the forward and backward slow and fast magnetosonic modes are related according to

$$\begin{aligned} k_x^{s\pm} &= k_x^{f\pm} \\ k_z^{s\pm} &= k_z^{f\pm} \end{aligned} \quad \text{and } k^{s\pm} = \frac{V_f(\theta^{f\pm})}{V_s(\theta^{s\pm})}k^{f\pm}; \tag{83}$$

$$\text{or } \frac{\cos\theta^{s\pm}}{V_s(\theta^{s\pm})} = \frac{\cos\theta^{f\pm}}{V_f(\theta^{f\pm})};\ \frac{\cos\phi^{s\pm}\sin\theta^{s\pm}}{V_s(\theta^{s\pm})} = \frac{\cos\phi^{f\pm}\sin\theta^{f\pm}}{V_f(\theta^{f\pm})}. \tag{84}$$

On substituting (84) into the expression on the rhs of (82), it is easily shown that it reduces exactly to the left-hand side (lhs) of (82), thereby establishing the equality. Hence, the $n = 1$ pressure Equation (76) becomes

$$\delta\hat{p}_m\left(1 + \frac{\boldsymbol{U}_0\cdot\boldsymbol{k}_m}{\omega'_m}\right)^2 = (\delta\hat{p}^{f+} + \delta\hat{p}^{f-} + \delta\hat{p}^{s+} + \delta\hat{p}^{fs})$$
$$\times (1 + M_f(\theta^{f+})(\sin\psi\cos\phi^{f+}\sin\theta^{f+} + \cos\psi\cos\theta^{f+}))^2 . \tag{85}$$

Because $\delta\hat{p}_m = \delta\hat{p}^{f+} + \delta\hat{p}^{f-} + \delta\hat{p}^{s+} + \delta\hat{p}^{s-}$ must hold always, expression (85) relates $\theta^{f+}$ and $\phi^{f+}$ to the observed Doppler-shifted frequency and phase values $\omega'_m$ and $\boldsymbol{k}_m$ via

$$\left(1 + \frac{U_0k_{mx}}{\omega'_m}\sin\psi + \frac{U_0k_{mz}}{\omega'_m}\cos\psi\right)^2 = (1 + M_f(\theta^{f+})$$
$$\times \sin\psi\cos\phi^{f+}\sin\theta^{f+} + M_f(\theta^{f+})\cos\psi\cos\theta^{f+})^2 . \tag{86}$$

Because (86) holds for all values of $\psi$, we have

$$\frac{U_0k_{mx}}{\omega'_m} = M_f(\theta^{f+})\cos\phi^{f+}\sin\theta^{f+}; \tag{87}$$

$$\frac{U_0k_{mz}}{\omega'_m} = M_f(\theta^{f+})\cos\theta^{f+}. \tag{88}$$

Because $V_f(\theta^{f+}) = \omega'_m/k_{mz}\cos\theta^{f+}$, using (20) yields

$$\cos^2\theta^{f+} = \frac{1}{M_0^2M_{A0}^2}\frac{(M_0^2 + M_{A0}^2)(\omega'_m/U_0k_{mz})^2 - 1}{(\omega'_m/U_0k_{mz})^4}; \tag{89}$$

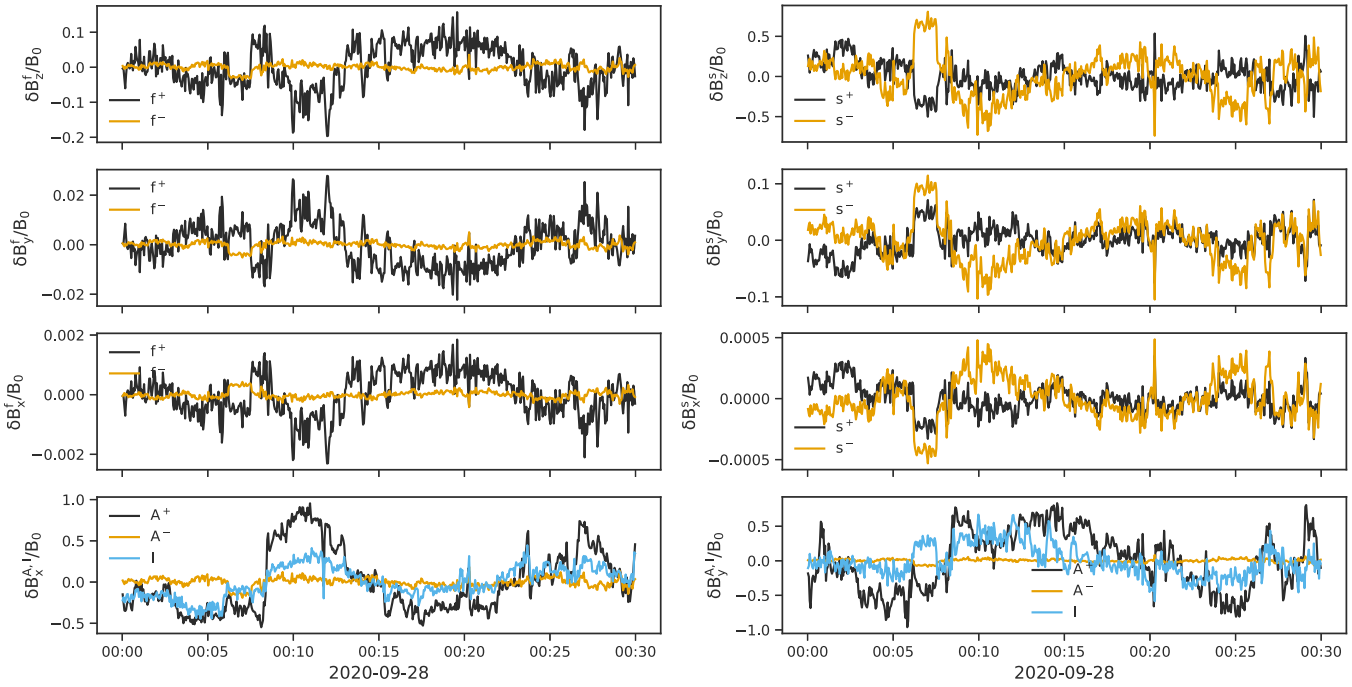


**Figure 5.** Mode decomposition in the mean-field coordinates showing separately the contributions to the fluctuating magnetic field from, arranged top to bottom in the left column, the forward and backward fast $\delta B^{f\pm}_{z,y,x}$ magnetosonic modes, respectively, and the forward and backward $x$-component of the Alfvén mode $\delta B^{A\pm}_{x}$ and the advected magnetic island $\delta B^{i}_{x}$ (blue curve), and in the right column, the forward and backward slow $\delta B^{s\pm}_{z,y,x}$ magnetosonic modes, respectively, and the forward and backward $y$-component of the Alfvén mode $\delta B^{A\pm}_{y}$ and the advected magnetic island $\delta B^{i}_{y}$ (blue). All fluctuating quantities are normalized to the mean magnetic field strength as labeled.

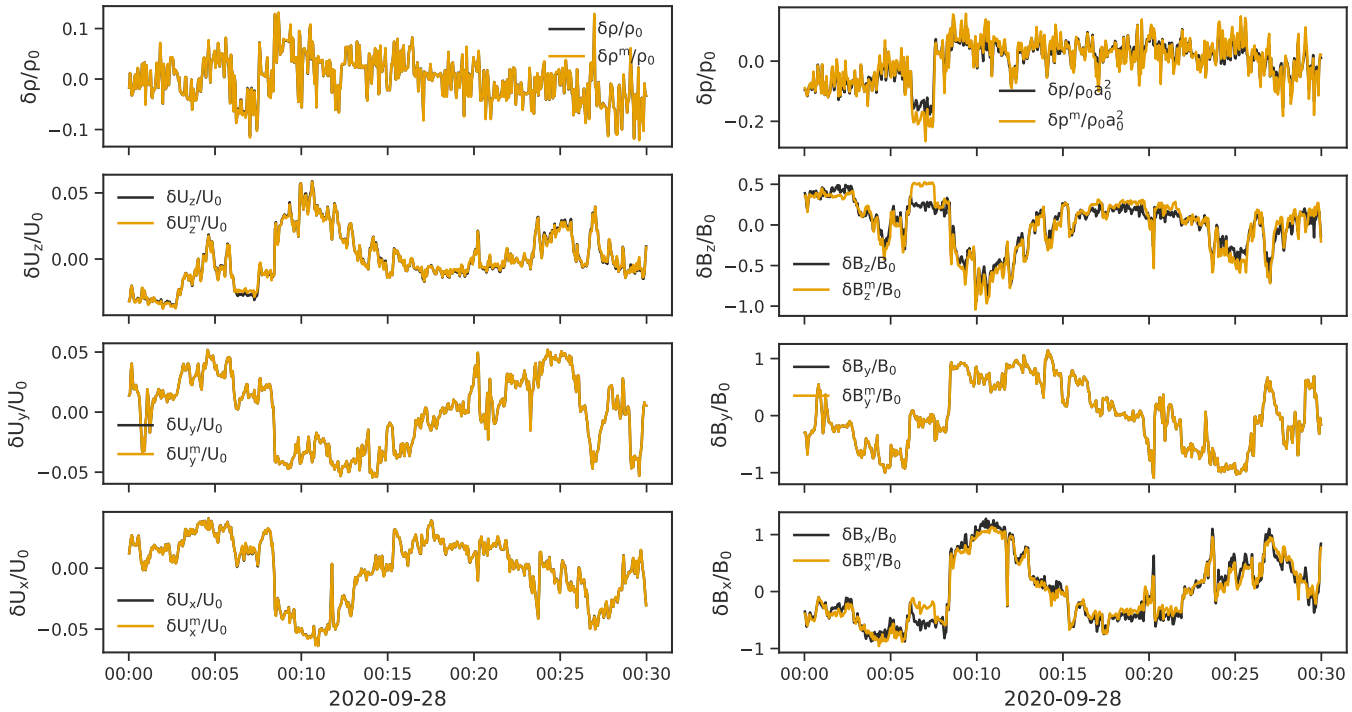


**Figure 6.** The black curves denote the reconstruction of the normalized (left column, top to bottom) total density $\delta\rho$, and fluctuating velocity components $\delta u_{z,y,x}$ respectively, from the summed mode decomposition, over which are plotted (orange curves) the corresponding measured values $\delta\rho^m$ and $\delta u^m_{z,y,x}$; (right column, top to bottom), total pressure $\delta p$, and fluctuating magnetic field components $\delta B_{z,y,x}$, respectively, over which are plotted (black curves) the corresponding normalized measured values $\delta p^m$ and $\delta B^m_{z,y,x}$. All fluctuating quantities are normalized to the appropriate mean value as labeled.

$$\cos\phi^{f+} = \frac{1}{(\omega'_m/U_0 k_{mx}) M_f(\theta^{f+})\sin\theta^{f+}}, \tag{90}$$

and we can therefore express the forward fast-mode magnetosonic angles $\theta^{f+}$, $\phi^{f+}$ in terms of the observed Doppler-shifted frequency $\omega'_m$ and wavenumber $\boldsymbol{k}_m$ together with the

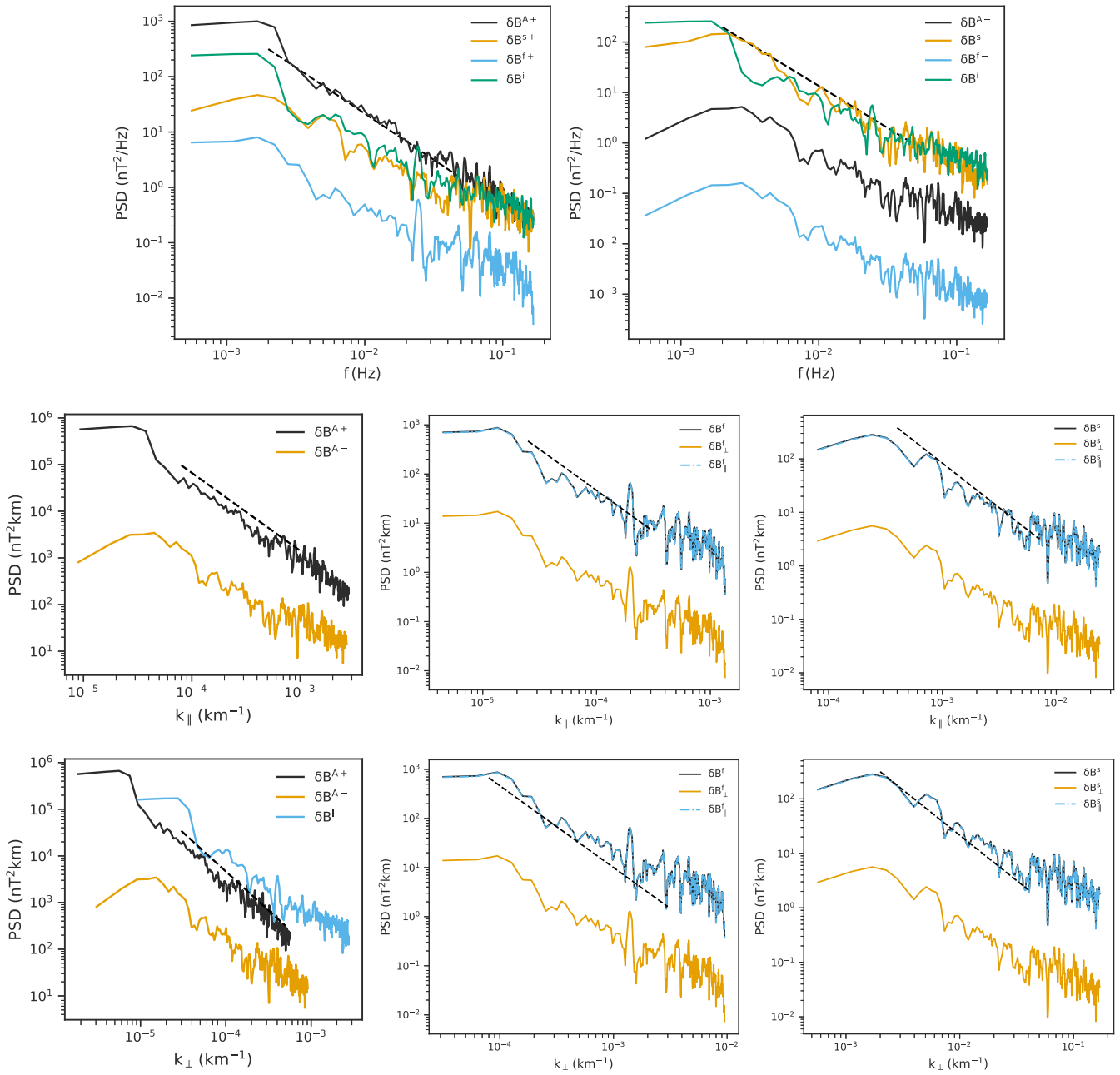


**Figure 7.** PSD plots of the fluctuating magnetic field. Top row: the frequency spectra of the magnetic island and forward Alfvén, fast, and slow magnetosonic modes (left); and the spectra of the magnetic island and backward Alfvén, fast, and slow magnetosonic modes (right). The dashed line in each plot is a reference $f^{-5/3}$ spectrum. Middle row: the parallel wavenumber spectra of the magnetic island and forward and backward Alfvén mode magnetic field fluctuations (left); the parallel wavenumber spectra of the parallel and perpendicular components, as well as the total magnetic field fluctuations of the fast magnetosonic modes (middle); and the parallel wavenumber spectra of the parallel and perpendicular components, as well as the total magnetic field fluctuations of the slow magnetosonic modes (right). Bottom row: the perpendicular wavenumber spectra of the magnetic island and forward and backward Alfvén mode magnetic field fluctuations (left); the perpendicular wavenumber spectra of the parallel and perpendicular components, as well as the total magnetic field fluctuations of the fast magnetosonic modes (middle); and the perpendicular wavenumber spectra of the parallel and perpendicular components, as well as the total magnetic field fluctuations of the slow magnetosonic modes (right).

measured mean plasma and magnetic field values $M_0$, $M_{A0}$, and $U_0$. By virtue of (79), this yields $\theta^{f-}$, $\phi^{f-}$ as well.

On using the first relation in Equation (84) and (20), we can express $\theta^{s+}$ in terms of $\theta^{f+}$, with

$$\cos^2\theta^{s+} = \frac{M_f^2(\theta^{f+})}{M_0^2 M_{A0}^2}\cos^2\theta^{f+}(M_0^2 + M_{A0}^2 - M_f^2(\theta^{f+})\cos^2\theta^{f+} \tag{91}$$

and from (84),

$$\cos\phi^{s+} = \frac{M_f(\theta^{f+})}{M_s(\theta^{s+})}\frac{\cos\phi^{f+}\sin\theta^{f+}}{\sin\theta^{s+}}. \tag{92}$$

Relations (81) then provide the corresponding values of $\theta^{s-}$, $\phi^{s-}$.

From the results above, the density Equation (77) can be expressed as

$$\delta\hat{\rho}_m\left(1+\frac{\boldsymbol{U}_0\cdot\boldsymbol{k}_m}{\omega'_m}\right)^2=\delta\hat{\rho}^e\left(\frac{\boldsymbol{U}_0\cdot\boldsymbol{k}^e}{\omega'_m}\right)^2+(\delta\hat{\rho}^{f+}+\delta\hat{\rho}^{f-}+\delta\hat{\rho}^{s+}+\delta\hat{\rho}^{s-})$$
$$\times(1+M_f(\theta^{f+})(\sin\psi\cos\phi^{f+}\sin\theta^{f+}+\cos\psi\cos\theta^{f+}))^2. \quad (93)$$

Because $\delta\hat{\rho}_m=\delta\rho^e+\delta\hat{\rho}^{f+}+\delta\hat{\rho}^{f-}+\delta\hat{\rho}^{s+}+\delta\hat{\rho}^{s-}$ must hold, we require that the equality

$$\frac{\boldsymbol{U}_0\cdot\boldsymbol{k}^e}{\omega'_m}=(1+M_f(\theta^{f+})(\sin\psi\cos\phi^{f+}\sin\theta^{f+}+\cos\psi\cos\theta^{f+})) \quad (94)$$

or

$$k_x^e\sin\psi+k_z^e\cos\psi=\frac{\omega'_m}{U_0}(1+M_f(\theta^{f+})(\sin\psi\cos\phi^{f+}\sin\theta^{f+}+\cos\psi\cos\theta^{f+}))$$

hold for all $\psi$. On solving for $k_x^e$ and $k_z^e$, we obtain

$$k_x^e=\frac{\omega'_m}{U_0}(\sin\psi+M_f(\theta^{f+})\cos\phi^{f+}\sin\theta^{f+}); \quad (95)$$

$$k_z^e=\frac{\omega'_m}{U_0}(\cos\psi+M_f(\theta^{f+})\cos\theta^{f+}). \quad (96)$$

Hence, because the entropy mode is simply advected with only $\delta\rho^e$ nonzero, and $k_y^e=0$, from Equations (95) and (96), we have

$$\tan\theta^e=\frac{k_x^e}{k_z^e}=\frac{\sin\psi+M_f(\theta^{f+})\cos\phi^{f+}\sin\theta^{f+}}{\cos\psi+M_f(\theta^{f+})\cos\theta^{f+}}; \quad (97)$$

$$k^e=(\cos\theta^e)^{-1}\frac{\omega'_m}{U_0}(\cos\psi+M_f(\theta^{f+})\cos\theta^{f+}). \quad (98)$$

To determine $\boldsymbol{k}^{A\pm}$ in terms of $\theta^{f+}$, $\phi^{f+}$, we use the $n=1$ expansion (67) for the velocity fluctuations. Let us consider first the $\delta u_x$ fluctuations. The dispersion relation is given by $\omega'_{A\pm}=\pm V_{A0}k_z^{A\pm}$. As above, in the $\delta\hat{\boldsymbol{u}}$ $n=1$ expansion (67), we require that

$$\boldsymbol{U}_0\cdot\boldsymbol{k}^{A+}+V_{A0}k_z^{A+}=\boldsymbol{U}_0\cdot\boldsymbol{k}^{A-}-V_{A0}k_z^{A-}$$
$$\Leftrightarrow M_{A0}(k_x^{A+}\sin\psi+k_z^{A+}\cos\psi)+k_z^{A+}$$
$$=M_{A0}(k_x^{A-}\sin\psi+k_z^{A-}\cos\psi)-k_z^{A-}.$$

This relation holds if $k_x^{A+}=k_x^{A-}$ and $k_z^{A+}(M_{A0}\cos\psi+1)=k_z^{A-}(M_{A0}\cos\psi-1)$, i.e., if the relations

$$k_z^{A-}=k_z^{A+}\frac{M_{A0}\cos\psi+1}{M_{A0}\cos\psi-1}; \quad (99)$$

$$k_x^{A+}=k_x^{A-} \quad (100)$$

hold. Obviously, Alfvén waves can have a net propagation direction with the flow when $M_{A0}>1$, depending on the obliquity of the flow. To simplify the $n=1$ expansion (67), we require that

$$\omega'_{A+}+\boldsymbol{U}_0\cdot\boldsymbol{k}^{A+}=\omega'_m(1+M_f(\theta^{f+})$$
$$\times(\sin\psi\cos\phi^{f+}\sin\theta^{f+}+\cos\psi\cos\theta^{f+})) \quad (101)$$

hold. It can then be shown that expression (101) is true provided

$$k_x^{A+}=\frac{\omega'_m}{U_0}(\sin\psi+M_f(\theta^{f+})\cos\phi^{f+}\sin\theta^{f+}); \quad (102)$$

$$k_z^{A+}=\frac{\omega'_m}{V_{A0}}\frac{\cos\psi(\cos\psi+M_f(\theta^{f+})\cos\theta^{f+})}{M_{A0}\cos\psi+1}. \quad (103)$$

Expressions (99) and (100) give the corresponding results for $\omega'_{A-}+\boldsymbol{U}_0\cdot\boldsymbol{k}^{A-}$. Hence, use of the eigenrelations (28) and the angle relations (102), (103), (99), and (100) allows us to express

$$\frac{\delta\hat{u}_x^{A\pm}}{U_0}(\omega'_{A\pm}+\boldsymbol{U}_0\cdot\boldsymbol{k}^{A\pm})^2=-\frac{\delta\hat{u}^{A\pm}}{U_0}\sin\phi^{A\pm}\times(\omega'_m)^2$$
$$(1+M_f(\theta^{f+})\sin\psi\cos\phi^{f+}\sin\theta^{f+}+M_f(\theta^{f+})\cos\psi\cos\theta^{f+})^2. \quad (104)$$

Similarly,

$$\frac{\delta\hat{u}_x^{f\pm}}{U_0}(\pm\omega'_m+\boldsymbol{U}_0\cdot\boldsymbol{k}^{f\pm})^2=\frac{\delta\hat{p}^{f\pm}}{\rho_0a_0^2}(\omega'_m)^2\frac{1}{M_f(\theta^{f+})}$$
$$\times\frac{M_{A0}^2\cos\phi^{f+}\sin\theta^{f+}}{M_{A0}^2-M_f^2(\theta^{f+})\cos^2\theta^{f+}}(1+M_f(\theta^{f+})$$
$$\times\sin\psi\cos\phi^{f+}\sin\theta^{f+}+M_f(\theta^{f+})\cos\psi\cos\theta^{f+})^2. \quad (105)$$

A very similar result can be derived for the forward and backward slow-mode fluctuations. The $n=1$ expansion of (67) provides the following equation for $\phi^{A\pm}$, the solution of which is coupled to the amplitude matrix (74):

$$\frac{\delta\hat{u}^{A+}}{U_0}\sin\phi^{A+} + \frac{\delta\hat{u}^{A-}}{U_0}\sin\phi^{A-} = -\frac{\delta\hat{u}_{mx}}{U_0} + \frac{1}{M_f(\theta^{f+})} \times \left[\frac{\delta\hat{p}^{f+}}{\rho_0 a_0^2} + \frac{\delta\hat{p}^{f-}}{\rho_0 a_0^2} + \frac{M_f^2(\theta^{f+})}{M_s^2(\theta^{s+})}\left(\frac{\delta\hat{p}^{s+}}{\rho_0 a_0^2} + \frac{\delta\hat{p}^{s-}}{\rho_0 a_0^2}\right)\right] \times \frac{M_{A0}^2\cos\phi^{f+}\sin\theta^{f+}}{M_{A0}^2 - M_f^2(\theta^{f+})\cos^2\theta^{f+}}. \tag{106}$$

The same approach applied to the $\delta u_y$ fluctuations gives the second coupled wavenumber boundary condition equation as

$$\frac{\delta\hat{u}^{A+}}{U_0}\cos\phi^{A+} + \frac{\delta\hat{u}^{A-}}{U_0}\cos\phi^{A-} = \frac{\delta\hat{u}_{my}}{U_0} - \left(\frac{\delta\hat{p}^{f+}}{\rho_0 a_0^2} + \frac{\delta\hat{p}^{f-}}{\rho_0 a_0^2}\right)\frac{1}{M_f(\theta^{f+})}\frac{M_{A0}^2\sin\phi^{f+}\sin\theta^{f+}}{M_{A0}^2 - M_f^2(\theta^{f+})\cos^2\theta^{f+}} - \left(\frac{\delta\hat{p}^{s+}}{\rho_0 a_0^2} + \frac{\delta\hat{p}^{s-}}{\rho_0 a_0^2}\right)\frac{1}{M_s(\theta^{s+})}\frac{M_{A0}^2\sin\phi^{s+}\sin\theta^{s+}}{M_{A0}^2 - M_s^2(\theta^{s+})\cos^2\theta^{s+}}. \tag{107}$$

Finally, for $\theta^{A\pm}$, we can use $k_x^{A\pm}/k_z^{A\pm} = \cos\phi^{A\pm}\tan\theta^{A\pm}$. Hence, use of (102) and (103) yields

$$\tan\theta^{A\pm} = (\cos\phi^{A\pm})^{-1}\frac{M_{A0}\cos\psi \pm 1}{M_{A0}\cos\psi} \times \frac{\sin\psi + M_f(\theta^{f+})\cos\phi^{f+}\sin\theta^{f+}}{\cos\psi + M_f(\theta^{f+})\cos\theta^{f+}}. \tag{108}$$

Finally, consider the magnetic island phase. Because 2D magnetic islands lie in the plane orthogonal to $\boldsymbol{B}_0$, $\theta^i = \pi/2$, $\omega_i' = 0 = \omega - U_0\sin\psi k^i\cos\phi^i$, and $\omega_m' = \pm V_f(\theta^{f+})k^{f+}$, it follows from Equations (68) that $k_x^I$ must satisfy

$$k_x^i = \frac{\omega_m'}{U_0\sin\psi}(1 + M_f(\theta^{f+})\sin\psi\cos\phi^{f+}\sin\theta^{f+} + M_f(\theta^{f+})\cos\psi\cos\theta^{f+}). \tag{109}$$

By using (109), as well as the $y$-component of (68) in the $n = 1$ expansion, it can be shown that the equation that determines $\phi^i$ is given by

$$\frac{\delta\hat{B}^i}{B_0}\cos\phi^i = \frac{\delta\hat{B}_{my}}{B_0} + \left(\frac{\delta\hat{p}^{f+}}{\rho_0 a_0^2} + \frac{\delta\hat{p}^{f-}}{\rho_0 a_0^2}\right)\frac{M_{A0}^2\sin\phi^{f+}\sin\theta^{f+}\cos\theta^{f+}}{M_{A0}^2 - M_f^2(\theta^{f+})\cos^2\theta^{f+}} + \left(\frac{\delta\hat{p}^{s+}}{\rho_0 a_0^2} + \frac{\delta\hat{p}^{s-}}{\rho_0 a_0^2}\right)\frac{M_{A0}^2\sin\phi^{s+}\sin\theta^{s+}\cos\theta^{s+}}{M_{A0}^2 - M_s^2(\theta^{s+})\cos^2\theta^{s+}} + M_{A0}\left(\frac{\delta\hat{u}^{A+}}{U_0}\cos\phi^{A+} + \frac{\delta\hat{u}^{A-}}{U_0}\cos\phi^{A-}\right). \tag{110}$$

It should be noted that, because we used the boundary condition (58) in the amplitude matrix, we had to use (59) in deriving (110).

The measured fluctuation that is observed at a particular Doppler-shifted frequency $\omega_m'$ must be supplemented by the corresponding wavenumber $\boldsymbol{k}_m$. Unfortunately, $\boldsymbol{k}_m$ cannot be measured by a single spacecraft, and we need to utilize one of several methods available to estimate a value. These methods can include the minimum variance analysis technique (Sonnerup & Scheible 1998; Zhao et al. 2021c) and singular value decomposition (Santolik et al. 2003; Zhao et al. 2021b), both based on utilizing the divergence-free condition $\boldsymbol{k}\cdot\delta\boldsymbol{B} = 0$. Another method used for discontinuities is a cross-product method based on the upstream $\boldsymbol{B}_u$ and downstream magnetic field $\boldsymbol{B}_d$ vectors across a transition (Burlaga 1969; Burlaga & Ness 1969; Knetter et al. 2004). For our present purposes, we will assume that an inferred $\boldsymbol{k}_m$ exists. We discuss this point further below.

To solve the linear system (74) for the eight mode amplitudes, we need the corresponding phase information $\boldsymbol{k} = \boldsymbol{k}(k, \theta, \phi)$ for each mode based on the measured $\omega_m'$ and (inferred) $\boldsymbol{k}_m$. We showed above that $\theta^{f+}$, $\phi^{f+}$ can be derived from $\omega_m'$ and $\boldsymbol{k}_m$, from which $\theta^{f-}$, $\phi^{f-}$ and the remaining $\theta^e$, $\phi^e$, $\theta^i$, $\phi^i$, $\theta^{s\pm}$, and $\phi^{s\pm}$ can be determined. The supplementary Equations (106), (107), and (110) must be solved for $\phi^{A\pm}$ and $\phi^i$ together with the simultaneous inversion of the amplitude matrix. We have found that using mean values for the $\phi^{A\pm}$ yields a mode stable inversion. In practice, we developed two independent codes to solve the coupled system of equations, the one using an iterative method for (106), (107), and (110), and the other using a Newton–Raphson method that solves the linear system (74) simultaneously with (106), (107), and (110). Both methods give essentially identical results.

An attractive and useful consequence of evaluating the wavenumbers of each of the eight modes is that one can express the modal spectra interchangeably in terms of either Doppler-shifted frequency or wavenumber, i.e., we do not have to invoke Taylor's hypothesis when converting frequency to wavenumber. This is of course a consequence of expressing an observed fluctuation in terms of a superposition of small-amplitude linear modes, which may not be a good approximation for all situations. Nonetheless, this approach provides valuable insight into the nature of fluctuations in the solar wind. For convenience, we list the conversions that map frequency to wavenumber.

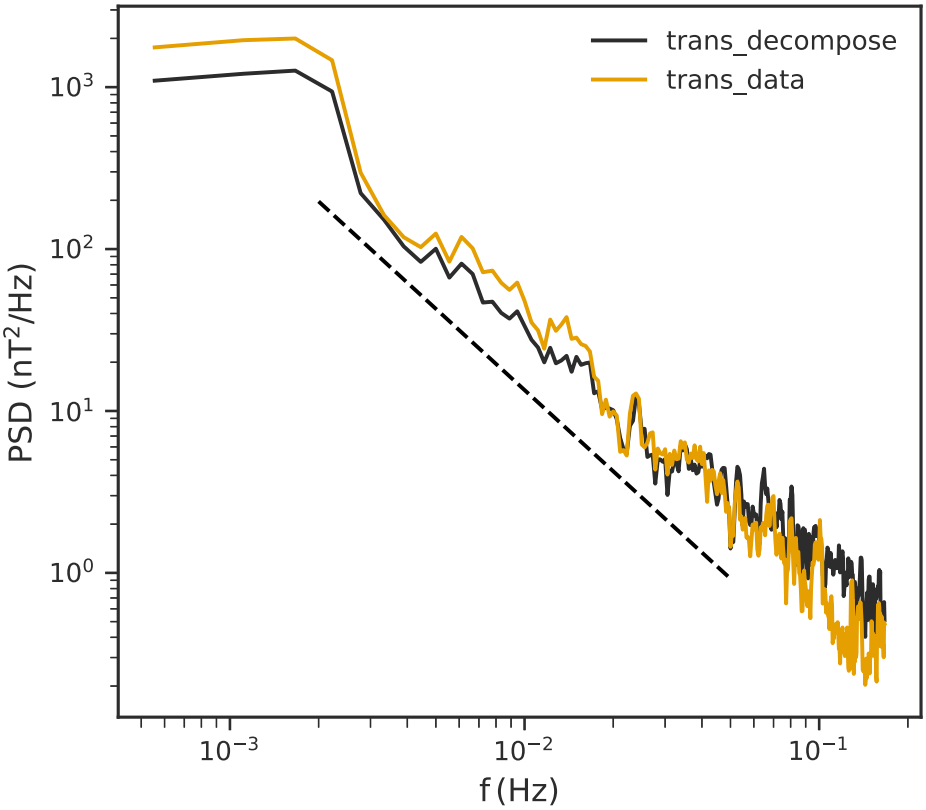


**Figure 8.** The orange curve shows the fully nonlinear FFT-derived PSD for the transverse magnetic field fluctuations drawn from the original data in the 30 minute interval shown in Figure 2. The black curve is a reconstructed spectrum for the transverse fluctuations derived by summing the transverse contributions from each mode that admits transverse fluctuations, i.e., the separate transverse contributions from each of the Alfvén, magnetic island, forward fast, backward fast, forward slow, and backward slow modes. The dashed line represents $f^{-5/3}$.

Entropy modes: for each $\omega'_m$, we map to the entropy wavenumber $\boldsymbol{k}^e$ using Equations (95), (96), $k_y^e = 0$, and (97), (98).

Magnetic islands: for each $\omega'_m$, $k_x^i$ is given by (109), $\phi^i$ by (110), and $k^i$ is determined from $k_x^i = k^i \cos\phi^i$ (because $\theta^i = \pi/2$).

Fast/slow magnetosonic modes: for each of these four cases, we have $k^{fs\pm} = \omega'_m / V_{fs}(\theta^{fs\pm})$ and hence $k_\perp^{fs\pm} = k^{fs\pm} \sin\theta^{fs\pm}$ and $k_\parallel^{fs\pm} = k^{fs\pm} \cos\theta^{fs\pm}$.

Alfvén modes: For each $\omega'_m$, Equations (106) and (107) provide $\phi^{A\pm}$ and (108) gives $\theta^{A\pm}$. Because $k_x^{A+} = k_x^{A-}$, we have

$$k^{A\pm} = (\cos\phi^{A\pm} \sin\theta^{A\pm})^{-1} \frac{\omega'_m}{U_0} (\sin\psi + M_f(\theta^{f+}) \cos\phi^{f+} \sin\theta^{f+}), \tag{111}$$

giving $k_\perp^{A\pm} = k^{A\pm} \sin\theta^{A\pm}$ and $k_\parallel^{A\pm} = k^{A\pm} \cos\theta^{A\pm}$.

The detailed algorithm to solve the linear mode-decomposition problem is presented in Appendix C.

## 4. Analysis of Solar Wind Data

To illustrate the practical application of the mode-decomposition method presented above, we consider several examples. Besides illustrating the method, several new interesting and important results about the composition of fluctuations in the solar wind and their modal spectra emerge in this first study. Specifically, the identification of entropy fluctuations is new, as is the separation of Alfvénic and small-scale magnetic island/flux rope modes and their respective spectra. Similarly, the various modal spectra are new results.

Several examples are considered, allowing us to explore briefly the application of the mode-decomposition method to flows with (i) an oblique orientation of the mean flow velocity and magnetic field vectors, (ii) a highly aligned flow configuration, and (iii) a highly oblique flow configuration.

In applying the mode-decomposition analysis, we consider a plasma parcel of limited duration (as long as 30 minutes and as short as 5 minutes) that can be considered as quiet (i.e., no shock waves, large-scale magnetic flux ropes, or crossings of the heliospheric current sheet). A set of mean plasma and magnetic field variables is constructed from the plasma parcel from which we obtain the fluctuating plasma and magnetic field components. The fluctuating variables are rotated into a coordinate system such that the mean flow velocity lies in the $(x, z)$-plane and the mean magnetic field $\boldsymbol{B}_0$ is aligned with the $z$-axis, as illustrated in Figure 1. The plasma parcel is considered to be a superposition of all the possible MHD modes listed in Section 2, provided that these can be measured by the spacecraft, propagating or advecting at various angles to the mean magnetic field vector. The plasma parcel is of suitably long duration that it is reasonable to assume that it is advected in the background supersonic and super-Alfvénic solar wind

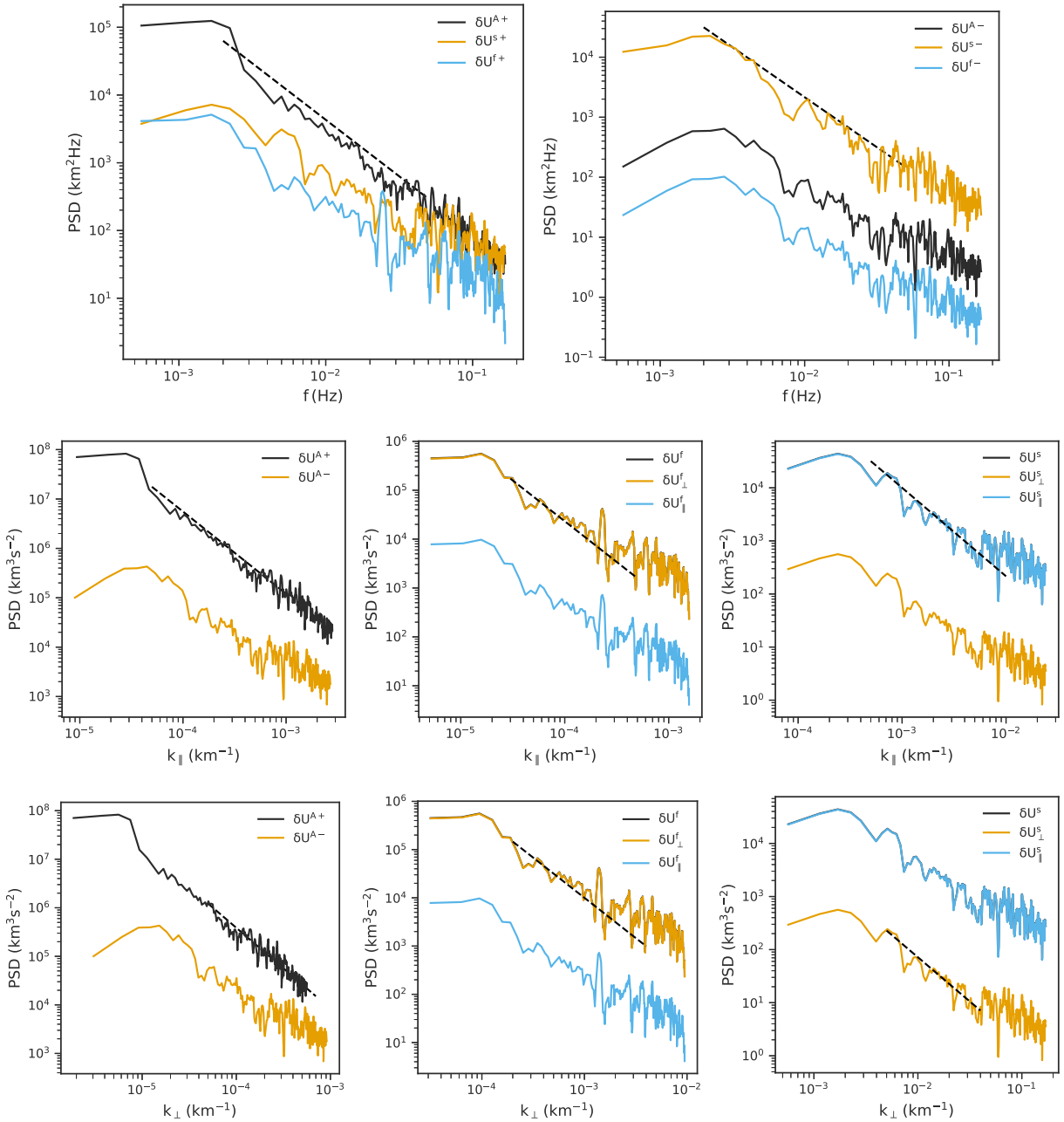


**Figure 9.** PSD plots of the fluctuating velocity field showing (left) frequency spectra of the forward Alfvén, fast, and slow magnetosonic modes (left); and spectra of the backward Alfvén, fast, and slow magnetosonic modes (right). The dashed line in each plot is a reference $f^{-5/3}$ spectrum. Middle row: the parallel wavenumber spectra of the forward and backward Alfvén mode magnetic field fluctuations (left); the parallel wavenumber spectra of the parallel and perpendicular components, as well as the total velocity field fluctuations of the fast magnetosonic modes (middle); and the parallel wavenumber spectra of the parallel and perpendicular components, as well as the total velocity field fluctuations of the slow magnetosonic modes (right). Bottom row: the perpendicular wavenumber spectra of the forward and backward Alfvén mode magnetic field fluctuations (left); the perpendicular wavenumber spectra of the parallel and perpendicular components, as well as the total velocity field fluctuations of the fast magnetosonic modes (middle); and the perpendicular wavenumber spectra of the parallel and perpendicular components, as well as the total velocity field fluctuations of the slow magnetosonic modes (right).

flow. This assumption makes the Minimum Variance Analysis (MVA) method particularly attractive in determining the direction of $\boldsymbol{k}_m$. The MVA approach (Sonnerup & Scheible 1998; Zhao et al. 2021c) yields the angles $\theta_m$ and $\phi_m$ of $\boldsymbol{k}_m$ for the plasma parcel. By invoking Taylor's hypothesis for the plasma parcel in which the fluctuations are embedded, we obtain the magnitude of $\boldsymbol{k}_m$, i.e., $k_m = \omega'_m/U_0$. This is valid for a supersonic, super-Alfvénic solar wind flow; if the flow is sub-Alfvénic, for example, a modified form of Taylor's hypothesis is necessary (e.g., Zank et al. 2022). As shown in Appendix C, the measured frequency $\omega'_m$ and the components of $\boldsymbol{k}_m$ always appear as a ratio, meaning that the amplitude of $\boldsymbol{k}_m$ and $\omega'_m$ cancel. This makes the MVA approach especially tractable. Investigation of other approaches to the determination of $\boldsymbol{k}_m$ should be explored, but the results presented here all utilize an MVA for each plasma parcel of interest.

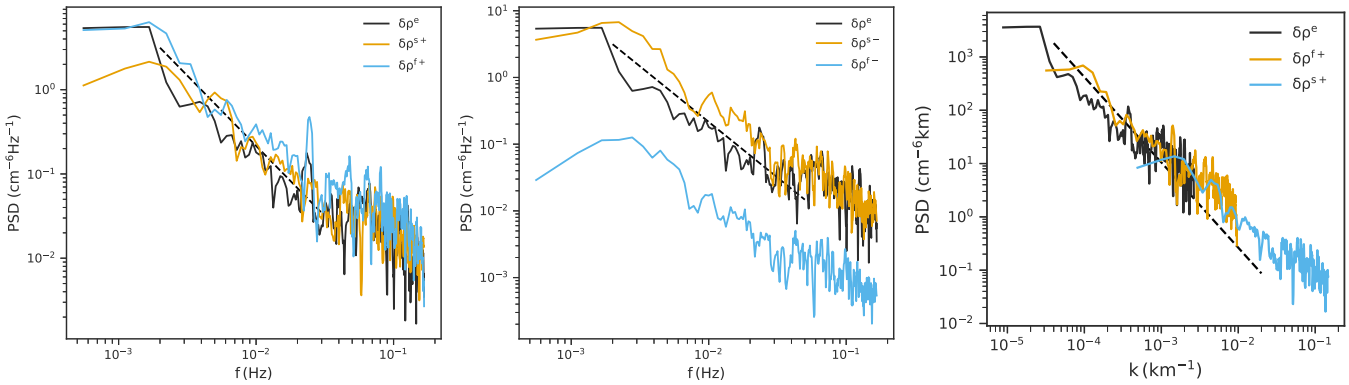


**Figure 10.** PSD plots for the fluctuating density showing the frequency spectra of the entropy and the forward fast and slow magnetosonic modes (left), the frequency spectra of the entropy and the backward fast and slow magnetosonic modes (middle), and the wavenumber spectra of the entropy and forward fast and slow magnetosonic modes (right). The dashed lines in the left and middle plots are reference $f^{-5/3}$ curves, and that in the right plot is a $k^{-5/3}$ curve.

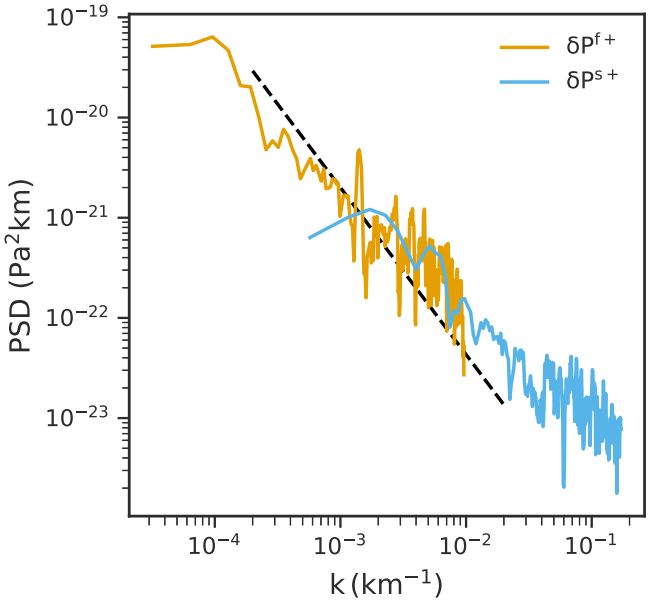


**Figure 11.** PSD plots for the fluctuating pressure showing wavenumber spectra of the forward fast and slow magnetosonic modes.

### *4.1. Oblique Flow Interval*

Shown in Figure 2 is a 30 minute interval from a fast solar wind stream observed by the Wind spacecraft on 2020 September 28. The $\boldsymbol{k}_m$ vector was calculated at 0.01 Hz (within the inertial range at 1 au) and the fluctuations were calculated by subtracting the average value from the observed value. From top to bottom, Figure 2 shows the magnetic field magnitude, the three components of the magnetic and velocity fields in GSE coordinates, the angle $\theta_{BV}$ between the magnetic and velocity vectors, the proton number density, and finally the proton plasma beta $\beta_p$. The background flow $U_0$ in the mean-field coordinates (i.e., the frame shown in Figure 1) is [497, 0, 446] km s$^{-1}$, and $B_0$ in the mean-field coordinates is [0, 0, 4.34] nT. Several points are of interest: this is a very typical fast solar wind interval that would be described as Alfvénic, as illustrated by the magnetic and velocity field component correlations, possessing no particular features such as shocks or strong current sheet crossings; and the mean velocity and magnetic field vectors are largely intermediate to both $\theta_{BV} = 0°$ and 90°, making this a good example of an oblique flow with $\theta_{BV} \sim 60°$ for most of the 30 minute interval. However, there is a short period around 00:05 when the flow and magnetic field are perpendicular to one another, and shortly thereafter is a small interval of about a minute and a half duration (bounded by two vertical dashed lines) that is characterized by increased magnetic field strength and decreased proton density and plasma beta. The plasma beta $\beta_p$ is derived from the plasma pressure that is taken as twice the proton pressure. It is unclear what this structure is, as the increased magnetic field strength, reduced proton density, and plasma beta might suggest a coronal mass ejection flux rope-like structure, but a helicity method analysis (Zhao et al. 2020) failed to identify it as such, as there is little apparent rotation of the magnetic field components in the interval. The total pressure plot (the sum of the thermal and magnetic pressures) in the last panel of Figure 2 shows that the interval has a relatively constant but depressed total pressure relative to its surroundings. Based on its curious structure, we regard this interval as corresponding to a large-amplitude nonlinear structure with enhanced $|\boldsymbol{B}|$ and low density. In view of this characterization, the assumptions of small-amplitude fluctuations and linearity in this interval are unlikely to be met. Indeed, as we point out below, this short interval corresponds to a region for which a reconstruction of the data based on the $8 \times 8$ mode decomposition is not exact. There is a brief interval around 00:27 where $\theta_{BV} \sim 20°$. Finally, outside the vertical red lines, the plasma beta ranges from ∼2 to 3, or equivalently the proton plasma beta is ∼1–1.5 over most of the interval. If interpreted in terms of NI MHD, this places the interval in the $\beta_p \sim O(1)$ regime for which the turbulence might be expected to correspond to a superposition of 2D + slab fluctuations (Zank & Matthaeus 1992, 1993; Zank et al. 2017, 2020). Within the scope of NI MHD, larger values of $\beta_p$ would correspond at leading order to fully 3D incompressible MHD and a higher-order compressible correction (Zank & Matthaeus 1992, 1993).

On applying the $8 \times 8$ mode-decomposition algorithm outlined in Appendix C, we plot in Figure 3 the contributions to the density due to (from top to bottom) the advected entropy modes $\delta\rho^e$ as well as the forward and backward fast $\delta\rho^{f\pm}$ and slow $\delta\rho^{s\pm}$ magnetosonic modes. This is the first identification of density fluctuations associated with entropy modes made in solar wind data. It is apparent that the amplitudes of the $\delta\rho^e$,

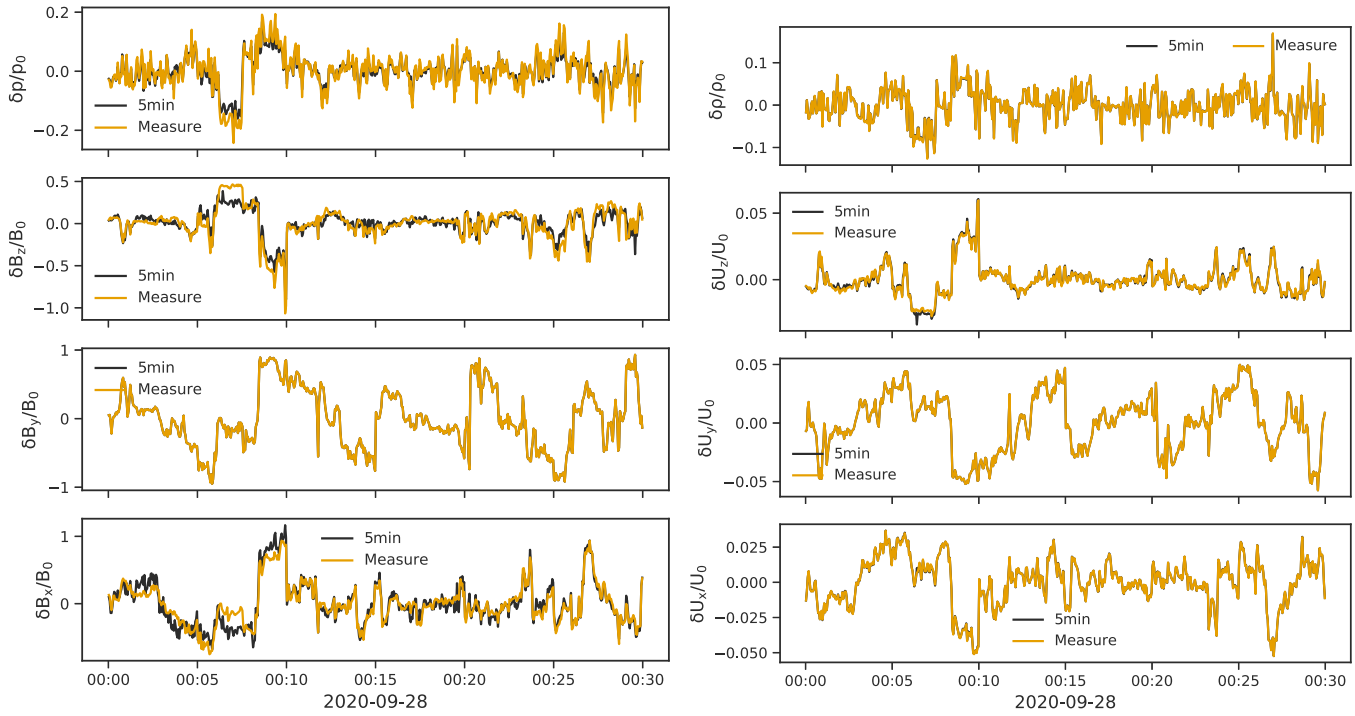


**Figure 12.** The orange curves denote the normalized measured data for the full 30 minute interval showing (left column, top to bottom) the normalized fluctuating total pressure $\delta p$ and the fluctuating magnetic field components $\delta B_{z,y,x}$, as well as (right column, top to bottom) the density $\delta\rho$ and the fluctuating velocity components $\delta u_{z,y,x}$, respectively, over which are plotted (black curves) the reconstructed values derived from the connected six 5 minute intervals. All fluctuating quantities are normalized to the appropriate mean value as labeled.

$\delta\rho^{f+}$, and $\delta\rho^{s\pm}$ are all comparable and that $\delta\rho^{f-}$ is a minor contributor. The density spectra are discussed below.

The contributions of the magnetosonic and Afvénic modes to the fluctuating velocity field are illustrated in Figure 4. Here and hereafter, we use the mean-field coordinates as defined in Figure 1. The top left and right panels show the compressible velocity fluctuations $\delta u_z^{fs\pm}/U_0$ for the forward and backward fast (left column) and slow (right) magnetosonic modes. The forward and backward slow compressible fluctuations are roughly anticorrelated and have comparable amplitudes. The slow-mode fluctuations are approximately 10–20 times larger in amplitude than the compressible forward fast magnetosonic modes, and the compressible backward fast mode makes little contribution. The left and right second and third panels from the top show the compressible contribution to the transverse velocity fluctuations $\delta u_{x,y}^{fs\pm}$. Although the $\delta u_y^{s\pm}$ and $\delta u_x^{s\pm}$ transverse velocity fluctuations are anticorrelated, the amplitudes of the $\delta u_x^{s\pm}$ fluctuations are about two orders of magnitude smaller than those of $\delta u_y^{s\pm}$. Similarly, the $\delta u_y^{f\pm}$ and $\delta u_x^{f\pm}$ transverse velocity fluctuations are anticorrelated and the amplitudes of the $\delta u_x^{f\pm}$ fluctuations are about an order of magnitude smaller than $\delta u_y^{f+}$. The backward fast modes have very small amplitudes. Finally, the bottom panels show the incompressible transverse velocity fluctuations contributed by the forward and backward Alfvén modes, $\delta u_x^{A\pm}$ (left) and $\delta u_y^{A\pm}$ (right). The contribution from the backward Alfvén mode is almost negligible compared to the forward Alfvén mode $\delta u_{x,y}^{A+}$, and these amplitudes are considerably larger than the corresponding compressible transverse velocity fluctuations.

The decomposition of the fluctuating magnetic field is illustrated in Figure 5, in the same format as Figure 4. The formatting and normalization expresses clearly the correlations and anticorrelations between the compressible and incompressible velocity and magnetic field fluctuations of the fast, slow, and Alfvénic modes. Also plotted in the bottom two panels are the incompressible transverse magnetic field fluctuations contributed by the magnetic islands (blue curves). The transverse magnetic field components are dominated by the incompressible forward Alfvén $\delta B_{x,y}^{A+}$ and magnetic island $\delta B_{x,y}^{i}$ components, although the contribution by the compressible $y$-component of the forward and backward slow mode is not insignificant.

Having performed the mode decomposition of the Wind interval, we can sum the modal contributions to the plasma density, velocity, pressure, and magnetic field to construct the total plasma density, velocity, pressure, and magnetic field. This can then be compared to the original data observed by Wind. As shown in Figure 6, the reconstructed data ($\delta\Psi$, black curves) replicate the measured data $\delta\Psi^m$ (orange curves) very well in general. The density, velocity components, and $\delta B_y$ reconstruction are essentially identical to the measured values. With the exception of one interval, identified by the vertical red dashed lines in Figure 2, the reconstructed pressure and $x$- and $z$-components of the magnetic field fluctuations closely track the measured data. The poor reconstruction of the 90 s of data between the vertical red lines would appear to be due to a larger-scale magnetic island embedded in the interval and therefore not appropriate to a small-amplitude mode representation. Excluding the large-scale structure, we conclude the modal decomposition accurately reproduces the measured data.

Thanks to the mode decomposition, we can examine the spectral properties of each of the modal components, both as functions of Doppler-shifted frequency and wavenumber using

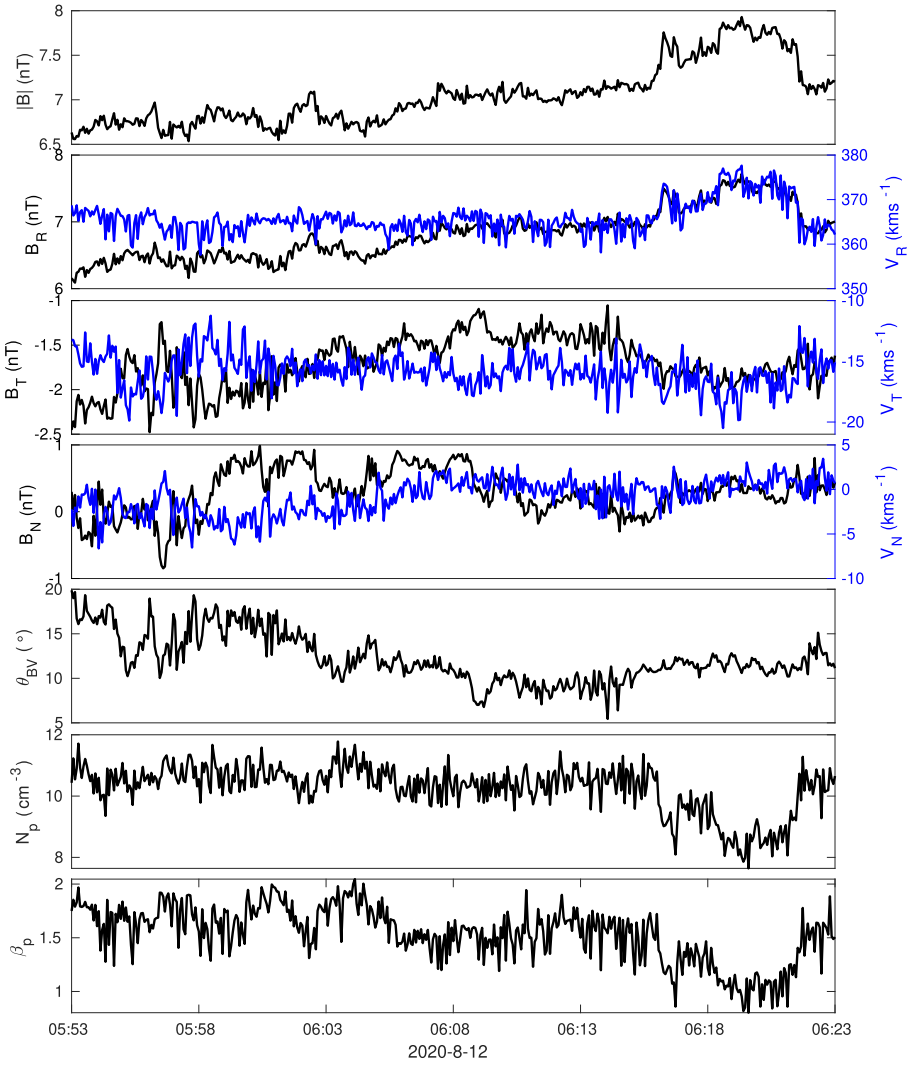


**Figure 13.** Overview of a 30 minute slow solar wind interval observed by the Solar Orbiter spacecraft on 2020 August 12. From top to bottom, we plot the magnitude of the magnetic field $|B|$, the components of the magnetic field (left axis and black curves) and velocity field (right axis and blue curves) in the *RTN* coordinate system, the angle $\theta_{BV}$ between the magnetic and flow velocity vectors, the proton number density, and the proton plasma beta $\beta_p$.

the results at the end of Section 3.4. The top two panels of Figure 7 plot the fluctuating magnetic field power spectral densities (PSDs) as a function of frequency for (left) the forward Alfvén, forward fast and slow magnetosonic, and the magnetic island modes, as well as (right) the corresponding backward and magnetic island modes. For the fast and slow magnetosonic modes, $\delta B^{fs\pm} = \sqrt{\delta B_{\parallel}^2 + \delta B_{\perp}^2}$ includes both the longitudinal and transverse compressible components, whereas $\delta B^{A\pm,i} = (\delta B_{\perp}^{A\pm,i2})^{1/2}$ for the Alfvénic and magnetic island modes is exclusively transverse and incompressible. Based on the top two panels, we would conclude that the forward Alfvén, magnetic island, and the forward and backward slow modes dominate the spectral energy density. All four spectra follow an $f^{-5/3}$ spectrum approximately for about 1.5 decades, after which the magnetic island and slow magnetosonic spectra appear to exhibit some flattening at the higher frequencies.

A notable feature of the mode decomposition is that we can transform the spectra from a frequency domain to a wavenumber domain via the transformations listed in Section 3.4. The middle panel plots the various modal PSDs as functions of parallel wavenumber $k_{\parallel}$, showing from left to right plots of the forward and backward Alfvén spectra; the PSDs for the fast magnetosonic mode total $\delta B^f$, longitudinal $\delta B_{\parallel}^f$, and transverse $\delta B_{\perp}^f$; and the PSDs for the slow magnetosonic mode total $\delta B^s$, longitudinal $\delta B_{\parallel}^s$, and transverse $\delta B_{\perp}^s$. The range of $k_{\parallel}$ is from about $10^{-5}$ (km$^{-1}$) to about $2.5 \times 10^{-3}$ (km$^{-1}$) for the Alfvén modes. The range is similar for the fast magnetosonic modes, but moves to higher wavenumbers for the slow mode (from $10^{-4}$ (km$^{-1}$) to about $2 \times 10^{-2}$ (km$^{-1}$)). Clearly, the forward Alfvén mode is the dominant component of the parallel wavenumber spectrum, and for both magnetosonic modes, the longitudinal PSD is dominant. The bottom row of panels plots the various modal PSDs as functions of perpendicular wavenumber $k_{\perp}$. The format follows that of the middle panel. The left bottom panel now includes the magnetic island PSD, showing that it in fact is the dominant contribution to the spectrum of incompressible transverse magnetic fluctuations, being larger than the forward Alfvénic fluctuations. As with the $k_{\parallel}$ PSDs of the middle panel, the incompressible transverse modes due to the magnetic island

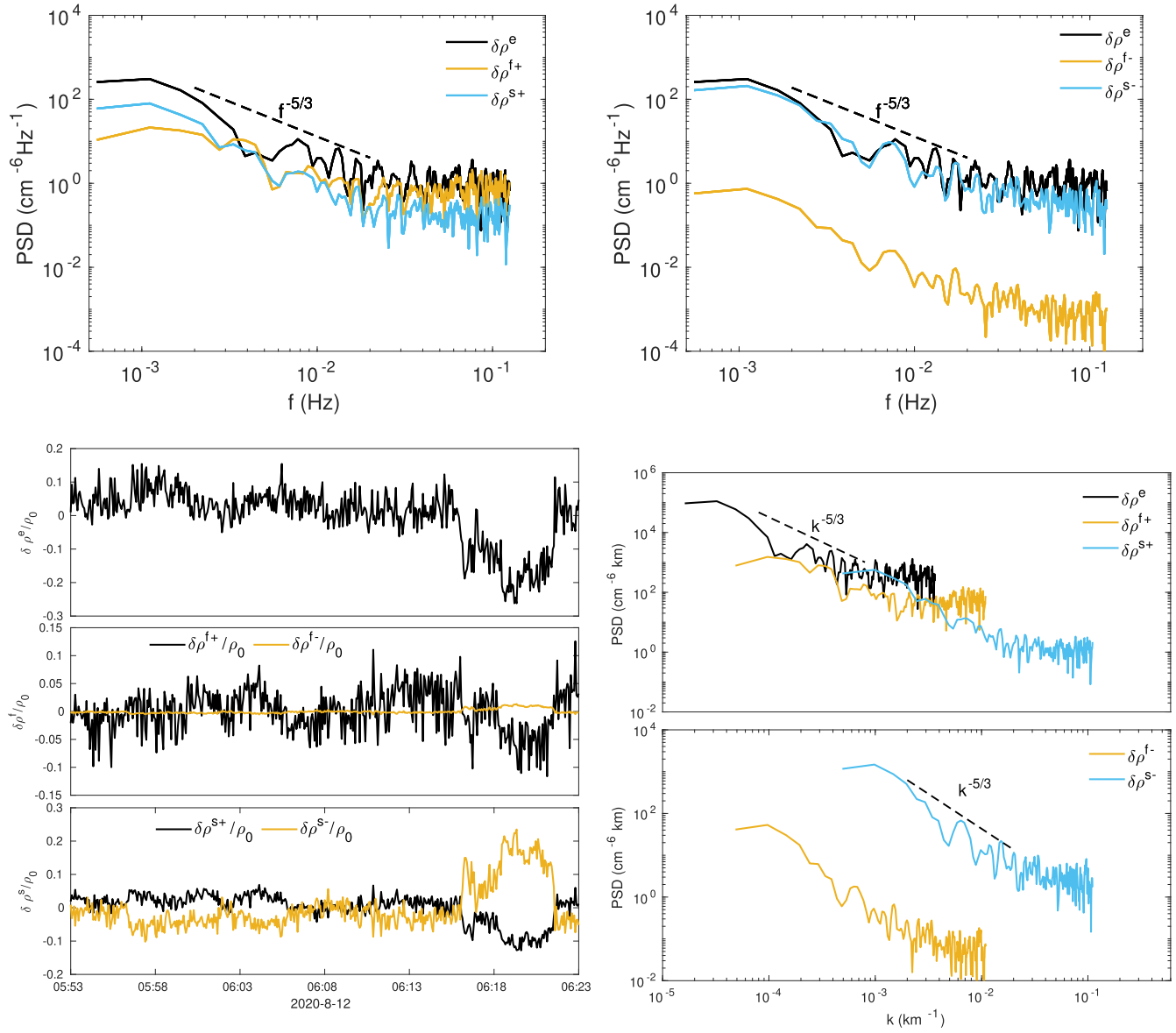


**Figure 14.** Mode decomposition over the highly aligned 30 minute interval showing the density fluctuations. Top row, left to right: the frequency spectra of the entropy, forward fast and slow, and backward fast and slow magnetosonic modes, $\delta\rho^{e}$, $\delta\rho^{f\pm}$, and $\delta\rho^{s\pm}$; Bottom left: from top to bottom the entropy mode and the forward and backward fast and slow magnetosonic modes. Bottom right: PSDs in isotropic wavenumber $k$ of the entropy the and forward- (top) and backward-propagating magnetosonic modes (bottom). All fluctuating quantities are normalized to the mean density as labeled.

and forward Alfvén waves are nearly three orders of magnitude larger than their compressible fast- and slow-mode counterparts. It is interesting to note that the decomposition reveals the presence of Alfvénic structures with $\theta^{A+} = 90°$, i.e., non-propagating, highly oblique Alfvén vortices.

Before turning to the velocity spectra, we consider one more comparative test of the mode decomposition. This is illustrated in Figure 8. The orange curve represents an FFT-derived PSD of the transverse components of the original magnetic field data, and the black curve shows a PSD derived from a reconstruction of the transverse components obtained from the mode decomposition, i.e., the sum of the transverse magnetic field components extracted from the mode decomposition that separately yielded the transverse fluctuations corresponding to the Alfvén, magnetic island, forward fast, backward fast, forward slow, and backward slow modes. The PSD is plotted in frequency to avoid any complications associated with plotting in wavenumber. The accuracy of the comparison is notable, given that the FFT-derived spectrum makes no assumptions about linearity or small-amplitude fluctuations, unlike the mode-decomposition composite spectrum. This indicates that the mode-decomposition-based spectra, while limited, provide surprisingly good insight into the fully nonlinear spectrum, and this suggests that the modal spectra presented here and below should be quite an accurate representation of the various modes.

We follow the format of Figure 7 in plotting the fluctuating velocity/kinetic energy PSDs in Figure 9, except there is of course no magnetic island contribution. The top two panels show frequency velocity PSDs for forward (left) and backward

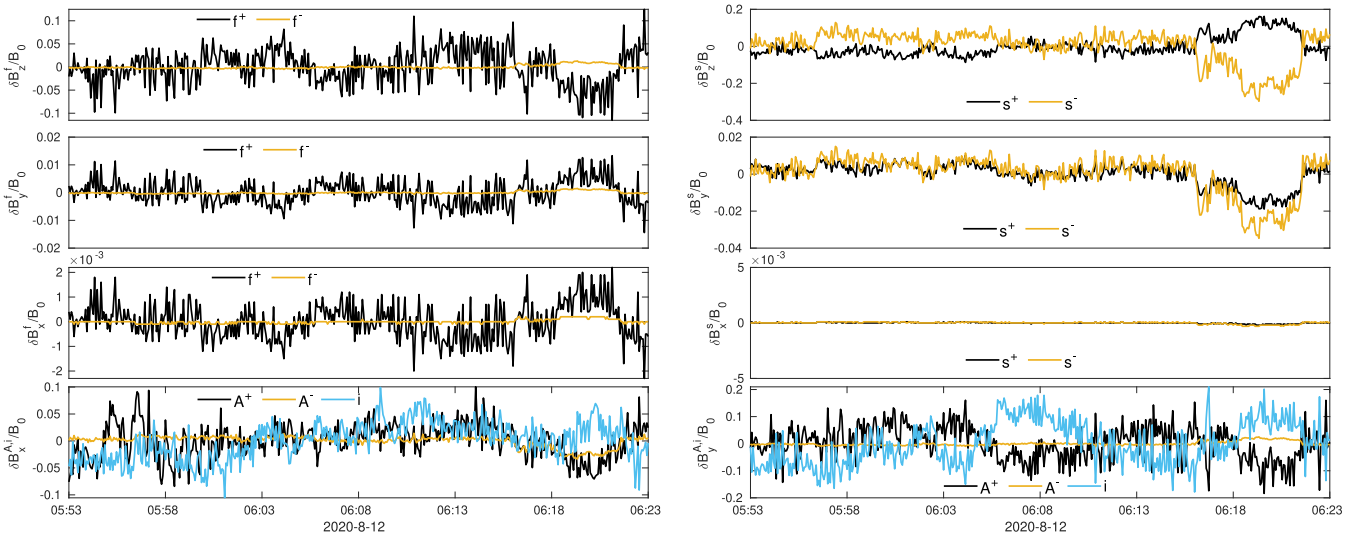


**Figure 15.** Mode decomposition in the mean-field coordinates for the aligned case showing separately the contributions to the normalized fluctuating magnetic field from top to bottom. Left column: the forward and backward fast $\delta B^{f\pm}_{z,y,x}$ magnetosonic modes, respectively, and the forward and backward $x$-components of the Alfvén mode $\delta B^{A\pm}_{x}$ and the magnetic island mode $\delta B^{i}_{x}$. Right column: the forward and backward slow $\delta B^{s\pm}_{z,y,x}$ magnetosonic modes, respectively, and the forward and backward $y$-component of the Alfvén mode $\delta B^{A\pm}_{y}$ and the magnetic island mode $\delta B^{i}_{y}$. All fluctuating quantities are normalized to the mean magnetic field strength as labeled.

(right) propagating Alfvén, slow, and fast modes. The frequency spectra transformed to parallel wavenumber (middle panels) and perpendicular wavenumber (bottom panels) are shown below. The comments made about the Alfvén and fast and slow magnetosonic modal spectra in discussing the magnetic field fluctuations carry over to the kinetic energy spectra.

Figures 10 and 11 are essentially the same because of the eigenrelationship between $\delta\rho^{fs\pm}$ and $\delta p^{fs\pm}$. The left and middle panels of Figure 10 show the density PSDs for the entropy as well as the forward (left) and backward (middle) fast and slow magnetosonic modes as a function of frequency. In the frequency density spectra for the entropy and forward modes, the amplitudes are all similar but the backward fast-mode spectrum lies well below the entropy and backward slow-mode spectra. However, replotting the entropy and forward fast and slow modes in wavenumber space $k$ yields overlapping spectra that form effectively a single power-law spectrum in $k$. A $k^{-5/3}$ curve is plotted to guide the eye. Although overlapping, the modal contributions to the density spectra are ordered from smallest to largest $k$ according to entropy, fast, and slow mode. As shown and expected, the same spectral form in wavenumber $k$ is true for the fluctuating pressure, as illustrated in Figure 11, except that only the fast and slow modes contribute.

In concluding this subsection, we describe briefly the effect of using smaller intervals. We subdivide the 30 minute interval into six subintervals of 5 minutes each and apply the $8 \times 8$ mode decomposition to each of the subintervals. In each subinterval, a distinct set of mean values $\rho_0$, $P_0$, $\boldsymbol{U}_0$, and $\boldsymbol{B}_0$ is determined, different from the mean values used in the 30 minute decomposition. In Figure 12, we compare the 30 minute mode decomposition with a combined set of six 5 minute mode decompositions, using the same format as in Figure 6. The figures in the left column, from top to bottom, show the total fluctuating pressure $\delta p$, fluctuating magnetic field components $\delta B_{z,y,x}$, fluctuating density $\delta\rho$, and fluctuating velocity components $\delta u_{z,y,x}$, respectively, from the summed 30 minute mode decomposition, i.e., the application of the MVA and mode decomposition to the entire 30 minute interval, and the results are overplotted with the measured values for the fluctuations $\delta\Psi_m$. The right column shows the corresponding six "stitched together" subintervals with the same ordering from top to bottom, using again an application of the MVA and $8 \times 8$ mode decomposition to each 5 minute interval. The total interval of course corresponds to the complete 30 minute interval.

Evidently, the left and right plots for $\delta\Psi$ and $\delta\Psi_m$ are similar, although different in detail. The differences in the representations of the fluctuations stem from the distinct values taken by the mean values $\Psi_0$ (30 minutes) versus $\Psi^i_0$ (5 minutes), $i = 1 \cdots 6$, and indeed this can be anticipated from inspection of Figure 2 where it is clear that mean plasma and magnetic values for shorter intervals will be different from mean values derived from the full 30 minute interval. The particular choice of interval on which to examine the characterization of solar wind fluctuations will depend on the questions and scales being addressed. Regardless of this separate question, two conclusions can be drawn from Figure 12, these being that the mode decomposition works equally well for the multiple 5 minute intervals as well as the single 30 minute interval, and the discrepancy between the reconstructed and measured data in the 90 s located between the 5–8 minute intervals remains.

The spectral characteristics of the 5 minute subintervals have been examined, and modest differences between the spectra extracted from the full 30 minute interval exist, largely due to the reduced sampling. For conciseness, the 5 minute spectral figures are not reproduced here.

### *4.2. Highly Aligned Flow Interval*

We need to recognize that a single spacecraft is constrained in the nature of the fluctuations that it can physically measure. In a highly aligned flow, i.e., one in which the mean flow velocity vector is highly aligned with the mean magnetic field

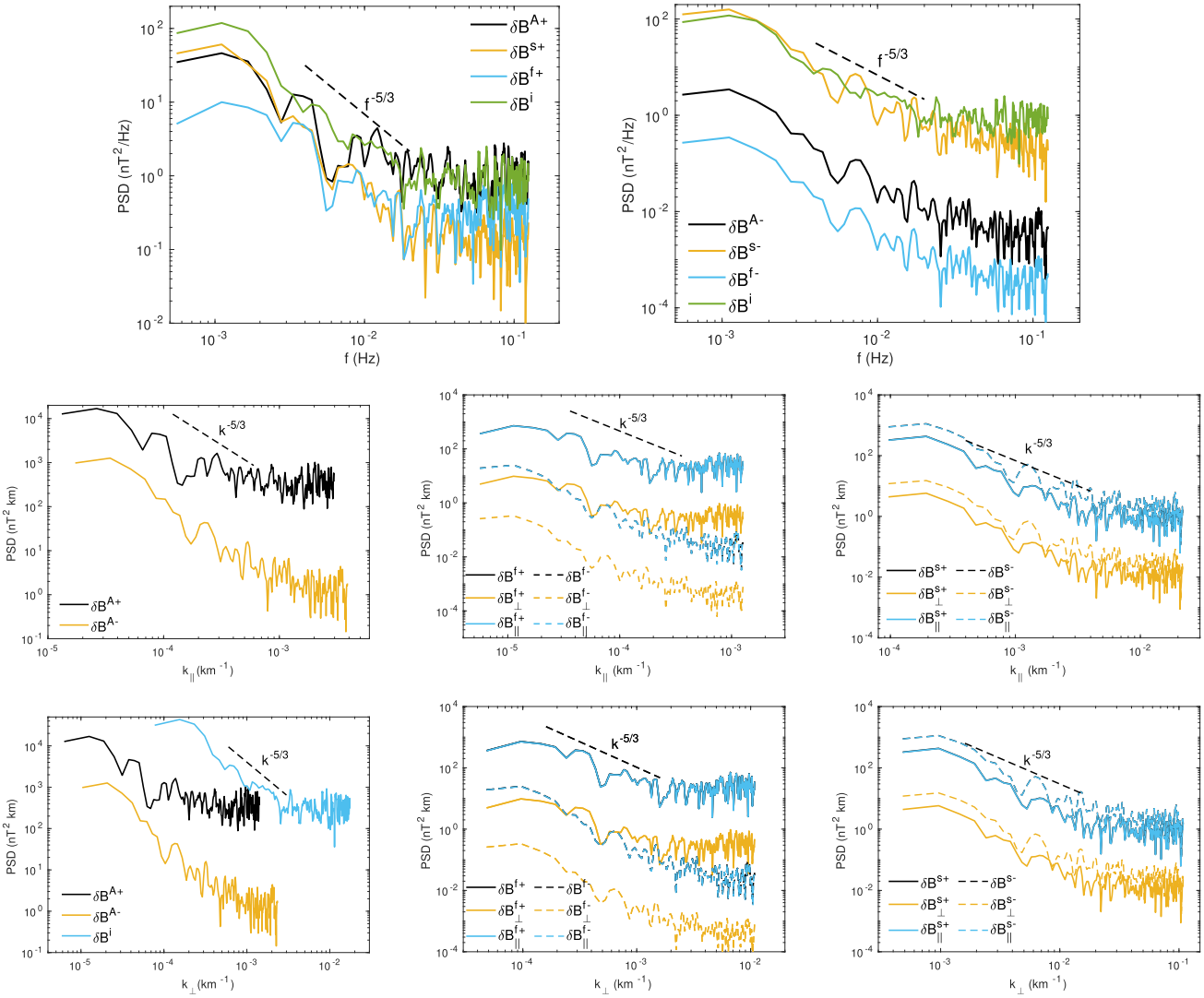


**Figure 16.** PSD plots of the fluctuating magnetic field for the aligned flow case. Top row: the frequency spectra of the magnetic island, forward Alfvén, fast, and slow magnetosonic modes (left); and the spectra of the magnetic island and backward Alfvén, fast, and slow magnetosonic modes (right). The dashed black line in each plot is a reference $f^{-5/3}$ curve. Middle row: the parallel wavenumber spectra of the forward and backward Alfvén mode magnetic field fluctuations (left), the parallel wavenumber spectra of parallel wavenumber spectra of the parallel and perpendicular components, and the total magnetic field fluctuations of the fast magnetosonic modes (middle); the parallel wavenumber spectra of the parallel and perpendicular components, as well as the total magnetic field fluctuations of the slow magnetosonic modes (right). Bottom row: the perpendicular wavenumber spectra of the magnetic island and forward and backward Alfvén mode magnetic field fluctuations (left), the perpendicular wavenumber spectra of the parallel and perpendicular components, and the total magnetic field fluctuations of the fast magnetosonic modes (middle); and the perpendicular wavenumber spectra of the parallel and perpendicular components, as well as the total magnetic field fluctuations of the slow magnetosonic modes (right).

vector, the plasma and magnetic field instruments cannot easily measure fluctuations in a plane orthogonal to the mean magnetic field or that are functions of $\boldsymbol{k}_\perp$ only. This therefore means that 2D magnetic and velocity fluctuations that are functions of $\boldsymbol{k}_\perp$ only may be undersampled, unlike fluctuations that have a $k_\parallel$ dependence. Of course, no flow is perfectly aligned with the mean magnetic field, but the ability to measure certain fluctuations may be inhibited. Alternatively, a single spacecraft measuring fluctuations in a mean flow that is highly oblique to the mean magnetic field cannot easily measure disturbances that are propagating along the mean magnetic field. In this case, Alfvénic modes may be undersampled, unlike the magnetic island modes. This geometric flow–magnetic field alignment effect on the measurement of magnetic field fluctuations by a single spacecraft has been exploited to good effect by Bieber et al. (1996), Saur & Bieber (1999), Forman et al. (2011), Zank et al. (2020), Bandyopadhyay & McComas (2021), Adhikari et al. (2021, 2022a, 2022b), and Zhao et al. (2022b) in evaluating spectral anisotropy of MHD turbulence in the solar wind. Here, we apply the mode decomposition to a highly aligned flow interval, and below to an interval that has a highly oblique mean flow-magnetic field orientation, in order to assess differences in the resulting decompositions. This should not be interpreted as a statistical study analogous to those just cited.

Plotted in Figure 13 is an overview of a slow solar wind flow that is approximately aligned with the mean magnetic field, as illustrated in the $\theta_{BV}$ panel. The panel from top to bottom shows the magnitude of magnetic field, the $R$, $T$, and $N$ components of the magnetic field and solar wind speed, angle

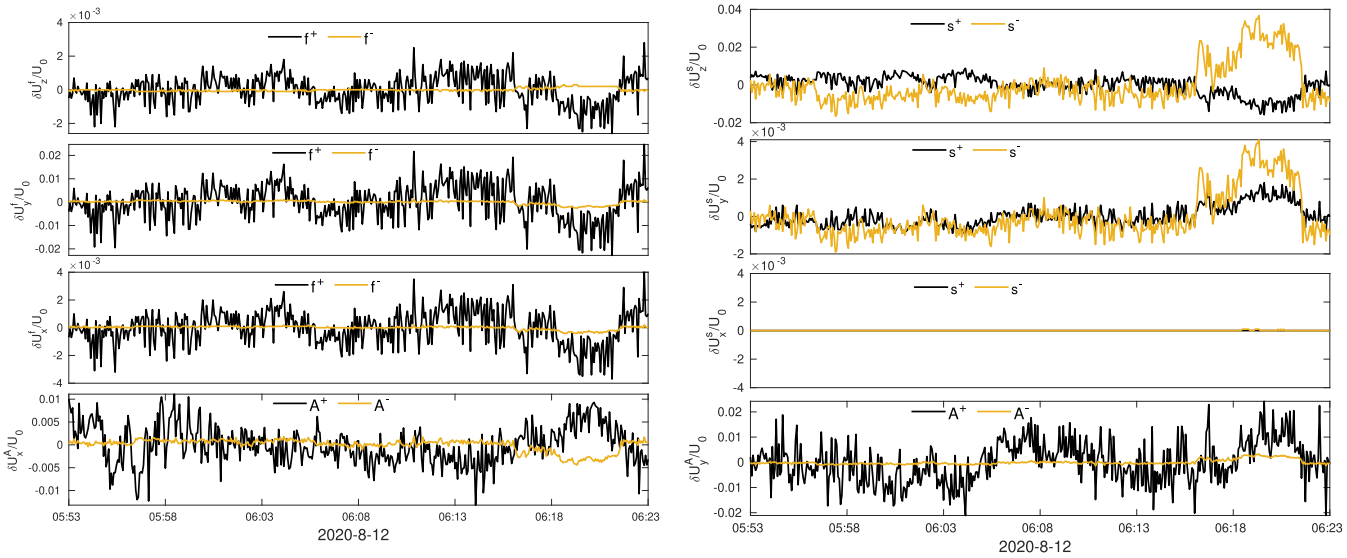


**Figure 17.** Mode decomposition in the mean-field coordinates for the aligned case, showing separately the contributions to the normalized fluctuating velocity from top to bottom. Left column: the forward and backward fast $\delta u^{f\pm}_{z,y,x}$ magnetosonic modes, respectively, and the forward and backward $x$-components of the Alfvén mode $\delta u^{A\pm}_{x}$. Right column: the forward and backward slow $\delta u^{s\pm}_{z,y,x}$ magnetosonic modes, respectively, and the forward and backward $y$-components of the Alfvén mode $\delta u^{A\pm}_{y}$. All fluctuating quantities are normalized to the mean flow speed as labeled.

$\theta_{BV}$, solar wind proton number density, and plasma beta $\beta_p$ measured by Solar Orbiter (Owen et al. 2020; Horbury et al. 2020) from (hh:mm) 05:53 to 06:23 on 2020 August 12. During this period, Solar Orbiter is at about 0.81 au. In the 30 minute interval, the magnetic field $|B|$ and $B_R$ increase gradually; $V_R$, $N_p$, and $\beta_p$ are approximately constant for about 23 minutes. These parameters then rotate for about 6 minutes, after which they remain constant.The angle between the flow and the magnetic field $\theta_{BV}$ varies between 5°.44 and 20°, with an average value of about 12°.23. Similarly, the plasma beta varies between 0.8 and 2.05. This range is in the $\beta_p \sim O(1)$ regime, i.e., the nearly incompressible MHD regime in which the turbulence corresponds to a superposition of a leading-order 2D turbulence description and a higher-order slab model (with compressible fluctuations entering at the same order) (Zank & Matthaeus 1992, 1993; Zank et al. 2017).

As discussed above, we transform the $R$, $T$, and $N$ components of the magnetic field and the solar wind speed into the mean-field coordinate system. The mean solar wind speed in the mean-field coordinates is about [75.24 0 358.36] km s$^{-1}$, and the mean magnetic field is [0 0 7.04] nT.

Figure 14 is a composite (top) of the frequency spectra of the entropy and fast and slow magnetosonic modes. The bottom left panel shows, from top to bottom, the normalized fluctuating density associated with the entropy mode, the forward and backward fast magnetosonic modes, and the corresponding slow modes. As seen in the frequency spectra, the entropy, forward fast, and backward slow magnetosonic modes are dominant, which differs from the oblique case discussed in Section 4.1. The backward fast mode is almost vanishingly small compared to the other modes. There is a distinct flattening in frequency spectra compared to the oblique flow density frequency spectra of Section 4.1, especially with the forward modes. For the Solar Orbiter SWA-PAS (proton and alphas) instrument (Owen et al. 2020), the moment sampling rate is 4 s, giving a Nyquist frequency of 0.019 Hz. While the flattening may be of interest (see, e.g., Šafránková et al. 2015, in which they identify flattening of the density spectrum near kinetic scales), this is not important in the context of this work. One should not overinterpret the flattening exhibited in the density/pressure spectra, because it occurs at frequencies higher than the Nyquist frequency (∼0.02 Hz) and needs to be studied separately and more carefully. The translation of the frequency spectra for the various modes into wavenumber spectra is illustrated in the two right bottom panels of Figure 14. The flattening of the spectra for the entropy and forward modes is very apparent in the $k$ plots and less so in the backward magnetosonic modes.

The mode decomposition of the fluctuating magnetic field is illustrated in Figure 15 using the same format as Figure 5. As for the oblique case of Section 4.1, the longitudinal amplitude $\delta\hat{B}_z$ of the magnetosonic modes dominates the amplitudes of the transverse components. As above, the backward fast mode is vanishingly small compared to the other magnetosonic modes. The bottom panels show the magnetic island and Alfvén wave magnetic field fluctuations. In this example, the amplitudes of the magnetic island and forward Alfvén mode, $\delta\hat{B}^{i,A+}_{x,y}$, far exceed that of the backward Alfvén mode. The mode decomposition allows one to calculate the exact normalized cross helicity for the Alfvén modes and not simply a cross helicity determined from measuring the transverse fluctuations, which could be contaminated by transverse contributions from other modes. Accordingly, we used the mode-decomposed Alfvén fluctuations to calculate the energy density in the forward and backward modes, subtracted the difference, and normalized to the total energy in the Alfvénic fluctuations. This yielded a normalized cross helicity $\sigma^A_c \sim 1$ for the Alfvén waves in the aligned interval, very reminiscent of the cross helicity in other highly aligned solar wind intervals investigated by Telloni et al. (2019), Zank et al. (2022), and Zhao et al. (2022c, 2022d) both in the super-Alfvénic and sub-Alfvénic solar winds.

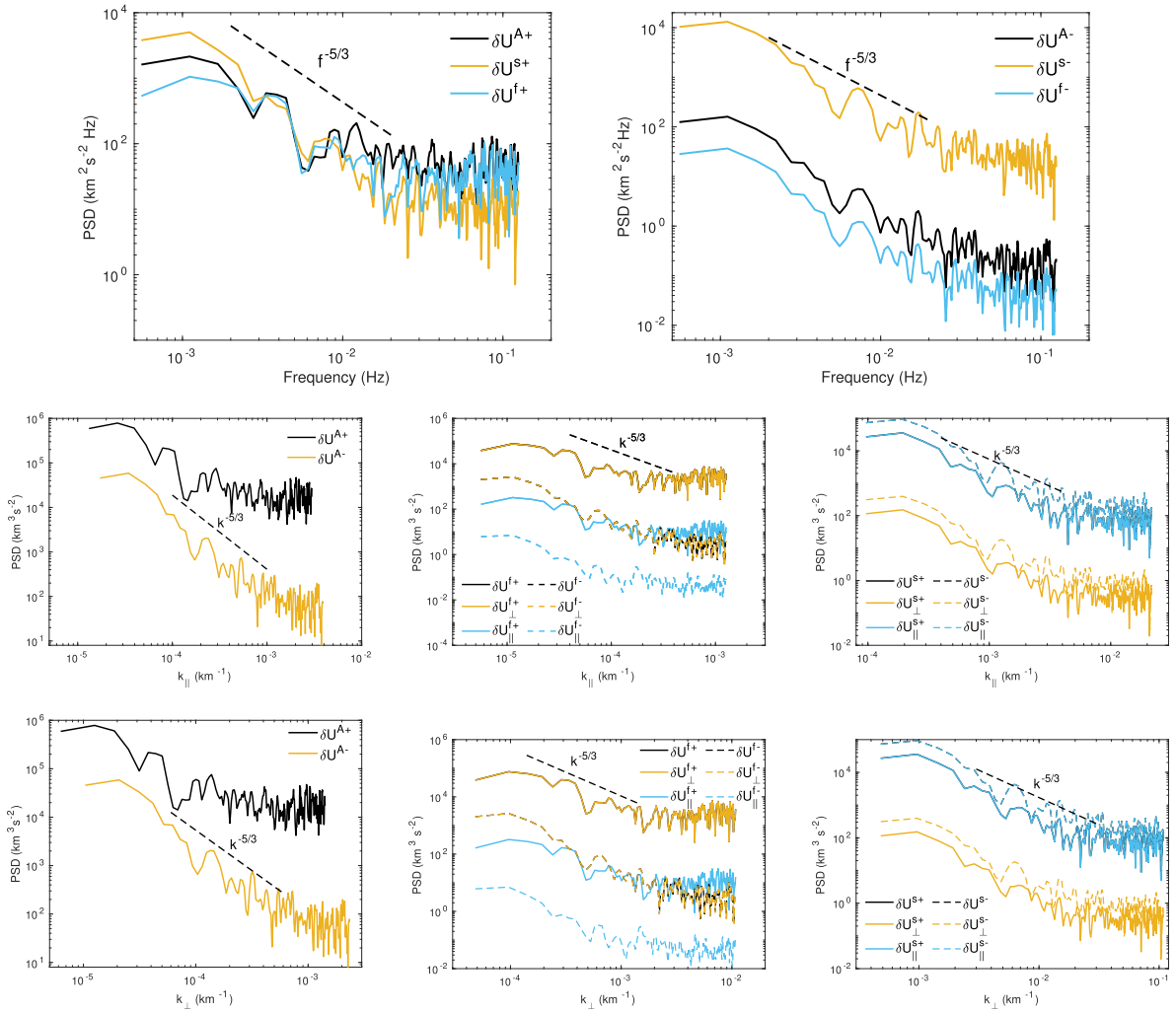


**Figure 18.** PSD plots of the fluctuating velocity field. Top row: the frequency spectra of the forward Alfvén, fast, and slow magnetosonic modes (left); and the spectra of the backward Alfvén, fast, and slow magnetosonic modes (right). The dashed line in each plot is a reference $f^{-5/3}$ spectrum. Middle row: the parallel wavenumber spectra of the forward and backward Alfvén mode velocity field fluctuations (left); the parallel wavenumber spectra of the parallel and perpendicular components, as well as the total velocity field fluctuations of the fast magnetosonic modes (middle); and the parallel wavenumber spectra of the parallel and perpendicular components, as well as the total velocity field fluctuations of the slow magnetosonic modes (right). Bottom row: the perpendicular wavenumber spectra of the forward and backward Alfvén mode velocity field fluctuations (left); the perpendicular wavenumber spectra of the parallel and perpendicular components, as well as the total velocity field fluctuations of the fast magnetosonic modes (middle); and the perpendicular wavenumber spectra of the parallel and perpendicular components, as well as the total velocity field fluctuations of the slow magnetosonic modes (right).

Despite being a highly aligned interval, the energy density in the magnetic island and forward Alfvén mode fluctuations is comparable, as is also illustrated in the frequency spectra plots of Figure 16. We note that the magnetosonic modes in the frequency spectra contain the fluctuating parallel component that is the dominant component. The translation of the frequency spectra to wavenumber spectra for all modes is illustrated in the middle and bottom panels of Figure 16. The middle panels show the spectra in terms of the parallel wavenumber $k_{||}$, and the bottom panels show them in terms of $k_\perp$. The middle left panel shows that the Alfvénic fluctuations are primarily forward with a spectrum that flattens, while the minority Alfvénic component $\delta B^{A-}$ appears to have a more extended $k_{||}^{-5/3}$-like spectrum. The Alfvénic spectra in $k_\perp$ in the panel below are similar. The magnetic island spectrum in $k_\perp$ extends to higher $k_\perp$ and also appears to flatten at high $k_\perp$. The energy density in the magnetic island and Alfvén modes is comparable. Although not examined in detail here, it would appear that the spectra for the incompressible fluctuations do not resemble well either critical balance, for which we might expect scaling relations of the form $k_\perp^{-5/3}$ and $k_{||}^{-2}$ or Iroshnikov–Kraichnan $k^{-3/2}$ scalings. The center and right middle and bottom panels illustrate the fast and slow magnetosonic mode spectra, respectively, with each panel plotting the forward and backward total, transverse, and parallel fluctuating components. As noted already, the parallel component is larger than the transverse contribution in each case. Both the forward and backward magnetosonic modes and the parallel and transverse wave components exhibit flattening of the $k_{||}$ and $k_\perp$ spectra.

The mode-decomposed velocity fluctuations are illustrated for the four magnetosonic and two Alfvén modes in Figure 17 for the highly aligned flow, and the corresponding spectra are shown in Figure 18. The backward Alfvén and fast magnetosonic modes are minority components in the velocity fluctuations as well. The velocity amplitudes of the $x$-

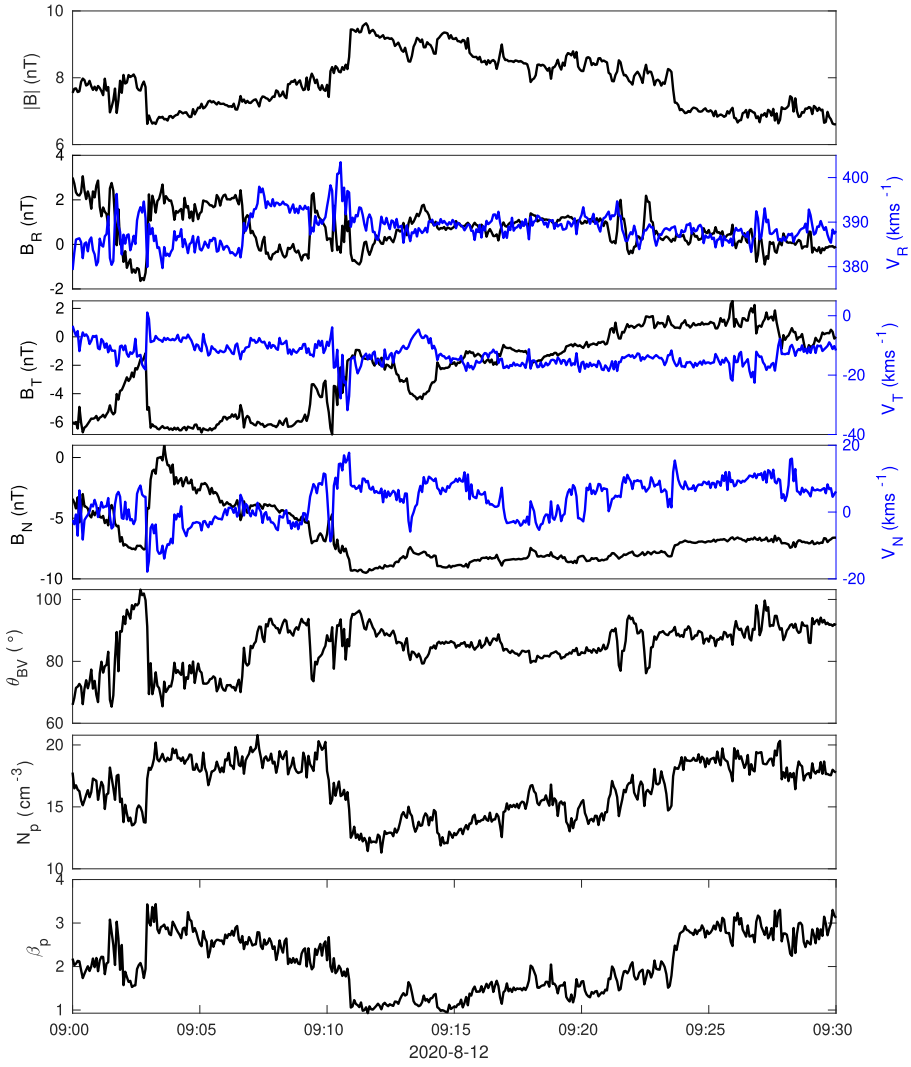


**Figure 19.** Overview of a 30 minute highly oblique slow solar wind interval observed by the Solar Orbiter spacecraft on 2020 August 12. From top to bottom, we plot the magnitude of the magnetic field $|B|$, the components of the magnetic field (left axis and black curves) and velocity field (right axis and blue curves) in the *RTN* coordinate system, the angle $\theta_{BV}$ between the magnetic and flow velocity vectors, the proton number density, and the proton plasma beta $\beta_p$.

component of the forward and backward slow modes contribute even less than the corresponding magnetic field fluctuations. The incompressible velocity spectra closely resemble the fluctuating magnetic field spectra, other than of course the absence of the magnetic island modes. The same flattening of the forward Alfvénic spectrum is exhibited, and the minority spectrum has a reasonable $k_{\parallel,\perp}^{-5/3}$ form. However, this is not true of the fast modes, where the amplitude of the transverse velocity fluctuation spectrum (forward and backward modes) well exceeds that of the parallel spectrum, quite unlike the corresponding magnetic field fluctuations. For the slow-mode forward and backward fluctuating spectrum, the parallel and transverse spectra resemble close those of the corresponding magnetic field fluctuations. In both cases, clear flattening of the magnetosonic mode spectra is seen.

### 4.3. Highly Oblique Flow Interval

Figure 19 shows an overview of a highly oblique slow solar wind flow measured by Solar Orbiter at (hh:mm) 09:00–09:30 in 2020 August 12. The panel from top to bottom displays the magnitude of the magnetic field, the $R$, $T$, and $N$ components of the magnetic field and solar wind speed, the angle $\theta_{BV}$, the solar wind proton number density, and the plasma beta $\beta_p$. The highly oblique 30 minute interval was measured about 2 hours and 30 minutes earlier than the highly field-aligned flow (Figure 13), and hence the two flows are at a similar distance of about 0.81 au. In the figure, $\theta_{BV}$ varies between 65° and 103°, and the average $\theta_{BV}$ is about 85°. Similarly, $\beta_p$ varies between 0.93 and 3.4, and for more than half the interval it is about 2 and above. Unlike the two prior examples, we might anticipate that this particular plasma beta regime places the interval in a nearly incompressible MHD regime in which the leading-order description is that of fully 3D incompressible MHD rather than the superposition description (2D plus slab) (Zank & Matthaeus 1992, 1993). Solar wind parameters, such as the proton density and the $R$, $T$, and $N$ components of the magnetic field and solar wind speed show large changes within the first 15 minutes, after which the SW parameters are reasonably smooth. The mean solar wind speed in mean-field coordinates is about [387 0 38.6] km s$^{-1}$ and the mean magnetic field is [0 0 7.03] nT.

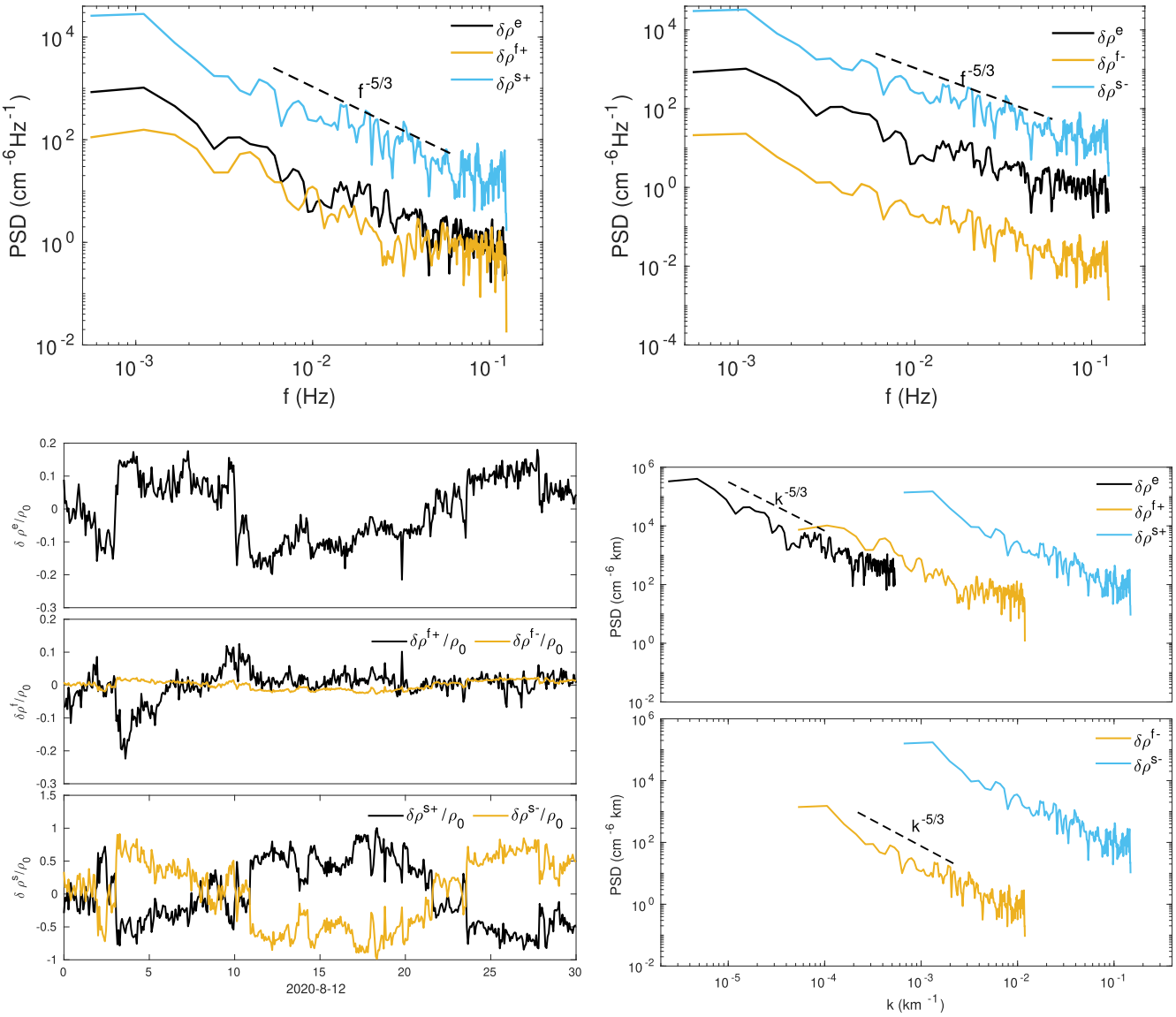


**Figure 20.** Mode decomposition over the highly oblique 30 minute interval showing the density fluctuations. Top row, left to right: the frequency spectra of the entropy, forward fast and slow, and backward fast and slow magnetosonic modes, $\delta\rho^e$, $\delta\rho^{f\pm}$, and $\delta\rho^{s\pm}$. Bottom left: from top to bottom, the entropy mode and the forward and backward fast and slow magnetosonic modes. Bottom right: PSDs in isotropic wavenumber $k$ of the entropy and forward-propagating (top) and backward-propagating magnetosonic modes (bottom). All fluctuating quantities are normalized to the mean density as labeled.

Corresponding to the format of Figure 14, we present the fluctuating density mode decomposition and spectra for the highly oblique case in Figure 20. The forward and backward slow modes have the largest amplitudes of the frequency PSD, with the entropy mode providing the next-most important contribution. The wavenumber plots confirm the important contribution of the slow-mode fluctuations, but the entropy and forward fast modes are equally important at longer wavelengths. The wavenumber plots of the composite density spectra now quite closely resemble those of the oblique case, Figure 10, both in the distribution of the three forward modes with respect to $k$ and in the overall spectral form $k^{-5/3}$. In this case, because the decomposition provides information for all wave modes, we plot separately the contribution from the two backward magnetosonic modes in the bottom right panel. The composite spectrum in this case exhibits a small step.

For this example, both fast magnetosonic modes are minority constituents of the various fluctuating components, as illustrated in Figures 21 and 22. The mode decomposition indicates that the forward and backward Alfvén modes, magnetic islands, and slow modes all contribute approximately equally to the energy in the fluctuations. This would be consistent with expectations of NI MHD in the high plasma beta regime. In this case, the normalized Alfvénic cross helicity $\sigma_c^A \sim 0$. The incompressible wavenumber spectra are quite different from those of the highly aligned and oblique cases discussed above, both of which were essentially in a $\beta_p \sim O(1)$ regime. The $k_\parallel$ and $k_\perp$ spectra for the Alfvénic fluctuations are Kolmogorov-like, as is the magnetic island spectrum. Furthermore, the $k_\perp$ Alfvénic and magnetic island spectra virtually overlay one another. As above, we have not examined the scalings in detail, but the spectra do not appear to be consistent

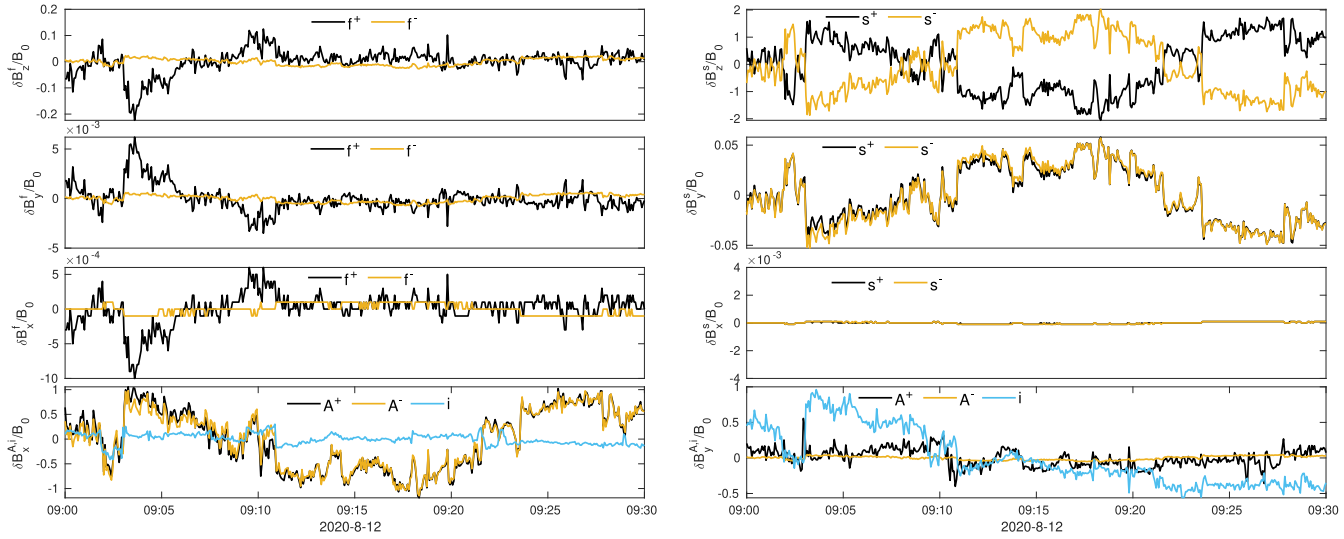


**Figure 21.** Mode decomposition in the mean-field coordinates for the highly oblique case, showing separately the contributions to the normalized fluctuating magnetic field from top to bottom. Left column: the forward and backward fast $\delta B^{f\pm}_{z,y,x}$ magnetosonic modes, respectively, and the $x$-component of the magnetic island and forward and backward Alfvén mode $\delta B^{i,A\pm}_{x}$. Right column: the forward and backward slow $\delta B^{s\pm}_{z,y,x}$ magnetosonic modes, respectively, and the $y$-component of the magnetic island and forward and backward Alfvén modes $\delta B^{i,A\pm}_{y}$. All fluctuating quantities are normalized to the mean magnetic field strength as labeled.

with either the critical balance hypothesis nor the Iroshnikov–Kraichnan spectral scalings, despite the apparently ideal conditions for the theories. The flattening of the minority fast-mode spectra that was apparent in the flow-aligned case is less obvious although present in this case. The dominant slow-mode spectra are clearly Kolmogorov-like.

The final set of plots correspond to the mode decomposition for the velocity fluctuations and the derived velocity mode spectra for the Alfvén and magnetosonic modes (Figures 23 and 24). The velocity PSD for the Alfvén modes is quite unlike the corresponding flow-aligned spectra, with the distinction between the forward and backward Alfvén modes being minimal in $k_\perp$ and essentially shifted in the $k_\parallel$ case. Some possible flattening at high $k$ may be present, but the spectra are essentially Kolmogorov-like. Similarly, some related flattening of the fast-mode spectra is present although less pronounced than in the flow-aligned case. The slow-mode spectra exhibit no flattening and are clearly Kolmogorov-like, quite unlike the $\beta_p \sim 1$ flow-aligned spectra.

## 5. Discussion and Conclusions

Linear MHD admits fundamental modes, six of which correspond to waves and two to advected modes. The problem of identifying these low-frequency modes in a quiet solar wind plasma parcel (or indeed in a computer-simulated plasma parcel) and determining their individual properties has not been satisfactorily resolved theoretically. In this paper, we develop a novel method to decompose a solar wind parcel into its fundamental or constituent MHD modes, provided the plasma parcel contains no large-amplitude (nonlinear) structures, such as shock waves, pressure-balanced structures, flux ropes associated with, e.g., coronal mass ejections, or current sheet crossings, for example. Prior attempts to develop an MHD mode decomposition method neglected to include advected modes, nor do they evaluate the phase information of the individual MHD fluctuations.

After reviewing briefly the derivation of the eight modes admitted by the linearized nonconservation form of the MHD equations, including deriving the eigenvector relations, we exploited the linearized conservation form of the MHD equations to derive a set of seven boundary conditions that the amplitudes and phases of the individual modes have to satisfy. The MHD conservation laws had to be augmented by an additional boundary condition appropriate to small-scale flux ropes, giving a total of eight conservation laws. The problem is not yet closed, because the eight boundary conditions contain eight unknown mode amplitudes and 24 unknown phases or wavenumber components associated with the normal linear modes. We show how to expand the plasma and magnetic field variables to derive a constrained set of phase relations that can be evaluated from the Doppler-shifted frequency measured by a spacecraft and an inferred "measured" wavenumber vector $\boldsymbol{k}_m$ for the plasma parcel of interest. The form of the phase relations or angles relative to the mean magnetic field makes an MVA approach to deriving $\boldsymbol{k}_m$ particularly attractive. Based on the derived phase information for each of the eight fundamental wave modes, the $8 \times 8$ matrix for the amplitudes of the fluctuating mode variables can be inverted uniquely to provide a linearly independent set that represents the MHD mode decomposition of an observed plasma parcel of suitably short duration. A decoherence timescale is derived that places bounds on the observation time of a plasma parcel to ensure the validity of the mode decomposition.

Because we utilize a linearized small-amplitude analysis, each mode, propagating or advected, admits a particular dispersion relation between the frequency and wavenumber. This implies that Taylor's hypothesis is not needed to convert frequency spectra to wavenumber spectra for any of the eight MHD modes, but of course the caveat above applies. Nonetheless, because the mode decomposition provides a description for the fluctuations observed in a plasma parcel, this correspondence of frequency and wavenumber provides

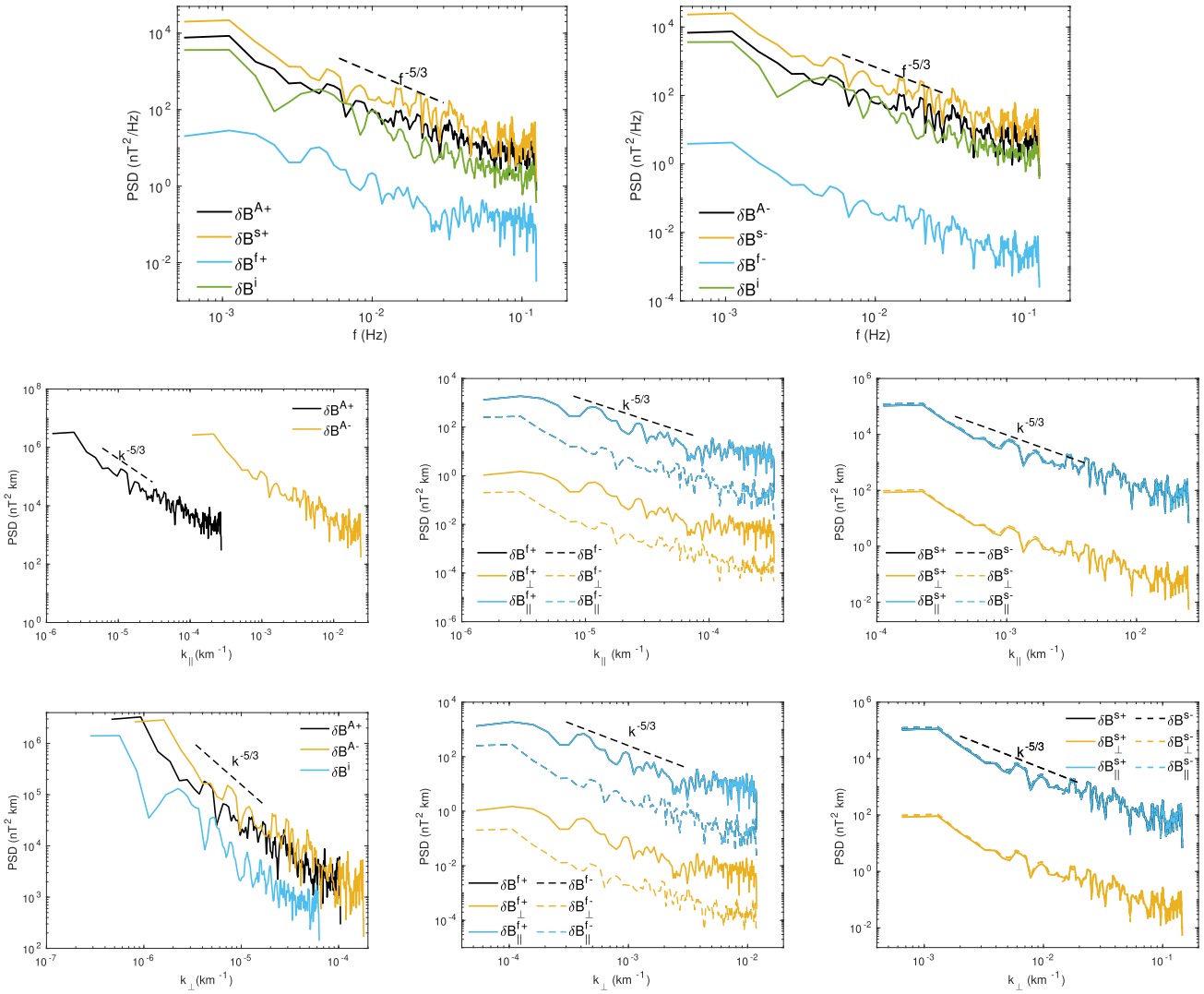


**Figure 22.** PSD plots of the fluctuating magnetic field for the highly oblique case. Top row: the frequency spectra of the magnetic island, forward Alfvén, fast, and slow magnetosonic modes (left); and the frequency spectra of the magnetic island and backward Alfvén, fast, and slow magnetosonic modes (right). The dashed line in each plot is a reference $f^{-5/3}$ spectrum. Middle row: the parallel wavenumber spectra of the forward and backward Alfvén mode magnetic field fluctuations (left); the parallel wavenumber spectra of the parallel and perpendicular components, as well as the total magnetic field fluctuations of the fast magnetosonic modes (middle); and the parallel wavenumber spectra of the parallel and perpendicular components, as well as the total magnetic field fluctuations of the slow magnetosonic modes (right). Bottom row: the perpendicular wavenumber spectra of the magnetic island and forward and backward Alfvén mode magnetic field fluctuations (left); the perpendicular wavenumber spectra of the parallel and perpendicular components, as well as the total magnetic field fluctuations of the fast magnetosonic modes (middle); and the perpendicular wavenumber spectra of the parallel and perpendicular components, as well as the total magnetic field fluctuations of the slow magnetosonic modes (right).

considerable insight into the nature of solar wind fluctuations that cannot be otherwise gained.

We provide a detailed algorithm for the mode decomposition of a plasma parcel observed in the solar wind, and we illustrate the method by implementing it for three 30 minute intervals using Wind and Solar Orbiter data at ∼1 au and ∼0.8 au, respectively. The three cases differ in the angle $\theta_{UB}$ between the mean velocity and the mean magnetic field vectors, one being an oblique configuration, another being highly aligned, and the last highly oblique. Furthermore, the three cases correspond to roughly two plasma beta $\beta_p$ regimes, $\beta_p \sim O(1)$, and $\beta_p > 1$. This algorithm can equally be applied to fluctuations measured in MHD simulations.

By way of validating the mode-decomposition method, we used two tests. In the first, we performed the mode decomposition and then reconstructed the total plasma density, pressure, and velocity and magnetic field vectors by summing the relevant contributions from each of the derived modes. The reconstructed data were then compared to the original data set, yielding excellent agreement—with the exception of one possible large-amplitude structure in the oblique case. A second test was to use the mode decomposition to construct the total fluctuating transverse magnetic field PSD from the relevant contributing modes, which was then compared to an FFT-generated PSD of the transverse fluctuations for the interval. As illustrated, the "linear" and the "nonlinear" PSDs are identical in their basic characteristics (spectral form, power) and virtually overlay one another. In short, despite being an essentially linear description, the mode decomposition provides a surprisingly accurate description of the original underlying data.

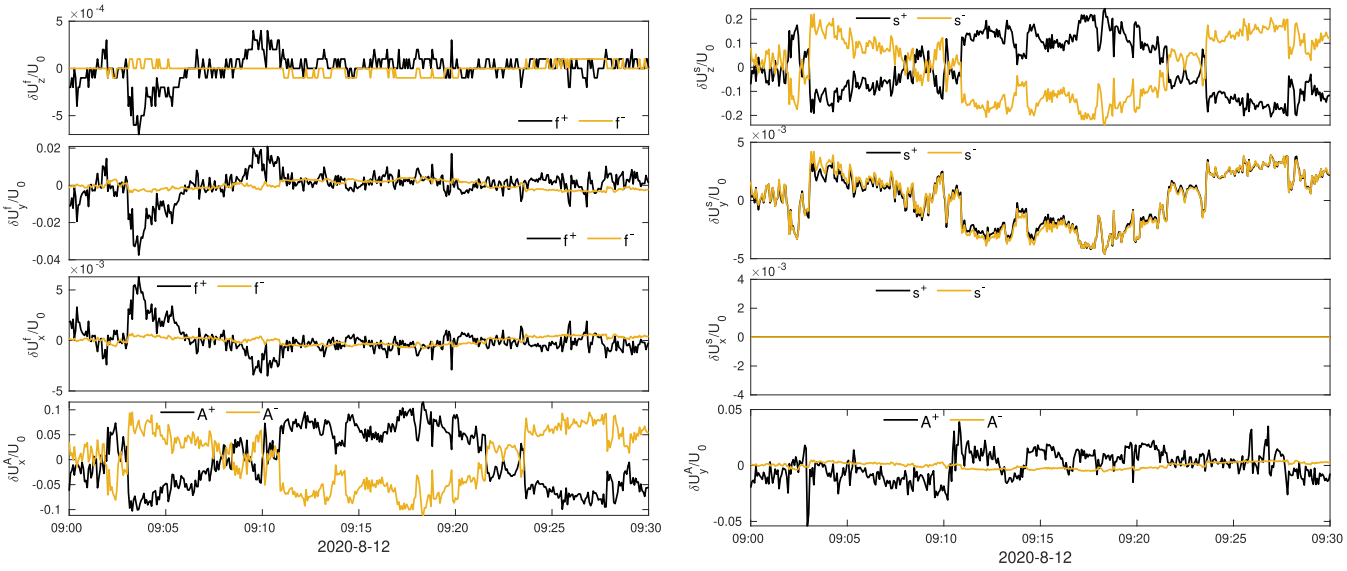


**Figure 23.** Mode decomposition in the mean-field coordinates for the highly oblique case, showing separately the contributions to the normalized fluctuating velocity from top to bottom. Left column: the forward and backward fast $\delta u^{f\pm}_{z,y,x}$ magnetosonic modes, respectively, and the forward and backward $x$-components of the Alfvén mode $\delta u_x^{A\pm}$. Right column: the forward and backward slow $\delta u^{s\pm}_{z,y,x}$ magnetosonic modes, respectively, and the forward and backward $y$-components of the Alfvén mode $\delta u_y^{A\pm}$. All fluctuating quantities are normalized to the mean flow speed as labeled.

Although the focus of the paper was to develop a new mode-decomposition method that incorporated both nonpropagating MHD modes and phase information, the examples to which we applied the new approach yielded novel and very interesting results about fluctuations in the solar wind at 1 and 0.81 au. These results are listed briefly below.

1. The mode-decomposition method allowed us to make the first identification of density fluctuations associated with entropy modes. Unlike density fluctuations associated with magnetosonic modes, these are nonpropagating or advected density fluctuations, and in all the cases considered here they comprise an important and dominant low-frequency, small $k$ component. A Kolmogorov-like power law $k^{-5/3}$ is typical of the entropic density fluctuations with the possibility of a slight flattening at higher $k$-values.
2. The mode decomposition distinguishes between entropy as well as forward and backward fast and slow magnetosonic density fluctuations, and each mode forms an independent power-law PSD in wavenumber, ordered in $k$-space from small to large wavenumber according to entropy, fast, and slow modes. Sometimes, the combined density spectrum from all the modes appears to resemble a single-density PSD with a $\sim k^{-5/3}$ power law. At other times, the total combined density PSD does not appear to be continuous but has instead jumps between the spectra of different modes, giving the appearance of broken spectra. This is true when one or more modes appear to be especially dominant.
3. The pressure fluctuations associated with the fast and slow magnetosonic modes are directly correlated with their density fluctuations, and therefore the normalized spectra are identical. We note in passing that this corresponds directly to the pseudosound approximation introduced into nearly incompressible hydrodynamics and MHD (Montgomery et al. 1987; Matthaeus & Brown 1988; Zank & Matthaeus 1990, 1992, 1993; Zank et al. 1990).
4. The mode decomposition of the observed magnetic fluctuations identifies the longitudinal and transverse components of the fast and slow magnetosonic modes, i.e., the compressible fluctuating magnetic field components. We found intervals in which the longitudinal component was much larger than the corresponding transverse component of the compressible fluctuations. For example, in the oblique example for which $\beta_p \sim O(1)$, $\delta B_\parallel^{f,s}$ dominated $\delta B_\perp^{f,s}$. Both components of the fast and slow modes exhibited Kolmogorov-like spectra with $k_\parallel^{-5/3}$ and $k_\perp^{-5/3}$. For the highly flow-aligned and highly oblique cases, we considered the forward and backward fast and slow modes separately, finding that the longitudinal component was still dominant in each case with spectra close to $k_{\parallel,\perp}^{-5/3}$ but having high $k$ flattening. Not surprisingly, the results are related closely to the corresponding velocity fluctuations, including the spectra.
5. The mode decomposition of the incompressible magnetic field fluctuations identifies the magnetic island component and the forward and backward Alfvén modes. In the case of oblique flows with $\beta_p \sim O(1)$, we find that the magnetic island component dominates the transverse fluctuations, and the Alfvénic fluctuations correspond primarily to the forward (+) component whereas the backward (−) Alfvénic fluctuations are a minority component. We find that the Alfvénic cross helicity $\sigma_c^{A+} \simeq +1$, indicating essentially unidirectional Alfvén wave propagation. The Alfvén wave spectra for $A\pm$ are both given by $\sim k_\parallel^{-5/3}$ and $k_\perp^{-5/3}$, and the magnetic island spectrum is described by $k_\perp^{-5/3}$. The incompressible magnetic field fluctuations dominate the compressible magnetosonic fluctuations (longitudinal and transverse). The highly flow-aligned case, possibly because it has only a slightly different plasma beta value, yields results

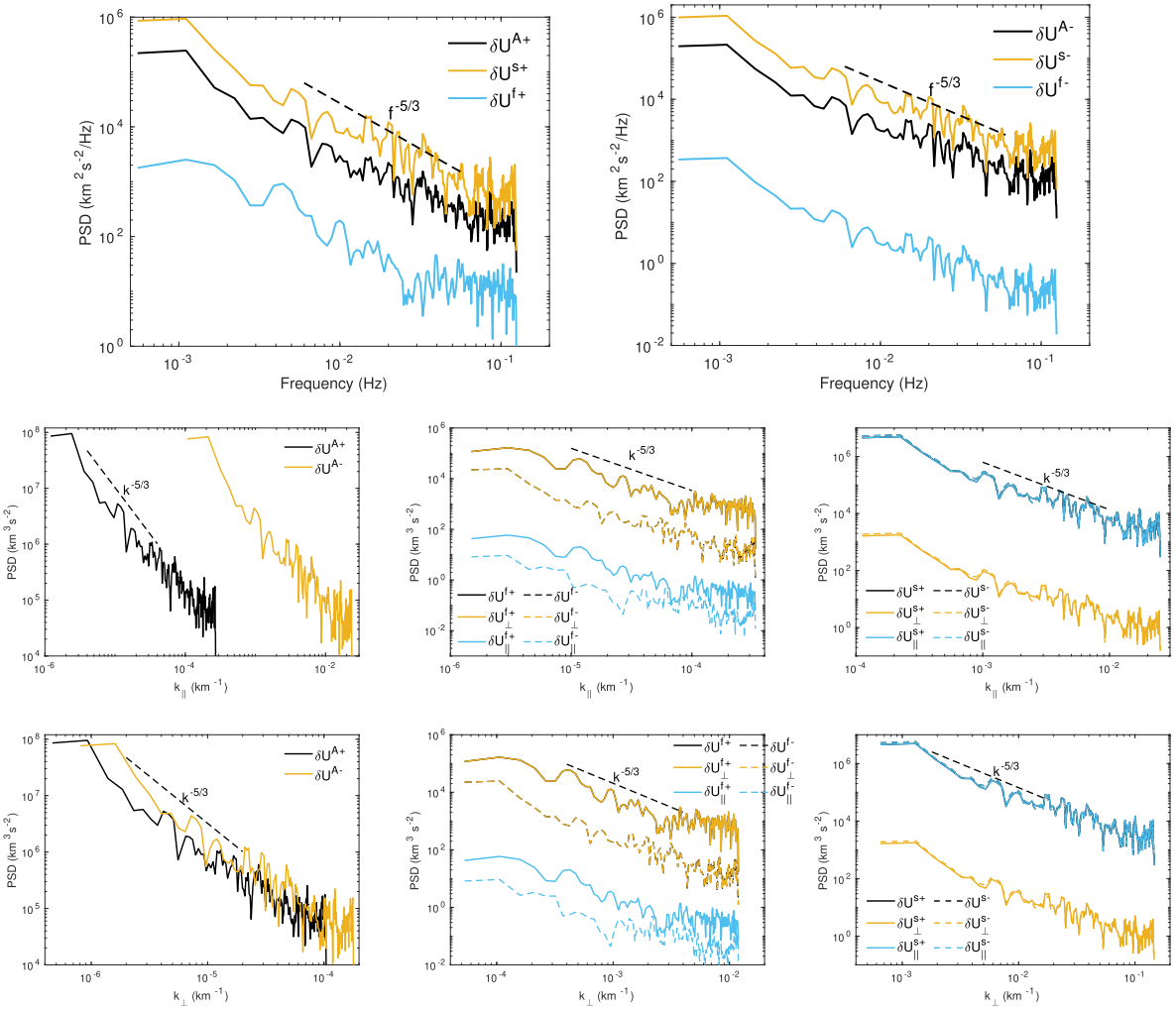


**Figure 24.** PSD plots of the fluctuating velocity field highly oblique case. Top row: the frequency spectra of the forward Alfvén, fast, and slow magnetosonic modes (left); and the spectra of the backward Alfvén, fast, and slow magnetosonic modes (right). The dashed line in each plot is a reference $f^{-5/3}$ spectrum. Middle row: the parallel wavenumber spectra of the forward and backward Alfvén mode magnetic field fluctuations (left); the parallel wavenumber spectra of the parallel and perpendicular components, as well as the total velocity field fluctuations of the fast magnetosonic modes (middle); and the parallel wavenumber spectra of the parallel and perpendicular components, as well as the total velocity field fluctuations of the slow magnetosonic modes (right). Bottom row: the perpendicular wavenumber spectra of the forward and backward Alfvén mode magnetic field fluctuations (left); the perpendicular wavenumber spectra of the parallel and perpendicular components, as well as the total velocity field fluctuations of the fast magnetosonic modes (middle); and the perpendicular wavenumber spectra of the parallel and perpendicular components, as well as the total velocity field fluctuations of the slow magnetosonic modes (right).

quite similar to the oblique case. For the highly oblique case in which $\beta_p \geqslant 2$ over much of the 30 minute interval, we found that the magnetic island and forward and backward Alfvén modes were roughly balanced, which appears to be consistent with NI MHD in the large plasma beta regime.

Finally, possible sources of inaccuracy and error are of course related to the accuracy of the inferred value of the "measured" wavenumber $\boldsymbol{k}_m$ . We used Taylor's hypothesis for the full 30 minute plasma parcel, which seems a reasonable assumption for a plasma parcel of this scale, and this yielded a very natural estimate of the ratio $\omega'_m/k_m$ between the measured frequency and the magnitude of the wavenumber. Nonetheless, exploring different methods to estimate $\boldsymbol{k}_m$ would be valuable. Second, single-spacecraft sampling of either highly aligned or highly oblique (with respect to the mean magnetic field and velocity vector) flow configurations can favor the observation of either $\boldsymbol{k}_\parallel$ or $\boldsymbol{k}_\perp$ dominant fluctuations, respectively (Zank et al. 2021b; Adhikari et al. 2022a, 2022b). The resulting mode decomposition may therefore be deficient in one or the other class of fluctuations. Fortunately, most flow-magnetic field configurations in solar wind plasma parcels are rarely perfectly aligned or perpendicular, and so this measurement problem may not be especially severe. As illustrated in the examples presented here, the mode decomposition appears to work reasonably well for what are nominally highly aligned or highly oblique cases.

To summarize, we have developed a new mode-decomposition method that resolves a solar wind plasma parcel into its eight fundamental or constituent MHD modes, i.e., two advected modes (the entropy and magnetic island modes) and the usual six propagating wave modes (two Alfvén, two fast, and two slow magnetosonic modes). The decomposition yields both the amplitude and phase for each mode, and all are related to the observed frequency and inferred wavenumber. Thanks to the small-amplitude assumption, linearity ensures that the frequency and wavenumber spectra for each mode are related

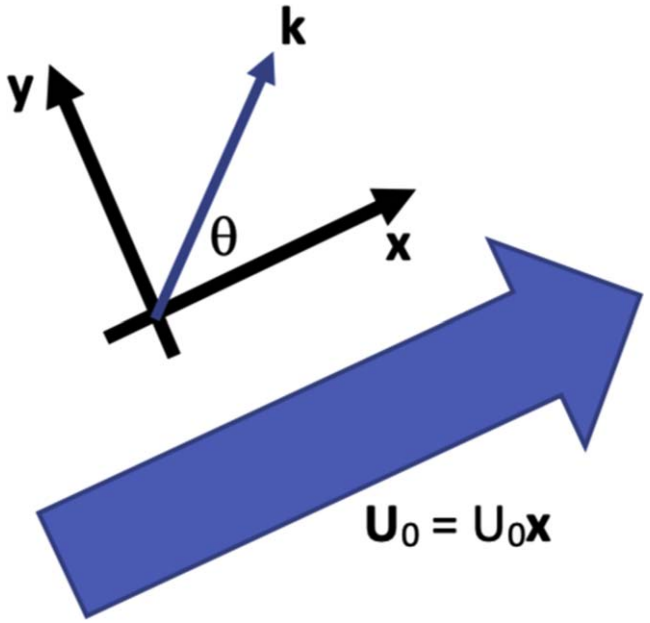


**Figure 25.** The assumed coordinate system with the mean flow vector $\boldsymbol{U}_0$ aligned along the $\hat{x}$-axis. The 2D wavenumber coordinates are also illustrated.

via the appropriate dispersion relations rather than Taylor's hypothesis. Although limited in this regard, the decomposition proves a surprisingly accurate description of the data, allowing for an accurate reconstruction of both the measured time series data and the spectral data derived from a standard FFT of the fluctuations in the given interval. Therefore, this provides considerable insight into both identifying specific low-frequency MHD modes and determining their individual properties and spectral characteristics.

## Acknowledgments

G.P.Z., L.Z., L.A., and M.N. acknowledge the partial support of a NASA Parker Solar Probe contract SV4-84017, an NSF EPSCoR RII-Track-1 Cooperative Agreement OIA—2148653, a NASA IMAP subaward under NASA contract 80GSFC19C0027, a NASA award 80NSSC20K1783, and a NASA Heliospheric DRIVE Center award SHIELD 80NSSC22M0164. A.P. acknowledges the partial support of the Czech Grant Agency under contract (23-06401S).

## Appendix A
## 2D Hydrodynamic Case

The simplest nontrivial case with which to consider mode decomposition is that of 2D hydrodynamics. We assume there exists a measured mean background ideal gas state $\rho_0$, $\boldsymbol{U}_0$, and $P_0$ (density, flow velocity, and pressure), and corresponding fluctuations $\delta\rho_m$, $\delta\boldsymbol{u}_m$, and $\delta p_m$, measured at a frequency $\omega_m'$ and corresponding wavenumber $\boldsymbol{k}_m$ in a laboratory or spacecraft frame.

It is well-known (McKenzie & Westphal 1968; Zank et al. 2021a) that 2D hydrodynamics admits four linear small-amplitude modes: advected entropy and vorticity modes, and propagating fast (+) and slow(−) acoustic waves. Their linear dispersion relations and eigenrelations are given by the following modes:

*Acoustic modes* $\omega' = \pm a_0 k$, where $\omega' \equiv \omega - \boldsymbol{U_0}\cdot\boldsymbol{k} \neq 0$, with eigenrelations

$$\delta\hat{\rho} = \frac{\delta\hat{p}}{a_0^2},\ \ \delta\hat{\boldsymbol{u}} = \mp\frac{\boldsymbol{k}/k}{\rho_0 a_0}\delta\hat{p},\ \ \delta\hat{\boldsymbol{B}} = 0,\ \ a_0^2 = \frac{\gamma P_0}{\rho_0}$$
(sound speed). (A1)

*Entropy modes* $\omega' = 0$ with eigenrelations

$$\delta\hat{s} = -\frac{\gamma\delta\hat{\rho}}{\rho_0},\ \ \delta\hat{p} = 0,\ \ \delta\hat{\boldsymbol{u}} = 0,\ \ \delta\hat{\boldsymbol{B}} = 0,\ \ \delta\hat{\rho}\ \ \text{arbitrary}. \tag{A2}$$

*Vortical modes* $\omega' = 0$, with eigenrelations, after introducing $\boldsymbol{k} = k(\cos\theta, \sin\theta) \equiv k(\alpha, \beta)$,

$$\delta\hat{p} = 0,\ \ \delta\hat{\boldsymbol{B}} = 0,\ \ \delta\hat{\rho} = 0,\ \ \delta\hat{\boldsymbol{u}} \neq 0,\ \ \delta\xi_z \neq 0;$$
$$\boldsymbol{k}\cdot\delta\hat{\boldsymbol{u}} = 0 \Longrightarrow \delta\hat{\boldsymbol{u}} = \delta\hat{u}(-\beta, \alpha). \tag{A3}$$

Here, $\boldsymbol{U}_0$ is the mean bulk flow velocity, $\delta\Psi$ corresponds to the perturbed gas variables, i.e., $\Psi = \Psi_0 + \delta\Psi$, and $\delta\hat{\Psi}$ is the amplitude associated with the normal mode, i.e., $\delta\Psi = \delta\hat{\Psi}\exp[i(\omega t - \boldsymbol{k}\cdot\boldsymbol{x})]$, $\boldsymbol{x} = (x, y)$, and the wavenumber is $\boldsymbol{k} = (k_x, k_y)$.

We adopt the coordinate system illustrated in Figure 25, i.e., where the mean flow velocity $\boldsymbol{U}_0$ is aligned with the $\hat{\boldsymbol{x}}$-axis.

By defining a surface such that the normal is aligned with $\boldsymbol{U}_0$, the perturbed conservation form of the 2D gas dynamic equations can be expressed as

$$\frac{\delta u_x}{U_0} + \frac{\delta\rho}{\rho_0} = \delta\mathcal{M}_a; \tag{A4}$$

$$\frac{\delta\rho}{\rho_0} + 2\frac{\delta u_x}{U_0} + \frac{\delta p}{\rho_0 U_0^2} = \delta\mathcal{M}_{mx}; \tag{A5}$$

$$\frac{\delta u_y}{U_0} = \delta\mathcal{M}_{my}; \tag{A6}$$

$$\frac{\delta u_x}{U_0} + \frac{(a_0^2/U_0^2)}{\gamma - 1}\left(\frac{\delta p}{P_0} - \frac{\delta\rho}{\rho_0}\right) + \frac{\mathcal{E}_0}{U_0^2}\left(\frac{\delta u_x}{U_0} + \frac{\delta\rho}{\rho_0}\right) = \frac{\delta\mathcal{E}_T}{U_0^2}, \tag{A7}$$

where $\mathcal{E}_0 \equiv (1/2)U_0^2 + a_0^2/(\gamma - 1)$.

To extract the amplitude, phase, and dispersion relation information embedded in the perturbed conservation laws (A4)–(A7), we need to decompose the gas fluctuations in terms of the Doppler-shifted normal-mode analysis. The hydrodynamic equations are expressed in the spacecraft frame such that $\boldsymbol{U} = \boldsymbol{U}_0 + \delta\boldsymbol{u}$ and $\delta\Psi = \delta\hat{\Psi}\exp[i(\omega t - \boldsymbol{k}\cdot\boldsymbol{x})]$. We measure a fluctuation $\delta\Psi$ at $\boldsymbol{x} = 0$, together with $\omega_m'$ and $\boldsymbol{k}_m$, i.e., $\omega_m'$ is the measured Doppler-shifted frequency, and $\omega' = \omega - \boldsymbol{U}_0\cdot\boldsymbol{k}$. We can express $\omega t - \boldsymbol{k}\cdot\boldsymbol{x} = \omega' t - \boldsymbol{k}\cdot\boldsymbol{x}'$, where $\boldsymbol{x}' \equiv \boldsymbol{x} - \boldsymbol{U}_0 t$ is the comoving spatial coordinate in the fluid frame.

The measured density fluctuation $\delta\rho_m$ is the sum of the entropy and the fast and slow acoustic density fluctuations, i.e., $\delta\rho_m = \delta\rho^e + \delta\rho^{a+} + \delta\rho^{a-}$ or

$$\delta\hat{\rho}_m e^{i(\omega_m' t - \boldsymbol{k}_m\cdot\boldsymbol{x}')} = \delta\hat{\rho}^e e^{i(\omega_e t - \boldsymbol{k}^e\cdot\boldsymbol{x})}$$
$$+ \delta\hat{\rho}^{a+} e^{i(\omega_{a+} t - \boldsymbol{k}^{a+}\cdot\boldsymbol{x})} + \delta\hat{\rho}^{a-} e^{i(\omega_{a-} t - \boldsymbol{k}^{a-}\cdot\boldsymbol{x})}. \tag{A8}$$

Expressed in the fluid frame and incorporating the dispersion relation, we have, e.g.,

$$\delta\hat{\rho}^e e^{i(\omega_e t-\boldsymbol{k}^e\cdot\boldsymbol{x})}=\delta\hat{\rho}^e e^{i(\omega_e' t-\boldsymbol{k}^e\cdot\boldsymbol{x}')}=\delta\hat{\rho}^e e^{-i\boldsymbol{k}^e\cdot\boldsymbol{x}'},$$
$$\text{and}\quad \delta\hat{\rho}^{a\pm}e^{i(\omega_{a\pm}t-\boldsymbol{k}^{a\pm}\cdot\boldsymbol{x})}=\delta\hat{\rho}^{a\pm}e^{i(\omega_{a\pm}' t-\boldsymbol{k}^{a\pm}\cdot\boldsymbol{x}')}, \tag{A9}$$

since $\omega_e'=0$.

The measurements are made at $\boldsymbol{x}=0$ in the spacecraft frame, which implies that $\boldsymbol{x}'=-\boldsymbol{U}_0 t$. We set $t=\Delta t$ to indicate that the observation is made over a suitably short time interval. Essentially, a parcel of gas within which the various linear modes are embedded is measured over an interval $\Delta t$ that ensures that the gas parcel remains coherent with respect to the decomposition. Accordingly, (A8) becomes

$$\delta\hat{\rho}_m e^{i\Delta t(\omega_m'+\boldsymbol{U}_0\cdot\boldsymbol{k}_m)}=\delta\hat{\rho}^e e^{i\Delta t\boldsymbol{U}_0\cdot\boldsymbol{k}^e)}$$
$$+\delta\hat{\rho}^{a+}e^{i\Delta t(\omega_m'+\boldsymbol{U}_0\cdot\boldsymbol{k}^{a+})}+\delta\hat{\rho}^{a-}e^{i\Delta t(-\omega_m'+\boldsymbol{U}_0\cdot\boldsymbol{k}^{a-})}, \tag{A10}$$

after using $\omega_{a+}'=+a_0k^{a+}=\omega_m'$ and $\omega_{a-}'=-a_0k^{a-}=-\omega_m'$ in (A9). On expressing the exponential in terms of its real part and using the Taylor expansion for $\omega_m'\Delta t\ll 1$,

$$\delta\hat{\Psi}\Delta t(\omega'+\boldsymbol{U}_0\cdot\boldsymbol{k})=\delta\hat{\Psi}\sum_{n=0}^{\infty}(-1)^n(\Delta t)^{2n}\frac{(\omega'+\boldsymbol{U}_0\cdot\boldsymbol{k})^{2n}}{(2n)}$$
$$=\delta\hat{\Psi}\left(1-\frac{1}{2}(\Delta t)^2(\omega'+\boldsymbol{U}_0\cdot\boldsymbol{k})\right)^2+\cdots),$$

we find from (A10) that the amplitudes satisfy

$$(n=0):\quad \delta\hat{\rho}_m=\delta\hat{\rho}^e+\delta\hat{\rho}^{a+}+\delta\hat{\rho}^{a-}, \tag{A11}$$

and the phase information is contained at the next order,

$$(n=1):\quad \delta\hat{\rho}_m(\omega_m'+\boldsymbol{U}_0\cdot\boldsymbol{k}_m)^2=\delta\hat{\rho}^e(\boldsymbol{U}_0\cdot\boldsymbol{k}^e)^2$$
$$+\delta\hat{\rho}^{a+}(\omega_m'+\boldsymbol{U}_0\cdot\boldsymbol{k}^{a+})^2+\delta\hat{\rho}^{a-}(-\omega_m'+\boldsymbol{U}_0\cdot\boldsymbol{k}^{a-})^2. \tag{A12}$$

Similarly, for $\delta\boldsymbol{u}_m=\delta\boldsymbol{u}^v+\delta\boldsymbol{u}^{a+}+\delta\boldsymbol{u}^{a-}$, we have

$$(n=0):\quad \delta\hat{\boldsymbol{u}}_m=\delta\hat{\boldsymbol{u}}^v+\delta\hat{\boldsymbol{u}}^{a+}+\delta\hat{\boldsymbol{u}}^{a-};$$
$$(n=1):\quad \delta\hat{\boldsymbol{u}}_m(\omega_m'+\boldsymbol{U}_0\cdot\boldsymbol{k}_m)^2$$
$$=\delta\hat{\boldsymbol{u}}^v(\boldsymbol{U}_0\cdot\boldsymbol{k}^v)^2+\delta\hat{\boldsymbol{u}}^{a+}(\omega_m'+\boldsymbol{U}_0\cdot\boldsymbol{k}^{a+})^2$$
$$+\delta\hat{\boldsymbol{u}}^{a-}(-\omega_m'+\boldsymbol{U}_0\cdot\boldsymbol{k}^{a-})^2, \tag{A13}$$

since $\omega_v'=0$, and for $\delta p_m=\delta p^{a+}=\delta p^{a-}$,

$$(n=0):\quad \delta\hat{p}_m=\delta\hat{p}^{a+}+\delta\hat{p}^{a-};$$
$$(n=1):\quad \delta\hat{p}_m(\omega_m'+\boldsymbol{U}_0\cdot\boldsymbol{k}_m)^2$$
$$=\delta\hat{p}^{a+}(\omega_m'+\boldsymbol{U}_0\cdot\boldsymbol{k}^{a+})^2+\delta\hat{p}^{a-}(-\omega_m'+\boldsymbol{U}_0\cdot\boldsymbol{k}^{a-})^2. \tag{A14}$$

The $n=0$ amplitude relations are used in the expansion of the conservation laws (A4)–(A7) and then reduced further by application of the eigenrelations (A1)–(A3). This then requires additional knowledge about the phases, which is contained in the $n=1$ expansion in terms of the measured frequency $\omega_m'$ and wavenumber $\boldsymbol{k}_m$. The phases derived from the $n=1$ results are therefore coupled to the $n=0$ amplitudes and the conservation law solutions.

There exist four unknown amplitudes, $\delta\hat{\rho}$, $\delta u^v\propto\delta\boldsymbol{u}^v=\delta u^v(-\beta,\alpha)$, and $\delta p^{a\pm}$ through $\delta\boldsymbol{u}^{a\pm}\propto\boldsymbol{k}^{a\pm}/k\delta p^{a\pm}$. Evidently, the eigenrelations embed phase information into the conservation laws. There are eight wavenumbers that are needed, $\boldsymbol{k}^e$, $\boldsymbol{k}^v$, and $\boldsymbol{k}^{a\pm}$, or equivalently $k^e$, $\theta^e$; $k^v$, $\theta^v$; and $k^{a\pm}$, $\theta^{a\pm}$. We have four conservation laws (A4)–(A7) for the four amplitudes ($n=0$) and four equations ($n=1$) to solve for the eight phase variables $k$, $\theta$. Fortunately, the number of phase variables is easily reduced to four.

1. Since the entropy mode is advected only, $k_y^e=k^e\sin\theta^e=0$ implies $\theta^e=0$ and $k_x^e=k^e$.
2. Since the fast (+) acoustic mode satisfies $\omega_{a+}'=a_0k^{a+}=\omega_m'$, the magnitude $k^{a+}=\omega_m'/a_0$ and hence $k_x^{a+}=(\omega_m'/a_0)\cos\theta^{a+}$.
3. Similarly, the slow (−) acoustic mode satisfies $\omega_{a-}'=-a_0k^{a+}=-\omega_m'$, giving $k^{a-}=+\omega_m'/a_0$ so that $k_x^{a-}=+(\omega_m'/a_0)\cos\theta^{a+}$.
4. Finally, for the vorticity, $k_x^v\neq 0$, $k_v^v\neq 0$. However, $\omega_v'=\omega-U_0k_x^v=0$, implying that $k_x^v=\omega/U_0=k^v\cos\theta^v$. Since $\omega_m'=\omega_{a+}'=\omega-U_0k_x^{a+}=\omega-U_0k^{a+}\cos\theta^{a+}=\omega-(\omega_m'/a_0)U_0\cos\theta^{a+}$, we have $\omega=\omega_m'(1+M_0\cos\theta^{a+})$, $M_0\equiv U_0/a_0$, and hence $k_x^v=(\omega_m'/U_0)(1+M_0\cos\theta^{a+})$.

We are therefore left with just four phase unknowns: $k^e$, $\theta^{a\pm}$, and $\theta^v$.

It is straightforward to show that the four $n=1$ Equations (A12)–(A14) can be expressed as

$$\frac{\delta\hat{\rho}_m}{\rho_0}\left(1+\frac{U_0k_{mx}}{\omega_m'}\right)^2=\frac{\delta\hat{\rho}^e}{\rho_0}\left(\frac{U_0k^e}{\omega_m'}\right)^2$$
$$+\frac{\delta\hat{p}^{a+}}{\rho_0a_0^2}(1+M_0\cos\theta^{a+})^2+\frac{\delta\hat{p}^{a-}}{\rho_0a_0^2}(1-M_0\cos\theta^{a-})^2; \tag{A15}$$

$$\frac{\delta\hat{u}_{mx}}{U_0}\left(1+\frac{U_0k_{mx}}{\omega_m'}\right)^2=-\frac{\delta\hat{u}^v}{U_0}\sin\theta^v\left(\frac{U_0k_x^v}{\omega_m'}\right)^2$$
$$+\frac{\delta\hat{p}^{a+}}{\rho_0a_0^2}\frac{\cos\theta^{a+}}{M_0}(1+M_0\cos\theta^{a+})^2$$
$$-\frac{\delta\hat{p}^{a-}}{\rho_0a_0^2}\frac{\cos\theta^{a-}}{M_0}(1-M_0\cos\theta^{a-})^2; \tag{A16}$$

$$\frac{\delta\hat{u}_{my}}{U_0}\left(1+\frac{U_0k_{mx}}{\omega_m'}\right)^2=-\frac{\delta\hat{u}^v}{U_0}\cos\theta^v\left(\frac{U_0k_x^v}{\omega_m'}\right)^2$$
$$+\frac{\delta\hat{p}^{a+}}{\rho_0a_0^2}\frac{\sin\theta^{a+}}{M_0}(1+M_0\cos\theta^{a+})^2$$
$$-\frac{\delta\hat{p}^{a-}}{\rho_0a_0^2}\frac{\sin\theta^{a-}}{M_0}(1-M_0\cos\theta^{a-})^2; \tag{A17}$$

$$\frac{\delta\hat{p}_m}{\rho_0a_0^2}\left(1+\frac{U_0k_{mx}}{\omega_m'}\right)^2=-\frac{\delta\hat{p}^{a+}}{\rho_0a_0^2}(1+M_0\cos\theta^{a+})^2$$
$$+\frac{\delta\hat{p}^{a-}}{\rho_0a_0^2}(1-M_0\cos\theta^{a-})^2. \tag{A18}$$

The four Equations (A15)–(A18) can be solved to provide the needed phase information as follows. It is simplest to begin with (A18). Because the amplitude equality (A14) ($n=0$) must hold, a consistent solution requires that both

$$(1+M_0\cos\theta^{a+})^2=(1-M_0\cos\theta^{a-})^2 \tag{A19}$$

$$\text{and} \quad \left(1 + \frac{U_0 k_{mx}}{\omega'_m}\right)^2 = (1 + M_0 \cos\theta^{a+})^2 \tag{A20}$$

hold. From (A19), we require that $\cos\theta^{a+} = -\cos\theta^{a-}$, or

$$\theta^{a-} = \pi - \theta^{a+}, \tag{A21}$$

since $\theta \in [0, \pi]$. Hence, for the equality (A20) to hold, we have

$$\cos\theta^{a+} = \frac{1}{M_0}\frac{U_0 k_{mx}}{\omega'_m}. \tag{A22}$$

From Equation (A15), to ensure that $(n = 0)$ $\delta\hat{\rho}_m = \delta\hat{\rho}^e + \delta\hat{\rho}^{a+} + \delta\hat{\rho}^{a-}$, we must have

$$\left(\frac{U_0 k^e}{\omega'_m}\right)^2 = (1 + M_0 \cos\theta^{a+})^2 ,$$

from which we obtain

$$k^e = \frac{\omega'_m}{U_0}(1 + M_0 \cos\theta^{a+}). \tag{A23}$$

Similarly, using one of either (A16) or (A17), we need to ensure that one of $\delta\hat{u}_{mx/y} = \delta\hat{u}^v_{x/y} + \delta\hat{u}^{a+}_{x/y} + \delta\hat{u}^{a-}_{x/y}$ holds, which requires that

$$\left(\frac{U_0 k^v}{\omega'_m}\right)^2 = (1 + M_0 \cos\theta^{a+})^2 .$$

Thus, we have

$$k^v_x = k^v \cos\theta^v = \frac{\omega'_m}{U_0}(1 + M_0 \cos\theta^{a+}). \tag{A24}$$

The remaining unused Equation (A16) or (A17) allows us to solve for $\theta^v$. In this case, using (A16) yields an equation that has to be solved iteratively for $\theta^v$ in concert with the conservation Equations (A4)–(A7):

$$\frac{\delta\hat{u}^v}{U_0}\sin\theta^v = \left(\frac{\delta p^{a+}}{\rho_0 a_0^2} + \frac{\delta p^{a-}}{\rho_0 a_0^2}\right)\frac{\cos\theta^{a+}}{M_0} - \frac{\delta\hat{u}_{mx}}{U_0}. \tag{A25}$$

Consequently, all the phase information can be derived from $\theta^{a+}$, which in turn is given by (A22). Hence, $\theta^{a-}$ is given by (A21), $k^e$ by (A23), $\theta^v$ by (A25), and $k^v$ by (A24).

By means of the amplitude relations $(n = 0)$ (A11)–(A14) and the eigenrelations (A1)–(A3), we can rewrite the conservation laws (A4)–(A7) in terms of the four normalized unknown variables $\delta\hat{\rho}^e/\rho_0$ (the fluctuating density associated with entropy modes), $\delta\hat{u}\ U_0$ (the magnitude of vortical fluctuations), and $\delta\hat{p}^{a\pm}/(\rho_0 a_0^2)$ (the pressure fluctuations of fast (+) and slow (−) acoustic modes). For example, in (A4),

$$\begin{aligned}
\delta\mathcal{M}_a &= \frac{\delta\hat{\rho}_m}{\rho_0} + \frac{\delta\hat{u}_{mx}}{U_0};\\
\frac{\delta\hat{\rho}}{\rho_0} &= \frac{1}{\rho_0}(\hat{\rho}^e + \hat{\rho}^{a+} + \hat{\rho}^{a-}) = \frac{\delta\hat{\rho}^e}{\rho_0} + \frac{\delta\hat{p}^{a+}}{\rho_0 a_0^2} + \frac{\delta\hat{p}^{a-}}{\rho_0 a_0^2};\\
\frac{\delta\hat{u}_x}{U_0} &= \frac{1}{U_0}(\hat{u}^v_x + \hat{u}^{a+}_x + \hat{u}^{a-}_x) = -\beta^v\frac{\delta\hat{u}^v}{U_0}\\
&\quad + \frac{k^{a+}_x/k^{a+}}{M_0}\frac{\delta\hat{p}^{a+}}{\rho_0 a_0^2} + \frac{k^{a-}_x/k^{a-}}{M_0}\frac{\delta\hat{p}^{a-}}{\rho_0 a_0^2}.
\end{aligned}$$

This allows (A4)–(A7) to be expressed as

$$\begin{aligned}
&\left(1 + \frac{a}{M_0}\cos\theta^{a+}\right)\frac{\delta\hat{p}^{a+}}{\rho_0 a_0^2} + \left(1 - \frac{a}{M_0}\cos\theta^{a-}\right)\\
&\times \frac{\delta\hat{p}^{a-}}{\rho_0 a_0^2} + \frac{\delta\hat{\rho}^e}{\rho_0} - \sin\theta^v\frac{\delta\hat{u}^v}{U_0} = \frac{\delta\hat{\rho}_m}{\rho_0} + \frac{\delta\hat{u}_{mx}}{U_0};
\end{aligned} \tag{A26}$$

$$\left(1 + 2\frac{\cos\theta^{a+}}{M_0} + \frac{1}{M_0^2}\right)\frac{\delta\hat{p}^{a+}}{\rho_0 a_0^2} + \left(1 - 2\frac{\cos\theta^{a-}}{M_0} + \frac{1}{M_0^2}\right)\frac{\delta\hat{p}^{a-}}{\rho_0 a_0^2} + \frac{\delta\hat{\rho}^e}{\rho_0} - 2\sin\theta^v\frac{\delta\hat{u}^v}{U_0} = \frac{\delta\hat{\rho}_m}{\rho_0} + 2\frac{\delta\hat{u}_{mx}}{U_0} + \frac{1}{M_0^2}\frac{\delta\hat{p}_m}{\rho_0 a_0^2}; \tag{A27}$$

$$\frac{\sin\theta^{a+}}{M_0}\frac{\delta\hat{p}^{a+}}{\rho_0 a_0^2} - \frac{\sin\theta^{a-}}{M_0}\frac{\delta\hat{p}^{a-}}{\rho_0 a_0^2} + \cos\theta^v\frac{\delta\hat{u}^v}{U_0} = \frac{\delta\hat{u}_{my}}{U_0}; \tag{A28}$$

$$\begin{aligned}
&\left[\frac{1}{2} + \frac{\gamma}{\gamma - 1}\frac{1}{M_0^2} + \left(\frac{3}{2} + \frac{1}{\gamma - 1}\frac{1}{M_0^2}\right)\frac{\cos\theta^{a+}}{M_0}\right]\frac{\delta\hat{p}^{a+}}{\rho_0 a_0^2}\\
&+ \left[\frac{1}{2} + \frac{\gamma}{\gamma - 1}\frac{1}{M_0^2} - \left(\frac{3}{2} + \frac{1}{\gamma - 1}\frac{1}{M_0^2}\right)\frac{\cos\theta^{a-}}{M_0}\right]\frac{\delta\hat{p}^{a-}}{\rho_0 a_0^2}\\
&+ \frac{1}{2}\frac{\delta\hat{\rho}^e}{\rho_0} - \left(\frac{3}{2} + \frac{1}{\gamma - 1}\frac{1}{M_0^2}\right)\sin\theta^v\frac{\delta\hat{u}^v}{U_0}\\
&= \left(\frac{3}{2} + \frac{1}{\gamma - 1}\frac{1}{M_0^2}\right)\frac{\delta\hat{u}_{mx}}{U_0} + \frac{\gamma}{\gamma - 1}\frac{1}{M_0^2}\frac{\delta\hat{p}_m}{\rho_0 a_0^2} + \frac{1}{2}\frac{\delta\hat{\rho}_m}{\rho_0}.
\end{aligned} \tag{A29}$$

Equations (A26)–(A29) together with (A21)–(A25) completely specify the mode-decomposition problem for 2D hydrodynamics. Thus, solving the linear system of equations for a measured set of fluctuations $(\delta\rho_m, \delta\boldsymbol{u}_m, \delta p_m)$ at a frequency $\omega'_m$ and wavenumber $\boldsymbol{k}_m$ expresses the measured fluctuations as superposition of entropy, vorticity, and fast and slow acoustic modes. The approach outlined here serves as a template for the more complicated problem of mode decomposition in MHD.

## Appendix B
## Summary of the Amplitude Matrix Entries

The amplitude matrix appropriate to a mean flow aligned obliquely to the mean magnetic field is given by $\boldsymbol{A} = (a_{ij})$, $i, j = 1 \cdots 8$, an $(8 \times 8)$ matrix that contains the amplitudes and phases of the entropy, fast, and slow magnetosonic, Alfvénic, and magnetic island modes. Here,

$$\boldsymbol{A}\boldsymbol{x} = \boldsymbol{b}, \quad \text{where} \quad \boldsymbol{A} = (a_{ij}),\ \boldsymbol{x} = (x_j),\ \boldsymbol{b} = (b_i), \quad i, j = 1 \cdots 8;$$
$$\boldsymbol{x} = \left( \frac{\delta\rho^e}{\rho_0}, \frac{\delta\hat{p}^{f+}}{\rho_0 a_0^2}, \frac{\delta\hat{p}^{f-}}{\rho_0 a_0^2}, \frac{\delta\hat{p}^{s+}}{\rho_0 a_0^2}, \frac{\delta\hat{p}^{s-}}{\rho_0 a_0^2}, \frac{\delta u^{A+}}{U_0}, \frac{\delta u^{A-}}{U_0}, \frac{\delta B^i}{B_0} \right)^t. \tag{B1}$$

The vector $\boldsymbol{b}$ is comprised of measured values and given below. Here, we list the elements $(a_{ij})$ of the matrix $\boldsymbol{A}$ derived from the MHD conservation laws.

Continuity:

$$\begin{aligned}
a_{11} &= 1;\\
a_{12} &= \left(1 + \frac{1}{M_0}\frac{V_{f+}}{a_0}\frac{V_{f+}^2 \cos\phi^{f+}\sin\theta^{f+}}{V_f^2 - V_{A0}^2\cos^2\theta^{f+}}\sin\psi + \frac{1}{M_0}\frac{a_0}{V_{f+}}\cos\theta^{f+}\cos\psi\right);\\
a_{13} &= a_{12}(f-); \quad \text{i.e., } f- \text{ replaces } f \text{ in } a_{12}.\\
a_{14} &= a_{12}(s+); \quad \text{i.e., } s+ \text{ replaces } f+ \text{ in } a_{12}.\\
a_{15} &= a_{12}(s-);\\
a_{16} &= -\beta^{A+}\sin\psi;\\
a_{17} &= -\beta^{A-}\sin\psi;\\
a_{18} &= 0.
\end{aligned}$$

Momentum: $x$-component

$$\begin{aligned}
a_{21} &= \sin\psi;\\
a_{22} &= \sin\psi\left(1 + \frac{1}{M_0^2}\right) + \frac{1+\sin^2\psi}{M_0}\frac{V_{f+}}{a_0}\frac{V_f^2\cos\phi^{f+}\sin\theta^{f+}}{V_f^2 - V_{A0}^2\cos^2\theta^{f+}} + \frac{\sin\psi\cos\psi}{M_0}\frac{a_0}{V_{f+}}\cos\theta^{f+}\\
&\quad + \frac{\sin\psi}{M_{A0}^2}\frac{V_f^2 - a_0^2\cos^2\theta^{f+}}{v_f^2} + \frac{\cos\psi}{M_{A0}^2}\frac{V_f^2\cos\phi^{f+}\sin\theta^{f+}\cos\theta^{f+}}{V_f^2 - V_{A0}^2\cos^2\theta^{f+}};\\
a_{23} &= a_{22}(f^-);\\
a_{24} &= a_{22}(s^+);\\
a_{25} &= a_{22}(s^-);\\
a_{26} &= -\left(\frac{\cos\psi}{M_{A0}} + (1 + \sin^2\psi)\right)\beta^{A+};\\
a_{27} &= \left(\frac{\cos\psi}{M_{A0}} - (1 + \sin^2\psi)\right)\beta^{A-};\\
a_{28} &= \frac{\cos\psi}{M_{A0}^2}\beta^i.
\end{aligned}$$

Momentum: $y$-component

$$\begin{aligned}
a_{31} &= 0;\\
a_{32} &= \frac{V_f^2\sin\phi^{f+}\sin\theta^{f+}}{V_f^2 - V_{A0}^2\cos^2\theta^{f+}}\left(\frac{\cos\psi}{M_{A0}^2}\cos\theta^{f+} + \frac{1}{M_{f+}(\theta^{f+})}\right);\\
a_{33} &= a_{32}(f-);\\
a_{34} &= a_{32}(s+);\\
a_{35} &= a_{32}(s-);\\
a_{36} &= \left(1 + \frac{\cos\psi}{M_{A0}}\right)\alpha^{A+};\\
a_{37} &= \left(1 - \frac{\cos\psi}{M_{A0}}\right)\alpha^{A-};\\
a_{38} &= -\frac{\cos\psi}{M_{A0}^2}.
\end{aligned}$$

Momentum: $z$-component

$$
\begin{aligned}
a_{41} &= \cos\psi;\\
a_{42} &= \cos\psi\left(1+\tfrac{1}{M_0^2}\right)+\tfrac{\cos\psi\sin\psi}{M_0}\tfrac{V_{f+}}{a_0}\tfrac{V_f^2\cos\phi^{f+}\sin\theta^{f+}}{V_f^2-V_{\rm A0}^2\cos^2\theta^{f+}}+(1+\cos^2\psi)\tfrac{a_0/V_{f+}}{M_0}\cos\theta^{f+}\\
&\quad+\tfrac{\sin\psi}{M_{\rm A0}^2}\tfrac{V_f^2\cos\phi^{f+}\sin\theta^{f+}\cos\theta^{f+}}{V_f^2-V_{\rm A0}^2\cos^2\theta^{f+}}-\tfrac{\cos\psi}{M_{\rm A0}^2}\tfrac{V_f^2-a_0^2\cos^2\theta^{f+}}{V_f^2};\\
a_{43} &= a_{42}(f-);\\
a_{44} &= a_{42}(s+);\\
a_{45} &= a_{42}(s-);\\
a_{46} &= -\sin\psi\left(\cos\psi+\tfrac{1}{M_{\rm A0}}\right)\beta^{A+};\\
a_{47} &= -\sin\psi\left(\cos\psi-\tfrac{1}{M_{\rm A0}}\right)\beta^{A-};\\
a_{48} &= \tfrac{\sin\psi}{M_{\rm A0}^2}\beta^{i}.
\end{aligned}
$$

Total energy:

$$
\begin{aligned}
a_{51} &= \frac{1}{2};\\
a_{52} &= \frac{1}{2}+\frac{\gamma}{\gamma-1}\frac{1}{M_0^2}+\left(\frac{\mathcal{E}_T}{U_0^2}+1\right)\frac{\sin\psi}{M_0}\frac{V_{f+}}{a_0}\frac{V_f^2\cos\phi^{f+}\sin\theta^{f+}}{V_f^2-V_{\rm A0}^2\cos^2\theta^{f+}}\\
&\quad+\left(\frac{\mathcal{E}_0}{U_0^2}+1\right)\frac{\cos\psi}{M_0}\frac{a_0}{V_{f+}}\cos\theta^{f+}\\
&\quad+2\frac{\sin\psi\cos\psi}{M_{\rm A0}^2}\frac{V_f^2\cos\phi^{f+}\sin\theta^{f+}\cos\theta^{f+}}{V_f^2-V_{\rm A0}^2\cos^2\theta^{f+}}\\
&\quad+2\frac{\sin^2\psi}{M_{\rm A0}^2}\frac{V_f^2-a_0^2\cos^2\theta^{f+}}{V_f^2};\\
a_{53} &= a_{52}(f-);\\
a_{54} &= a_{52}(s+);\\
a_{55} &= a_{52}(s-);\\
a_{56} &= -\left(\left(\frac{\mathcal{E}_T}{U_0^2}+1\right)+2\frac{\cos\psi}{M_{\rm A0}}\right)\sin\psi\beta^{A+};\\
a_{57} &= -\left(\left(\frac{\mathcal{E}_T}{U_0^2}+1\right)-2\frac{\cos\psi}{M_{\rm A0}}\right)\sin\psi\beta^{A-};\\
a_{58} &= 2\frac{\sin\psi\cos\psi}{M_{\rm A0}^2}\beta^{i},
\end{aligned}
$$

where $\mathcal{E}_0 \equiv (1/2)U_0^2 + a_0^2/(\gamma-1)$ and $\mathcal{E}_T \equiv \mathcal{E}_0 + V_{\rm A0}^2$.

Induction: $x$-component

$$
\begin{aligned}
a_{61} &= 0;\\
a_{62} &= \cos\psi\left(\frac{V_f^2\cos\phi^{f+}\sin\theta^{f+}}{V_f^2-V_{\rm A0}^2\cos^2\theta^{f+}}\left(\frac{V_{f+}/a_0}{M_0}+\cos\psi\cos\theta^{f+}\right)+\sin\psi\frac{V_f^2-a_0^2\cos^2\theta^{f+}}{V_f^2}\right);\\
a_{63} &= a_{62}(f-);\\
a_{64} &= a_{62}(s+);\\
a_{65} &= a_{62}(s-);\\
a_{66} &= -\cos\psi(1+\cos\psi M_{\rm A0})\beta^{A+};\\
a_{67} &= -\cos\psi(1-\cos\psi M_{\rm A0})\beta^{A-};\\
a_{68} &= \cos^2\psi\beta^{i}.
\end{aligned}
$$

Induction: $y$-component

$$
\begin{aligned}
a_{71} &= 0;\\
a_{72} &= \frac{V_f^2 \sin\phi^{f+}\sin\theta^{f+}}{V_f^2 - V_{\rm A0}^2\cos^2\theta^{f+}}\left(\frac{\cos\psi}{M_0}\frac{V_{f+}}{a_0} + \cos\theta^{f+}\right);\\
a_{73} &= a_{72}(f-);\\
a_{74} &= a_{72}(s+);\\
a_{75} &= a_{72}(s-);\\
a_{76} &= (\cos\psi + M_{\rm A0})\alpha^{A+};\\
a_{77} &= (\cos\psi - M_{\rm A0})\alpha^{A-};\\
a_{78} &= -\alpha^i.
\end{aligned}
$$

Because the $z$-component for the induction equation is a linear combination of the $x$- and $y$-components of the induction equation, it is neglected.

Magnetic island condition:

$$
\begin{aligned}
a_{81} &= 0;\\
a_{82} &= -\frac{V_f^2\cos\phi^{f+}\sin\theta^{f+}\cos\theta^{f+}}{V_f^2 - V_{\rm A0}^2\cos^2\theta^{f+}};\\
a_{83} &= a_{82}(f-);\\
a_{84} &= a_{82}(s+);\\
a_{85} &= a_{82}(s-);\\
a_{86} &= M_{\rm A0}\beta^{A+};\\
a_{87} &= -M_{\rm A0}\beta^{A-};\\
a_{88} &= -\beta^i.
\end{aligned}
$$

*Source vector* $\boldsymbol{b}(\delta\hat{\Psi}_m)$. Here, we list the elements of the source vector $(b_i)$, $i = 1\cdots 8$, that comprise the measured plasma and magnetic field variables:

$$
\begin{aligned}
b_1 &= \frac{\delta\hat{\rho}_m}{\rho_0} + \sin\psi\frac{\delta\hat{u}_{mx}}{U_0} + \cos\psi\frac{\delta\hat{u}_{mz}}{U_0}; \quad \text{(continuity)}\\
b_2 &= \sin\psi\frac{\delta\hat{\rho}_m}{\rho_0} + (1+\sin^2\psi)\frac{\delta\hat{u}_{mx}}{U_0} + \sin\psi\cos\psi\frac{\delta\hat{u}_{mz}}{U_0} + \frac{\sin\psi}{M_0^2}\frac{\delta\hat{p}_m}{\rho_0 a_0^2} + \frac{1}{M_{\rm A0}^2}\left(-\cos\psi\frac{\delta\hat{B}_{mx}}{B_0} + \sin\psi\frac{\delta\hat{B}_{mz}}{B_0}\right);\\
&\quad (x\text{-momentum})\\
b_3 &= \frac{\delta\hat{u}_{my}}{U_0} - \frac{\cos\psi}{M_{\rm A0}^2}\frac{\delta\hat{B}_{my}}{B_0}; \quad (y\text{-momentum})\\
b_4 &= \cos\psi\frac{\delta\hat{\rho}_m}{\rho_0} + \cos\psi\sin\psi\frac{\delta\hat{u}_{mx}}{U_0} + (1+\cos^2\psi)\frac{\delta\hat{u}_{mz}}{U_0} + \frac{\cos\psi}{M_0^2}\frac{\delta\hat{p}_m}{\rho_0 a_0^2} - \frac{1}{M_{\rm A0}^2}\left(\sin\psi\frac{\delta\hat{B}_{mx}}{B_0} + \cos\psi\frac{\delta\hat{B}_{mz}}{B_0}\right);\\
&\quad (z\text{-momentum})\\
b_5 &= \frac{1}{2}\frac{\delta\hat{\rho}_m}{\rho_0} + \left(\frac{\mathcal{E}_T}{U_0^2}+1\right)\sin\psi\frac{\delta\hat{u}_{mx}}{U_0} + \left(\frac{\mathcal{E}_0}{U_0^2}+1\right)\cos\psi\frac{\delta\hat{u}_{mz}}{U_0} + \frac{\gamma}{\gamma-1}\frac{1}{M_0^2}\frac{\delta\hat{p}_m}{\rho_0 a_0^2}\\
&\quad - 2\frac{\sin\psi\cos\psi}{M_{\rm A0}^2}\frac{\delta\hat{B}_{mx}}{B_0} + 2\frac{\sin^2\psi}{M_{\rm A0}^2}\frac{\delta\hat{B}_{mz}}{B_0};\\
&\quad \text{(total energy)}\\
b_6 &= \cos\psi\frac{\delta\hat{u}_{mx}}{U_0} - \cos^2\psi\frac{\delta\hat{B}_{mx}}{B_0} + \sin\psi\cos\psi\frac{\delta\hat{B}_{mz}}{B_0}; \quad (x\text{-induction})\\
b_7 &= \cos\psi\frac{\delta\hat{u}_{my}}{U_0} - \frac{\delta\hat{B}_{my}}{B_0}; \quad (y\text{-induction})\\
b_8 &= \frac{\delta\hat{B}_{mx}}{B_0}. \quad \text{(magnetic island).}
\end{aligned}
$$

## Appendix C
## Algorithm Summary

Although the wavenumber boundary conditions are given in Section 3.4, it is convenient to list all the relations together and in order. We solve the angles needed needed for the $8 \times 8$ system of equations $\boldsymbol{Ax} = \boldsymbol{b}$ from

1. $\cos^2\theta^{f+} = \dfrac{1}{M_0^2 M_{\rm A0}^2}\dfrac{(M_0^2 + M_{\rm A0}^2)(\omega_m'/(U_0 k_{mz}))^2 - 1}{(\omega_m'/(U_0 k_{mz}))^4}$;
2. $\cos\phi^{f+} = \dfrac{1}{(\omega_m'/(U_0 k_{mx}))M_f(\theta^{f+})\sin\theta^{f+}}$
3. $\theta^{f-} = \theta^{f+}$;
4. $\phi^{f-} = \phi^{f+}$;
5. $\cos^2\theta^{s+} = \dfrac{M_f^2(\theta^{f+})}{M_0^2 M_{\rm A0}^2}\cos^2\theta^{f+}(M_0^2 + M_{\rm A0}^2 - M_f^2(\theta^{f+})\cos^2\theta^{f+})$;
6. $\cos\phi^{s+} = \dfrac{M_f(\theta^{f+})}{M_s(\theta^{s+})}\dfrac{\cos\phi^{f+}\sin\theta^{f+}}{\sin\theta^{s+}}$;
7. $\theta^{s-} = \theta^{s+}$;
8. $\phi^{s-} = \phi^{s+}$;
9. $\phi^e = 0$;
10. $\tan\theta^e = \dfrac{\sin\psi + M_f(\theta^{f+})\cos\phi^{f+}\sin\theta^{f+}}{\cos\psi + M_f(\theta^{f+})\cos\theta^{f+}}$.

The angles $\phi^{A\pm}$, $\theta^{A\pm}$, and $\phi^i$ associated with the Alfvénic and magnetic island modes are solved iteratively from

1. $\dfrac{\delta\hat{u}^{A+}}{U_0}\sin\phi^{A+} + \dfrac{\delta\hat{u}^{A-}}{U_0}\sin\phi^{A-} = -\dfrac{\delta\hat{u}_{mx}}{U_0} + \dfrac{1}{M_f(\theta^{f+})}$
$\times\left[\dfrac{\delta\hat{p}^{f+}}{\rho_0 a_0^2} + \dfrac{\delta\hat{p}^{f-}}{\rho_0 a_0^2} + \dfrac{M_f^2(\theta^{f+})}{M_s^2(\theta^{s+})}\left(\dfrac{\delta\hat{p}^{s+}}{\rho_0 a_0^2} + \dfrac{\delta\hat{p}^{s-}}{\rho_0 a_0^2}\right)\right]\dfrac{M_{\rm A0}^2\cos\phi^{f+}\sin\theta^{f+}}{M_{\rm A0}^2 - M_f^2(\theta^{f+})\cos^2\theta^{f+}}$;
2. $\dfrac{\delta\hat{u}^{A+}}{U_0}\cos\phi^{A+} + \dfrac{\delta\hat{u}^{A-}}{U_0}\cos\phi^{A-} = \dfrac{\delta\hat{u}_{my}}{U_0}$
$-\left(\dfrac{\delta\hat{p}^{f+}}{\rho_0 a_0^2} + \dfrac{\delta\hat{p}^{f-}}{\rho_0 a_0^2}\right)\dfrac{1}{M_f(\theta^{f+})}\dfrac{M_{\rm A0}^2\sin\phi^{f+}\sin\theta^{f+}}{M_{\rm A0}^2 - M_f^2(\theta^{f+})\cos^2\theta^{f+}}$
$-\left(\dfrac{\delta\hat{p}^{s+}}{\rho_0 a_0^2} + \dfrac{\delta\hat{p}^{s-}}{\rho_0 a_0^2}\right)\dfrac{1}{M_s(\theta^{s+})}\dfrac{M_{\rm A0}^2\sin\phi^{s+}\sin\theta^{s+}}{M_{\rm A0}^2 - M_s^2(\theta^{s+})\cos^2\theta^{s+}}$;
3. $\tan\theta^{A\pm} = (\cos\phi^{A\pm})^{-1}\dfrac{M_{\rm A0}\cos\psi \pm 1}{M_{\rm A0}\cos\psi}\dfrac{\sin\psi + M_f(\theta^{f+})\cos\phi^{f+}\sin\theta^{f+}}{\cos\psi + M_f(\theta^{f+})\cos\theta^{f+}}$;
4. $\dfrac{\delta\hat{B}^i}{B_0}\cos\phi^i = \dfrac{\delta\hat{B}_{my}}{B_0} + \left(\dfrac{\delta\hat{p}^{f+}}{\rho_0 a_0^2} + \dfrac{\delta\hat{p}^{f-}}{\rho_0 a_0^2}\right)\dfrac{M_{\rm A0}^2\sin\phi^{f+}\sin\theta^{f+}\cos\theta^{f+}}{M_{\rm A0}^2 - M_f^2(\theta^{f+})\cos^2\theta^{f+}}$
$+\left(\dfrac{\delta\hat{p}^{s+}}{\rho_0 a_0^2} + \dfrac{\delta\hat{p}^{s-}}{\rho_0 a_0^2}\right)\dfrac{M_{\rm A0}^2\sin\phi^{s+}\sin\theta^{s+}\cos\theta^{s+}}{M_{\rm A0}^2 - M_s^2(\theta^{s+})\cos^2\theta^{s+}} + M_{\rm A0}\left(\dfrac{\delta\hat{u}^{A+}}{U_0}\cos\phi^{A+} + \dfrac{\delta\hat{u}^{A-}}{U_0}\cos\phi^{A-}\right)$.

## ORCID iDs

G. P. Zank https://orcid.org/0000-0002-4642-6192
L.-L. Zhao https://orcid.org/0000-0002-4299-0490
L. Adhikari https://orcid.org/0000-0003-1549-5256
M. Nakanotani https://orcid.org/0000-0002-7203-0730
D. Telloni https://orcid.org/0000-0002-6710-8142
H. Che https://orcid.org/0000-0002-2240-6728

## References

Adhikari, L., Khabarova, O., Zank, G. P., & Zhao, L. L. 2019, ApJ, 873, 72
Adhikari, L., Zank, G., & Zhao, L.-L. 2020a, ApJ, 901, 102
Adhikari, L., Zank, G. P., Hunana, P., et al. 2017, ApJ, 841, 85
Adhikari, L., Zank, G. P., Zhao, L. L., et al. 2020b, ApJS, 246, 38
Adhikari, L., Zank, G. P., Zhao, L. L., et al. 2021, A&A, 656, A6
Adhikari, L., Zank, G. P., Zhao, L. L., & Telloni, D. 2022a, ApJ, 938, 120
Adhikari, L., Zank, G. P., Zhao, L. L., & Telloni, D. 2022b, ApJ, 933, 56
Asgari-Targhi, M., Asgari-Targhi, A., Hahn, M., & Savin, D. W. 2021, ApJ, 911, 63
Bandyopadhyay, R., & McComas, D. J. 2021, ApJ, 923, 193
Bieber, J. W., Wanner, W., & Matthaeus, W. H. 1996, JGR, 101, 2511
Bruno, R., Telloni, D., Primavera, L., et al. 2014, ApJ, 786, 53
Burlaga, L. F. 1969, SoPh, 7, 54
Burlaga, L. F., & Ness, N. F. 1969, SoPh, 9, 467
Chen, Y., Hu, Q., & le Roux, J. A. 2019, ApJ, 881, 58
Cho, J., & Lazarian, A. 2003, MNRAS, 345, 325
Feng, H., Wu, D., Lin, C., et al. 2008, JGRA, 113, A12105
Forman, M. A., Wicks, R. T., & Horbury, T. S. 2011, ApJ, 733, 76
Fu, X., Li, H., Gan, Z., Du, S., & Steinberg, J. 2022, ApJ, 936, 127
Gan, Z., Li, H., Fu, X., & Du, S. 2022, ApJ, 926, 222
Glassmeier, K. H., Motschmann, U., & von Stein, R. 1995, AnGeo, 13, 76

Goldreich, P., & Sridhar, S. 1995, ApJ, 438, 763
Greco, A., Chuychai, P., Matthaeus, W. H., Servidio, S., & Dmitruk, P. 2008, GeoRL, 35, 19111
Horbury, T. S., O'Brien, H., Carrasco Blazquez, I., et al. 2020, A&A, 642, A9
Hunana, P., & Zank, G. P. 2010, ApJ, 718, 148
Khabarova, O., Zank, G. P., Li, G., et al. 2015, ApJ, 808, 181
Khabarova, O. V., & Zank, G. P. 2017, ApJ, 843, 4
Khabarova, O. V., Zank, G. P., Li, G., et al. 2016, ApJ, 827, 122
Knetter, T., Neubauer, F. M., Horbury, T., & Balogh, A. 2004, JGRA, 109, A06102
Lighthill, M. J. 1960, RSPTA, 252, 397
Malandraki, O., Khabarova, O., Bruno, R., et al. 2019, ApJ, 881, 116
Matthaeus, W. H., & Brown, M. R. 1988, PhFl, 31, 3634
McKenzie, J. F., & Westphal, K. O. 1968, PhFl, 11, 2350
Moldwin, M. B., Ford, S., Lepping, R., Slavin, J., & Szabo, A. 2000, GeoRL, 27, 57
Montgomery, D., Brown, M. R., & Matthaeus, W. H. 1987, JGR, 92, 282
Motschmann, U., Glassmeier, K.-H., & Pinçon, J.-L. 1998, ISSIR, 1, 79
Owen, C. J., Bruno, R., Livi, S., et al. 2020, A&A, 642, A16
Šafránková, J., Němeček, Z., Němec, F., et al. 2015, ApJ, 803, 107
Santolik, O., Parrot, M., & Lefeuvre, F. 2003, RaSc, 38, 1010
Saur, J., & Bieber, J. W. 1999, JGR, 104, 9975
Sonnerup, B. U. Ö., & Scheible, M. 1998, ISSIR, 1, 185
Tasnim, S., Zank, G. P., Cairns, I. H., & Adhikari, L. 2022, ApJ, 928, 125
Telloni, D., Bruno, R., Carbone, V., Antonucci, E., & D'Amicis, R. 2009, ApJ, 706, 238
Telloni, D., Carbone, F., Bruno, R., et al. 2019, ApJ, 887, 160
Telloni, D., Perri, S., Bruno, R., Carbone, V., & Amicis, R. D. 2013, ApJ, 776, 3
Telloni, D., Zhao, L., Zank, G. P., et al. 2020, ApJL, 905, L12
Trenchi, L., Bruno, R., D'Amicis, R., Marcucci, M. F., & Telloni, D. 2013, AnGeo, 31, 1333
Veltri, P. 1999, PPCF, 41, 787
Zank, G. P. 2014, Transport Processes in Space Physics and Astrophysics (New York: Springer)
Zank, G. P., Adhikari, L., Hunana, P., et al. 2017, ApJ, 835, 147
Zank, G. P., Hunana, P., Mostafavi, P., et al. 2015, ApJ, 814, 137
Zank, G. P., le Roux, J. A., Webb, G. M., Dosch, A., & Khabarova, O. 2014, ApJ, 797, 28
Zank, G. P., & Matthaeus, W. H. 1990, PhRvL, 64, 1243
Zank, G. P., & Matthaeus, W. H. 1992, JGR, 97, 17189
Zank, G. P., & Matthaeus, W. H. 1993, PhFl, 5, 257
Zank, G. P., Matthaeus, W. H., & Klein, L. W. 1990, GeoRL, 17, 1239
Zank, G. P., Nakanotani, M., Zhao, L. L., et al. 2021a, ApJ, 913, 127
Zank, G. P., Nakanotani, M., Zhao, L. L., Adhikari, L., & Telloni, D. 2020, ApJ, 900, 115
Zank, G. P., Zhao, L. L., Adhikari, L., et al. 2021b, PhPl, 28, 080501
Zank, G. P., Zhao, L. L., Adhikari, L., et al. 2022, ApJL, 926, L16
Zhao, L. L., Zank, G. P., Adhikari, L., et al. 2020, ApJS, 246, 26
Zhao, L. L., Zank, G. P., Adhikari, L., & Nakanotani, M. 2022b, ApJL, 924, L5
Zhao, L. L., Zank, G. P., Adhikari, L., et al. 2022c, ApJL, 934, L36
Zhao, L. L., Zank, G. P., Chen, Y., et al. 2019, ApJ, 872, 4
Zhao, L. L., Zank, G. P., He, J. S., et al. 2021b, ApJ, 922, 188
Zhao, L. L., Zank, G. P., He, J. S., et al. 2021c, A&A, 656, A3
Zhao, L. L., Zank, G. P., Hu, Q., et al. 2021a, A&A, 650, A12
Zhao, L. L., Zank, G. P., Nakanotani, M., & Adhikari, L. 2023, ApJ, 944, 98
Zhao, L. L., Zank, G. P., Telloni, D., et al. 2022d, ApJL, 928, L15
Zhao, S. Q., Yan, H., Liu, T. Z., Liu, M., & Wang, H. 2022a, ApJ, 937, 102
Zheng, J., & Hu, Q. 2018, ApJL, 852, L23